

Adriana Maria Pires Mamede

BURNED BONES: A COMPARISON OF METHODOLOGICAL APPROACHES TO ASSESS HEAT-INDUCED ALTERATIONS

Master in Forensic Chemistry

Chemistry Department

FCTUC

September 2017



UNIVERSIDADE DE COIMBRA

Adriana Maria Pires Mamede

BURNED BONES: A COMPARISON OF
METHODOLOGICAL APPROACHES TO ASSESS
HEAT-INDUCED ALTERATIONS

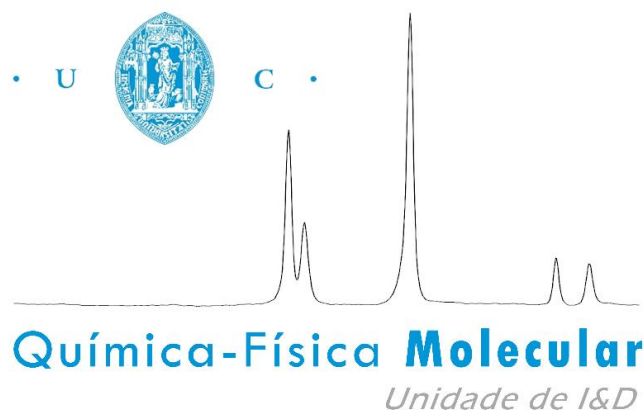
Dissertation presented as evaluation for the Master in Forensic Chemistry

Supervisor: Prof. Dr. Luís Alberto Esteves Baptista de Carvalho

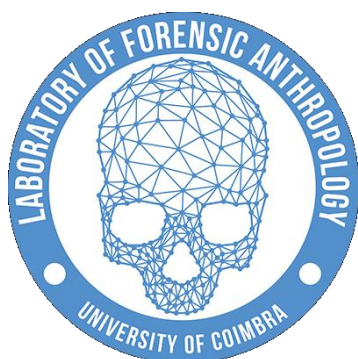
Co-supervisor: Prof. Dr. Maria Paula Matos Marques Catarro

September 2017

University of Coimbra



This dissertation is the result of my original work developed at the Unidade de Química-Física Molecular from the Department of Chemistry of the University of Coimbra, Portugal.



UNIVERSIDAD
DE MÁLAGA



Science & Technology Facilities Council
ISIS

**TAIL- Coimbra Trace Analysis
and Imaging Laboratory**

The bone samples used in this work belong to the 21st century collection of identified human skeletons of the Laboratory of Forensic Anthropology of the University of Coimbra. The Raman experiments with a 785 nm laser line, CARS, FT-Raman and LT-FT-Raman were performed at SCAI from the University of Málaga. X-ray diffraction was performed at TAIL, at the Physics Department of the University of Coimbra. Neutron experiments were accomplished at the ISIS Pulsed Neutron and Muon Source of the STFC Rutherford Appleton Laboratory, UK.

*I am just a child who has never grown up. I still keep asking these 'how' and 'why' questions.
Occasionally, I find an answer.*

Stephen Hawking

Acknowledgements/Agradecimentos

Após terminar este projeto quero agradecer a todas as pessoas que tornaram a sua realização possível.

Ao meu orientador, Professor Doutor Luís Batista de Carvalho e à minha coorientadora, Professora Doutora Maria Paula Marques por tão bem me receberem na Unidade de Química-Física Molecular, pela orientação e ajuda prestada sempre que solicitado, pela confiança que depositaram em mim ao permitirem que desenvolvesse este trabalho de forma autónoma, pelas experiências que me proporcionaram e que contribuíram para o meu crescimento pessoal e profissional.

To Doctor Juan Carlos Otero, for receiving me at the Physical-Chemistry department of the University of Málaga, for his and his co-workers' hospitality. To Cristina Ruano, Jessica Perez and Jose Zafra for all their help and empathy. To Elizabeth, without her my stay in Málaga would not be the same, thanks for showing me Málaga, for all help, ideas and encourage in my fight against fluorescence.

Access to TAIL-UC facilities, funded under QREN-Mais Centro project ICT-2009-02-012-1980, is gratefully acknowledged.

To Doctor Winfried Kockelmann, for his tireless help with GSAS. I would not be capable of doing it on my own, I am very thankful.

Ao Doutor David Gonçalves, pela oportunidade de participar nos seus projetos. À Ana Vassalo, pela ajuda, companhia e ensinamentos durante as longas horas de recolha de amostras. Ao Calil, pela ajuda, disponibilidade, incentivo e boa disposição inabalável.

Ao Professor Doutor Francisco Gil pela disponibilidade e toda a ajuda.

À Professora Doutora Margarida Castro, que sempre me apoiou e aconselhou nos momentos das decisões mais difíceis do meu percurso académico e me mostrou que um professor pode também ser um amigo com quem aprendemos e crescemos imenso.

À Ana Lúcia, por toda a ajuda e disponibilidade incansáveis ao longo deste ano e à Inês Lamego, pela boa disposição e pausas “obrigatórias” para dois dedos de conversa.

Aos meus amigos. Aos de sempre: Nando, JP, Eulália e especialmente ao Daniel. Aos amigos Bioqs que, mesmo longe me apoiaram sempre: Rita, Bruna, Ricardo, Gonçalo, Cláudia, Joana Perdigão, Joana Saraiva e Ana Rita. Aos amigos da química, cuja presença e apoio durante este último ano foi crucial: Ana Tomé, Inês, Sara, Maria Inês e André, obrigada por me “adotarem” e me ajudarem a manter a sanidade mental.

À minha família. Em particular aos meus pais, sem eles nada do que consegui até hoje seria possível; à minha avó que sempre me presenteou com o seu arroz doce nas horas mais críticas de estudo e trabalho. E por fim, mas não menos importante, à minha irmã que, ao longo destes 5

anos, me desencaminhou sempre que possível para sessões de cinema quando eu mais precisava de estudar.

Abstract

Forensic anthropology faces big difficulties in the estimation of the biological profile of burned skeletons once heating induces alterations in shape and dimensions of the bones, seriously compromising the reliability of bioanthropological methods, being urgent to develop a method that allows the estimation of sex, race, stature, age, *peri mortem* traumas, time and temperature of exposure to fire. With this in view, Forensic Anthropology and Forensic Chemistry work together to relate the heat-induced macroscopic alterations with the submicroscopic ones through several analytical methodologies.

In order to understand the extension of the bone submicroscopic thermally induced alterations it is necessary to compare their features with those in the unburned bones. However, intact bones' analysis is in general very difficult due to the presence of the organic constituents. Thus, the first undertaken approach in the present work was to evaluate the efficiency and possible negative effects of a new defatting and deproteinisation protocol using enzymes (lipase and collagenase), being concluded based on FTIR-ATR, XRD and INS data that, although not totally successful, this procedure does not alter bone inorganic component so markedly as petroleum ether/hydrazine treatment, and hence constitutes a potential alternative, after optimisation.

Human femur and humerus bone samples heated under controlled conditions, between 400 and 1000 °C were analysed through FTIR-ATR, Raman and INS spectroscopies, as well as X-Ray and neutron diffraction methods. A gradual loss of type A and B carbonates with an increase in temperature was verified, coupled to an OH increase and the occurrence of a transition mineral phase between 700 and 800 °C, related to the apatite monoclinic-hexagonal polymorphic transition and corroborated by all methodologies applied.

FTIR-ATR showed to be the more adequate and more informative technique for a routine analysis in forensic laboratories, but its coupling with XRD is imperative to attain more complete and reliable conclusions. Further studies, using different types of human bones (from different skeletons) burned under controlled conditions in a wide temperature range, are still needed to evaluate the consistency of these results.

Resumo

A antropologia forense enfrenta grandes dificuldades na estimativa do perfil biológico de esqueletos queimados devido às alterações induzidas pelo calor na forma e dimensões dos ossos, que comprometem seriamente a confiança nos métodos bioantropológicos é, por isso, urgente o desenvolvimento de um método que permita a estimativa do sexo, ancestralidade, estatura, idade, traumas *peri mortem*, tempo e temperatura de exposição ao fogo. É com este objetivo que a Antropologia e Química Forense se unem de modo a relacionar as alterações macroscópicas com as alterações submicroscópicas usando diferentes metodologias analíticas.

Para compreender a extensão das alterações submicroscópicas do tecido ósseo causadas pelo aquecimento é necessário compará-las com as particularidades do osso não queimado (intacto). No entanto, a análise de osso intacto é, geralmente, muito difícil devido à presença dos componentes orgânicos. Por este motivo a primeira abordagem deste trabalho passou por avaliar a eficácia e possíveis efeitos negativos de um novo protocolo de desengorduramento e desproteínização usando enzimas (lipase e colagenase), tendo-se concluído, com base nos resultados obtidos por FTIR-ATR, XRD e INS que, embora não totalmente eficaz, este novo procedimento não altera a componente inorgânica do osso de forma tão marcada como éter de petróleo e hidrazina, representando uma potencial alternativa a estes, após a otimização do protocolo enzimático.

Foram analisadas através de FTIR-ATR, Raman, INS, difração de raios-X e difração de nêutrons amostras de fêmur e úmero, queimadas em condições controladas entre 400 e 1000 °C, tendo-se provado que, concomitantemente ao aumento da temperatura, ocorre a diminuição gradual de carbonatos do tipo A e B, aumento gradual de OH⁻ e a existência de uma fase mineral transitória entre 700 e 800 °C relacionada com a transição polimórfica da biapatite de monoclinica para hexagonal, como corroborado por todas as metodologias aplicadas.

Adicionalmente conclui-se que a técnica mais adequada e também a mais informativa, ideal para uma análise diária nos laboratórios forenses é FTIR-ATR, no entanto, a sua utilização simultânea com XRD é essencial para a obtenção de resultados mais sólidos e completos. Estudos futuros usando diferentes tipos de ossos, de diferentes esqueletos, queimados numa gama de temperaturas mais ampla são necessários para avaliar a consistência destes resultados.

1 Introduction

1. Introduction

Forensic sciences have an imperative role in the application of the law, betting on scientific multidisciplinary: from chemistry, toxicology, genetics, ballistics to anthropology or psychology, serve Justice with its accuracy and precision for a fairer law enforcement.

A forensic autopsy is done when something from the environment is involved in the death, aiming to identify its causes and circumstances. As important as these information about the moment of death, is to identify the deadly victims and return the remains to their families. In any forensic case involving skeletal remains, and sometimes in cases of unrecognisable victims, the pathologists struggle to identify the person and to diagnose the cause of death because they have little training in osteology and anthropology. Forensic anthropologists are fundamental in such situations to extrapolate information from bones.

Forensic anthropology is one of the applications of physical anthropology to forensic settings, which in turn are defined as the application of scientific knowledge to law practices.

The forensic anthropologist primary analysis includes ten questions: “is it bone?”, “is it human?”, “when did the individual die?”, “what bones are present?”, “how many individuals are present?”, “age at death?”, “sex?”, “race?”, “stature?” and “factors of individualisation?”. The first three questions are crucial to either include or exclude forensic anthropologists into the investigation. If it is not bone or it is not human, the forensic anthropologist is no longer needed. On the other hand, there might be in fact human remains but the case may no longer be forensic but, archaeological instead. The criteria for a case to be considered forensic is related to the number of years a homicide takes to expire, which is established by the law of the country where the remains are found. In Portugal, this term is 15 years (Arts. 122° and 131°, Código Penal Português). Hence, if death has occurred for more than 15 years ago the case is considered archaeological.

The last five questions - “age at death?”, “sex?”, “race?”, “stature?” and “factors of individualisation?” - correspond to the estimation of the victim’s biological profile [1, 2], being the basis for individual identification. Additionally, forensic anthropologists look for *peri mortem* traumas that may give some clues on the circumstances of death or even be associated with the cause of death. This analysis is based on osteometry and bone morphology [3–5]. However when the victims are associated to fire contexts, sometimes the job of the forensic anthropologist is more difficult.

According to the World Health Organization (WHO), more than 300 000 deaths occur *per year*, caused by fire [6]. The causes of these fires vary from fortuitous fires, car accidents or mass disasters, to explosions or bombings, and sometimes they are associated to suicides or homicides [7, 8]. In such cases, when soft tissue is highly damaged or even absent it is impossible to use ordinary methods for individual identification: facial recognition and fingerprint analysis [9–11].

1. Introduction

The application of osteometry is possible if the skeleton does not present heat-induced alterations because fire causes color changes, warping, shrinkage/expansion and fragmentation [7, 12–15] leading to bone's shape and dimensions alterations and thus, compromising the reliability of bioanthropological methods [15, 16]. Odontological identification, in turn, is only achievable when *ante mortem* dental records are available [9, 10, 17]. As to genetic analysis, it requires the collection of soft tissue or DNA from bones, the latter being possible only if the skeletal remains are well preserved since DNA is destroyed at high burning temperatures [8, 18, 19] preventing its recovery and further analysis. Moreover, a DNA reference sample from the individual or from a next of kin would be needed. Hence, the development of a new osteometric method suitable for burned human bones is of utmost importance, having special applicability in forensic contexts, but also in archaeological scenarios.

1.1. From Archaeology to Forensics

The study of burned bones goes beyond crime or accident contexts. In archaeology, this field of study is fundamental to understand funerary behaviours, as well as cooking practices. Actually, the study of archaeological burned remains, from different animals but also from humans, was the precursor of the research of burned bones associated to forensic settings.

Some studies are mainly based on macroscopic alterations, because it is so important to maintain the remains intact in both areas (archaeology and forensic anthropology). In the highlight of archaeology, the occurrence of warping and thumbnail fractures [13], colour differences and mechanical bone alterations [12], bone loss, colour changes, shrinkage and weakness, and microscopic bone surface variations in rabbit bones [20], allowed to infer about corpses' preservation when exposed to heat, the temperature and duration of the exposure, and the sequence of burial and cooking events.

Concerning a forensic application of the above conclusions, Gonçalves *et al.* [21] studied bone warping and thumbnail fractures in both human cadavers and skeletons, concluding that they are more frequent in cadavers, but can also be detected in dry bones. Consequently, none of these changes is a particularly reliable indicator of pre-burning conditions (warping being potentially more useful). A study by Keough *et al.* [22] using pig models led to the evaluation of heat-induced features (heat borders, heat lines, joint shielding, brown burning and delamination) in bones at different decomposition stages. These authors concluded that bone colour distribution depends on the level of decomposition (fleshed or partially fleshed, wet or dry) when exposed to fire: the absence of heat borders, heat lines, and joint shielding are common in early decomposition stages; delamination and fractures often occur for higher decomposition stages, while parameters such as the duration of fire exposure or the amount of soft tissue in the bone may determine the number of

fractures. Although the differences between human's and pig's anatomy, way of locomotion and texture and quality of the bones may influence the observed burn patterns, this study provided valuable information on fire induced changes in corpses at different stages of decomposition, that will certainly be useful in future studies of human remains.

Although macroscopic alterations caused by fire may give clues about the sequence of events after death, namely the pre-burning conditions, the maximum temperature reached and the duration of the fire, they are not reliable indicators of the exact burning conditions since each heat-induced feature is not exclusive to one combustion parameter, that is influenced by several factors not yet totally understood.

Searching for answers, this field of research started to take advantage of analytical methods based on the premises that macroscopic changes observed in bone may be the result of other fundamental microscopic variations, possibly bone's chemical structure (crystallinity), organisation and composition [13, 23–27]. This is where Forensic Chemistry comes into place.

1.2. Bone composition

Bone is a heterogenous material, containing inorganic and organic constituents, apart from water: from the total bone's weight, 60% is ascribed to the inorganic phase (increasing to 70% in dry bone), 25% to the organic components and 9,7% to water [28–32]. The organic phase comprises lipids and proteins (mainly type I collagen) and a remaining 2% representing varied cellular constituents [29, 30, 33].

The inorganic phase is a hydroxyapatite analogue mineral, named bioapatite, of approximate formula $\text{Ca}_{10}(\text{PO}_4)_{6-x}(\text{OH})_{2-y}(\text{CO}_3^{2-})_{x+y}$, exhibiting plate-like crystals 20 to 80 nm long and 2 to 5 nm thick [29], partly substituted by carbonate.

In vivo, as schematically represented in Figure 1.1, carbonates (CO_3^{2-}) can substitute for the phosphate groups (PO_4^{3-}) in bioapatite (type B substitution) or for the hydroxyl groups (OH^-) (type A substitution, much less common) [34–36]. Once CO_3^{2-} groups have a different charge and geometry than PO_4^{3-} moieties, and are much bigger than the OH^- groups, their presence in the crystal lattice generate distortions that lead to a decrease in bioapatite's crystallinity [25, 36, 37]. Apart from these substitutions, bioapatite's crystal lattice may contain water and ions such as calcium (Ca^{2+}), sodium (Na^+), magnesium (Mg^{2+}), strontium (Sr^{2+}), potassium (K^+), fluorine (F^-) or chlorine (Cl^-) [25, 26, 28, 30, 38]. The individual proportion of each bone constituent, as well as its geometric and spatial arrangement, depend on numerous factors, namely: diet taken during the lifetime, metabolism, pathologies, age at death, *post mortem* period and environmental factors such as the type of soil in contact with the remains [39].

1. Introduction

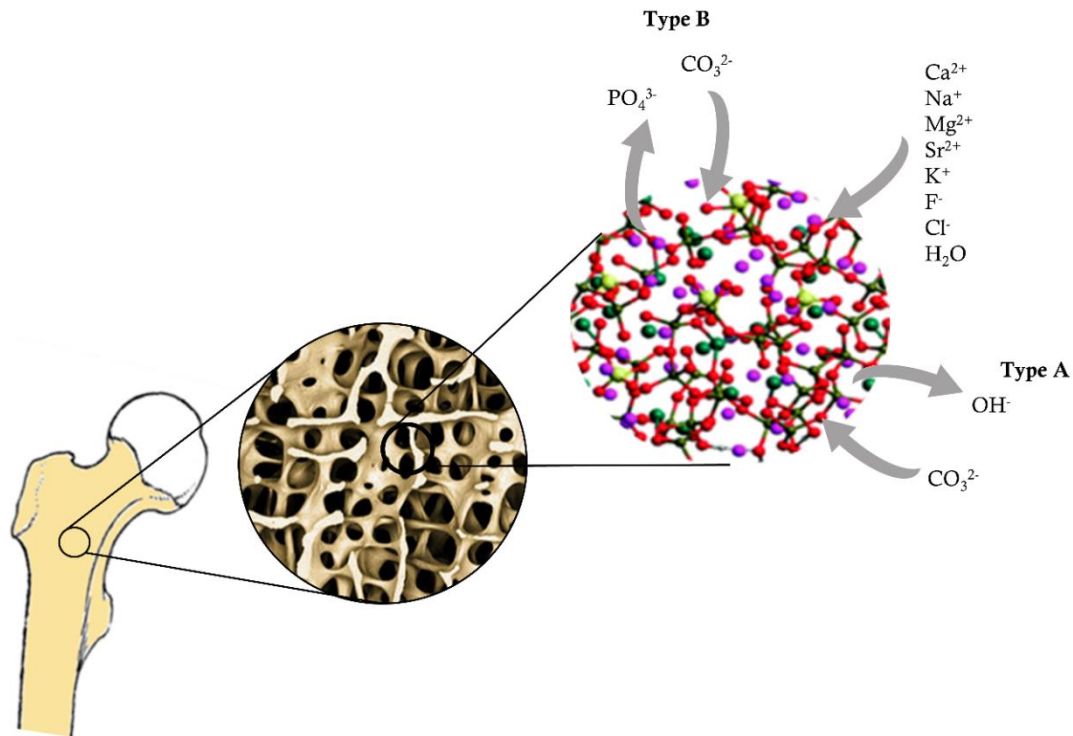


Figure 1.1. Representation of chemical substitutions in bioapatite crystal lattice.

Thus, bioapatite has a lower crystallinity than hydroxyapatite due to its high carbonate substitution degree, that is responsible for small sized crystals, with a high structural strain (caused by the distortions and defects within the crystal lattice), a high surface area and an increased solubility in water [31, 40]. These features confer particular characteristics to the bone matrix, such as resistance and flexibility, and contribute to the organism's mineral homeostasis [29, 30]. In addition, lower crystallinity renders bones susceptible to *post mortem* alterations caused by heat or environmental factors (*e.g.* contact with surrounding fluids) [26].

1.3. Diagenesis

Crystallinity is an indicator of the size and atomic order of a crystal. After death, bioapatite becomes less reactive and its crystallinity increases due to diagenesis, that includes spontaneous recrystallisation related to collagen decomposition (following exposure of bioapatite's crystals to the surroundings) and loss of carbonate coupled to fluorine uptake [41–43]. During the burning process, several events similar to diagenesis occur, concomitant with the loss of water and carbonate from the crystal lattice: with increasing temperatures, bioapatite becomes analogous to the geological form of hydroxyapatite, with bigger crystals, higher levels of crystallinity and lower porosity [25, 31].

Naturally, the three main components of bone tissue are differently affected by heat [23, 41, 44]. Thompson [15] has defined four different phases for heat-induced changes: i) dehydration, between 100 and 600 °C; ii) decomposition, 300 - 800 °C; iii) inversion, 500 - 1100 °C; iv) and fusion, above 700 °C. Etok *et al.* [24] further detailed these four phases: 25 – 250 °C loss of poorly bounded water up to 100 °C and of structural water from proteins and mineral surface-bounded H₂O up to 250 °C; 300 - 500°C combustion of about 50% of the organic phase, increase of crystal size (from *ca.* 10 nm to 30 nm) and crystal thickness (from *ca.* 2 nm to 9 nm), and formation of new mineral phases (NaCaPO₄, NaCl and KCl); above 500 °C loss of the remaining organic components, growth of crystal size to 110 nm and of crystal thickness to 10 nm, at 800 °C; loss of intercrystallite space, at 900 °C; above 1000 °C, formation of β -tricalcium phosphate (Ca₃(PO₄)₂). So, the first CO₂ release takes place between 250 and 500 °C as the result of organic component combustion, while the second fraction of CO₂ is released at *ca.* 500 °C consistent with structural carbonate loss [24, 25, 45]. Bioapatite's crystalline structure starts to be affected by heat solely above 500 °C, on account of an organic matrix thermal shielding effect that protects the inorganic moiety leaving only crystals' surface exposed to heat after its destruction [24, 31, 45].

Figure 1.2 summarises the heat-induced alterations described above, including colour changes (according to Shahack-Gross *et al.*, Shipman *et al.* and others [27, 46, 47]).

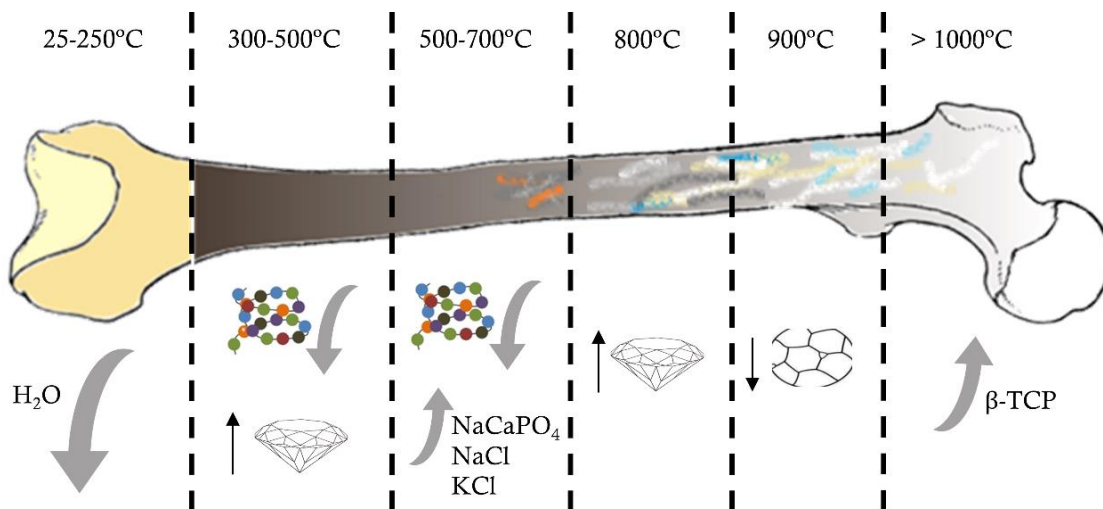





Figure 1.2. Schematic representation of heat-induced changes in human bone, for the temperature range 25 to 1000 °C. Upper part: colour alterations. Lower part: sub-microscopic variations.

Symbols: loss ↘ ; appearance ↗ ; decrease ↓ ; increase ↑ ; organic matrix  ; crystal thickness and length  ; intercrystallite space .

1. Introduction

Knowing that: a house on fire can reach 700 °C, a car on fire may reach between 900 to 1100 °C, a fire storm 2000 °C and an explosion caused by strong explosives (such as TNT, C4, nitroglycerine, dynamite and others) can reach 3000 °C [48, 49]; and organic material is seen to totally burn out above 500 °C, it is especially important to understand the inorganic matrix behaviour, as temperature increases once it is what remains.

1.4. Methodologies

Analysis of bone microstructure may be a difficult and challenging process, even more with all the possible changes (macroscopic, microscopic and submicroscopic) thermally induced. Once the main purpose of forensic researchers is to find a method that allows a rapid and reliable estimation of biological profiles leading to individual identification, the selection of techniques to successfully achieve this goal should follow defined parameters: equipment accessibility, maintenance costs, data acquisition time, small amounts of sample needed, non-destructive analysis, virtually no sample preparation, and ease of data analysis.

In the light of these criteria, and knowing that forensic laboratories are usually equipped with Raman and FTIR apparatus, vibrational spectroscopic techniques have become increasingly important in this field since they provide information on thermally induced changes in both organic and inorganic bone constituents (including crystallinity). Based on infrared data has been reported the: decrease in organic constituents [23, 45], increase in crystallinity up to 700 – 800 °C [25, 28, 45, 50, 51], decrease in B carbonates [25, 52], increase in A carbonates and OH⁻ content [25]. Based on Raman spectroscopic results it has been described the: increase in maturity/crystallinity [53, 54], expected decrease in carbonates content and the decrease in organic constituents [55]. In addition, inelastic neutron scattering (INS) spectroscopy can yield extremely useful data as it affords an unprecedented access to vibrational features unattainable by optical techniques (FTIR and Raman), thus allowing to attain the complete vibrational profile of bone samples by combination with infrared and Raman data. The described alterations as consequence of temperature exposure prove OH⁻ presence in bone lattice as well as its increase as temperature increases [44, 56]. This is essential for an accurate understanding of all modifications undergone within the bone matrix upon heating. In turn, diffraction methods, both conventional X-ray (XRD) and neutron [57–59] based, deliver crucial information on the crystal parameters, as well as on the chemical composition of the crystal lattice (including the localisation of the hydrogen atoms, when using neutron diffraction). Being stated the observed increase in crystallinity and crystals' length and thickness followed by mineral structure transitions above 600 °C [24, 26, 38, 60–62].

1.4.1. Vibrational Spectroscopy

Atoms within molecules are never motionless, they oscillate around their equilibrium positions [63], changing bond lengths and angles - these vibrational modes are called stretchings and bendings, respectively [64]. A vibrational spectrum results from transitions between quantised vibrational energy states, each fundamental vibrational mode, i , that involves nearly harmonic displacements of the atoms, corresponding to a characteristic frequency, ν_i [63, 65]. However, only a few atoms have larger movements (the functional groups), with characteristic frequencies, which stand out relatively to the remaining vibrations. The nature of the atoms nearby these functional groups affect their vibrational modes' frequency [65], *i.e.* the same chemical bound in different atomic environments will vibrate differently allowing the assessment of information about structural alterations.

1.4.1.1. Fourier Transform Infrared Spectroscopy

Infrared (IR) spectroscopy is based on the absorption of electromagnetic radiation at frequencies matching the vibrational modes of the molecule, *i.e.* the incident light with the same energy of a specific vibrational transition is absorbed, originating a spectral band [64–67]. However, absorption on the IR range, only occurs if, during the vibration, a change in the molecular electric dipole moment occurs: when electromagnetic radiation, with matching frequency to a vibrational motion, interacts with the fluctuating dipole moment of the molecule and is absorbed [63, 64].

The IR spectral region can be divided into far-IR ($<200\text{ cm}^{-1}$), mid-IR ($200 - 4000\text{ cm}^{-1}$) and near-IR ($4000 - 13000\text{ cm}^{-1}$). The mid-IR region is more commonly used since most of the fundamental vibrations occur between 400 and 4000 cm^{-1} . In turn, far-IR region is relevant for the study of molecular skeleton or torsional vibrations, crystal lattice modes, and stretching modes associated to hydrogen bonds, as well as molecules containing heavy metals [64, 68]. The near-IR interval, in turn, comprises overtones (multiples of fundamental vibrational frequencies) and combinations of fundamental modes [63, 64].

Fourier Transform Infrared in Attenuated Total Reflection (FTIR-ATR) mode is an alternative to the conventional FTIR transmission mode. In transmission mode the light passes through the sample [64], which is contained within a pellet of an IR transparent support medium, usually KBr (for mid-IR). This process comprises grinding in a mortar and applying pressure to form the pellet (that should be homogenous). Apart from the time required for preparation, the sample is not recoverable (although the amount needed is very small). Moreover, Thompson *et al.* [69] and Surovell and Stiner [70] found this sample handling in FTIR-KBr analysis, namely grinding, introduces alterations in bone crystallinity. In ATR mode the radiation beam enters a

1. Introduction

crystal with a high reflection index and is internally reflected if the angle of incidence in the sample-crystal interface is greater than the critical angle [64, 71], as represented in Figure 1.3. Interaction between the radiation and the sample occurs on this surface and is dependent on the sample's characteristics and on the environment. This is a particular suitable technique for rapid and non-destructive analysis of powders since it does not require any type of solvent or support medium, what reduces considerably sample preparation times, and the amount of sample needed is very low (<1 mg).

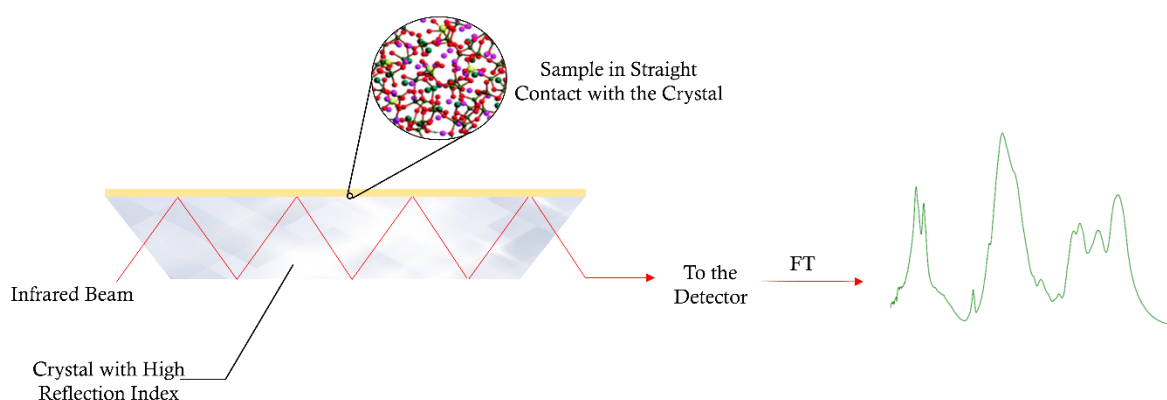


Figure 1.3 Schematic representation of an FTIR-ATR experiment.

Hence, FTIR-ATR appears to be a reliable and quite appropriate technique for bone analysis, as corroborated by Beasley *et al.* [41]. In comparison to FTIR-KBr, it is a better technique to analyse powder samples because it diminishes distortions caused by optical saturation and dispersion, and it is free of chemical sample alterations (water adsorption and ion exchange) possibly produced during KBr pellet preparation [72].

Despite the fact that both techniques give the same chemical information about the sample, Beasley and coworkers [41] found that differences in resolution between FTIR-KBr and ATR spectra do not allow the comparison of the spectroscopic indices (see Table 2.2, in the next chapter) obtained from these different techniques.

Furthermore, ATR spectra present distortions of the relative peak intensities in comparison to those acquired in transmission mode, since the depth of penetration by the incident radiation is dependent on its wavelength. Moreover, an effect known as anomalous dispersion leads to peaks shifting, because the refraction index of the sample undergoes quick changes nearby an absorption peak [73]. Therefore, an ATR correction function should be applied, that removes these effects from the spectra rendering their comparison possible with those obtained in transmission.

The biggest obstacle regarding IR spectroscopic analysis is the interference of H₂O and CO₂, whose signals may override relevant sample spectral information in the 2000 - 4000 cm⁻¹ range. This problem, however, is easily overcome using a purged FTIR apparatus.

1.4.1.2. Raman Spectroscopy

Raman spectroscopy is a complementary technique to IR spectroscopy, the physical process giving rise to the vibrational bands being different (with distinct selection rules): Raman inelastic light scattering *vs.* infrared light absorption [63].

Scattering corresponds to deflection of light from the direction of the incident beam. When the electromagnetic radiation interacts with a polyatomic molecule, a periodic perturbation of the electron clouds are induced and an oscillating electric moment is produced. Scattered light is, in reality, emitted radiation by this induced oscillating dipole moment, *i.e.* electrons can couple with photons and induce scattering [63]. This process may be either elastic (Rayleigh scattering) – the scattered light has the same frequency (ν_0) as the incident one - or inelastic (Raman scattering), involving a change in energy either higher ($\nu_0 + \nu_{\text{vib}}$) or lower ($\nu_0 - \nu_{\text{vib}}$) relative to the incident radiation (respectively, anti-Stokes Raman scattering or Stokes Raman scattering, as represented in Figure 1.4). The vibrational energy difference (ν_{vib}) is the same in both processes, *i.e.* the energy difference between the incident and scattered light is equal for either Stokes or anti-Stokes process. The later, however, yields less intense bands, since, it corresponds to an initial transition from an excited state (Figure 1.4.) which has a lower population than the ground one, thus giving rise to a less intense scattered signal. As a consequence, the Stokes Raman scattering is the one normally detected in Raman experiments. It should be noted that Raman is a very weak process, only a very small fraction of the incident light (10^{-6} for solids) undergoing inelastic scattering [63].

In sum, the Raman effect is the result of an oscillating induced dipole moment, resulting from the interaction between the electric field of the incident electromagnetic wave (*i.e.* the incident monochromatic light beam, nowadays a laser) and the molecular polarizability of a particular molecular vibration. Therefore, vibrational modes will be Raman active if they involve a change in the shape of the electron cloud.

Some vibrational modes will then be visible (active) in Raman but not in IR and vice-versa. In order to access the complete vibrational profile of a sample, both Raman and infrared analysis are needed [65, 74] (as well as neutron vibrational techniques, if possible, see sub-chapter 1.4.1.3).

The main advantages of Raman spectroscopy are: i) virtually no sample preparation; ii) small amount of sample needed; iii) non-destructive (the sample is completely recoverable) and non-invasive; iv) high specificity; v) high spatial resolution, mainly when using microspectroscopy setups (coupling Raman scattering and optical microscopy [75]). On the other hand, the major

1. Introduction

handicap of the technique is its quite low sensitivity and the interference from fluorescence. This determines the choice of the excitation source, the Raman differential scattering cross-section (σ) being proportional to the fourth power of the incident laser frequency [$\sigma \propto (\nu_0 - \nu_{\text{vib}})^4$], which favours the use of ultraviolet or visible light sources in order to increase the signal intensity. However, care must be taken in order to avoid fluorescence emission upon light absorption, as the former is a much more intense process than inelastic scattering and can completely overrule the Raman bands of the sample.

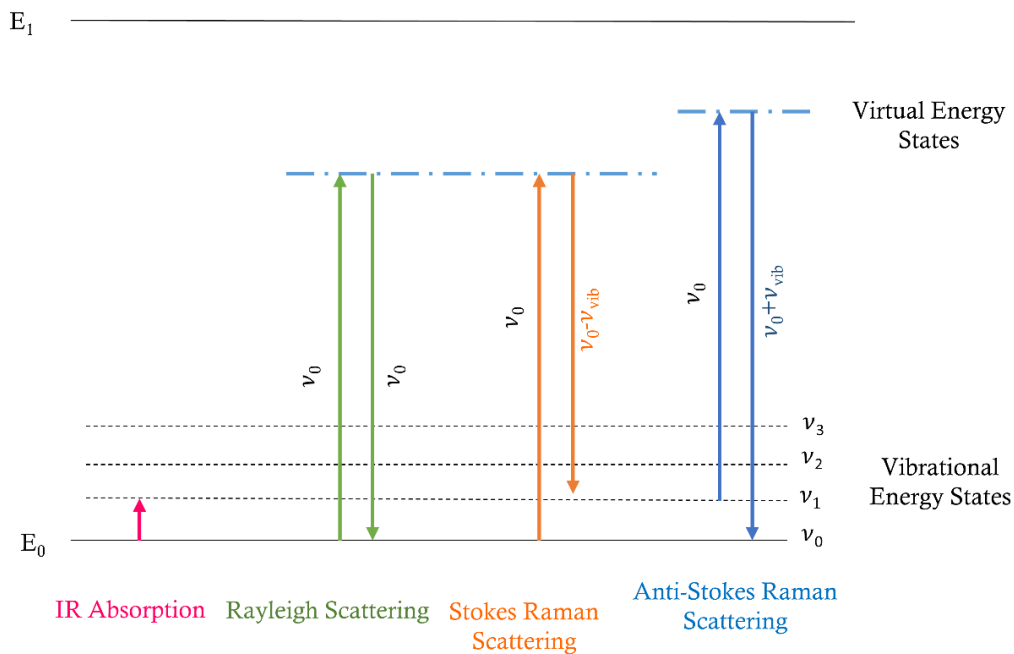


Figure 1.4. Schematic representation of the vibrational transitions corresponding to IR absorption and light scattering – Rayleigh and Raman (Stokes and Anti-Stokes).

Bone tissue analysis using Raman spectroscopy faces serious obstacles, mainly due to the presence of fluorophores within the bone matrix (mainly for intact bone) [76, 77]. Apart from lipids, collagen is the main organic component of bone and is a strongly fluorescent molecule [77, 78]. In turn, non-collagenous proteins containing aromatic aminoacids (tyrosine, tryptophan or phenylalanine) are also highly fluorescent [78]. With a view to overcome this problem, some measures are in use:

- Purification of the sample – if bone organic matrix is not the focus of the study, one possible approach to eliminate fluorescence is to remove it from the sample. Defatting and deproteinisation protocols are discussed below, in sub-chapter 1.5.

- Bleaching - either photobleaching - photochemical destruction of the fluorophore(s) by prolonged exposure of the sample to the laser beam [63] - or chemical bleaching - removal or significant damage of the fluorophore by treatment with organic solvents. Although chemical bleaching effectively reduces fluorescence, it may also damage the sample [76, 79]. Photobleaching, in turn, is still a ill understood phenomenon, thought to involve photon induced chemical damage and chemical changes within the fluorophore that, lead to quenching [79]. Nevertheless, photobleaching can also cause sample damage: Golcuk et al. [76] found that prolonged photobleaching of dry bone prompted variations in the area of mineral to matrix bands, and suggested that this might be due to photolysis of collagen cross-links or to dehydration upon continuous laser incidence (leading to heating).
- Choice of excitation wavelength - once fluorescence emission strongly depends on the excitation wavelength, a careful selection of the excitation source may avoid (or at least decrease) fluorescence interference [63]. Yet, one should keep in mind that, as discussed above, high wavelength lasers give rise to less intense Raman signals. In bone analysis, laser beams are typically within the range 514 to 1064 nm [80], the latter being used in Fourier Transform Raman instruments (FT-Raman).
- Coherent Anti-Stokes Raman Scattering (CARS) – the CARS effect is a four photon process based on a non-linear optical technique that yields Raman data in the anti-Stokes region with an improved signal strength. Two colinear lasers with different frequencies are used: the pump laser, with a stationary frequency, ($\omega_{\text{pump}} = \omega_{\text{probe}}$) and the Stokes scanning laser (ω_{Stokes}). These two radiations interact with the sample generating photons inelastically scattered within the anti-Stokes frequency region according to equation (1):

$$\omega_{\text{anti-Stokes}} = \omega_{\text{pump}} + (\omega_{\text{probe}} - \omega_{\text{Stokes}}) = \omega_{\text{pump}} - \omega_{\text{Stokes}} + \omega_{\text{probe}} = 2\omega_{\text{pump}} - \omega_{\text{Stokes}} \quad (1)$$

In case of collinear geometry of excitation, the light with frequency $\omega_{\text{anti-stokes}}$ is emitted in the forward direction, colinear to the laser beams, as the result of inelastic scattering of the sample [63, 81, 82]. With the use of these two colinear lasers, most molecules will be prompted into a virtual excited state and when relaxing to the ground electronic state the emitted radiation will be more energetic than the incident beam, resulting in anti-Stokes Raman scattering, as represented in Figure 1.5.

If the frequency difference $\omega_{\text{pump}} - \omega_{\text{Stokes}}$ matches a vibrational frequency transition (ω_{vib}), the signal obtained is approximately four orders of magnitude stronger than conventional Raman scattering. Besides the enhanced signal, the anti-Stokes region is blue shifted and thus is spectrally free of fluorescence background [63, 82, 83]. This feature renders CARS a very attractive technique for medical and biochemical purposes and might

1. Introduction

be a possible approach to eliminate fluorescence during Raman analysis of bones and teeth in forensic and archaeological sciences.

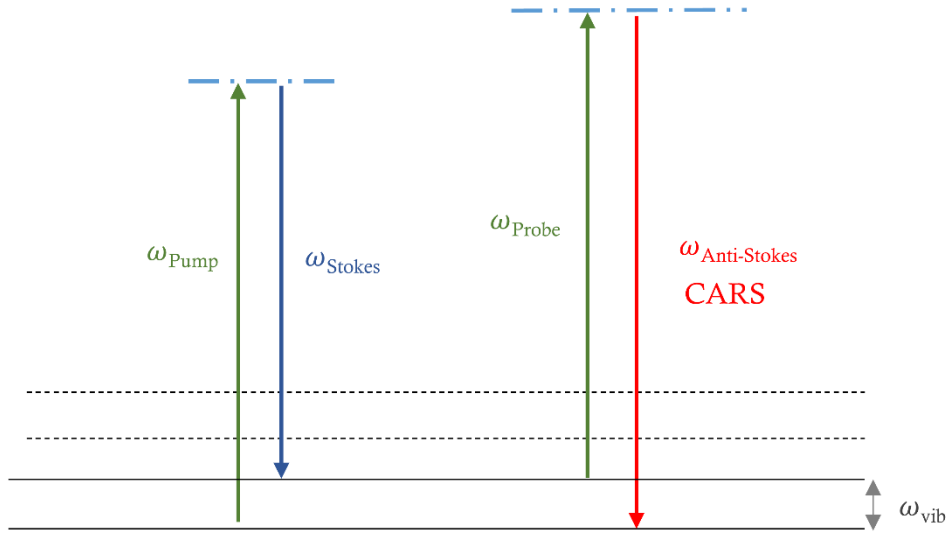


Figure 1.5. Representation of the vibrational transitions involved in the CARS effect.

1.4.1.3. Inelastic Neutron Scattering Spectroscopy

Inelastic neutron scattering (INS), as FTIR and Raman optical techniques, is a vibrational spectroscopy method very useful for attaining a complete vibrational profile of a system (by coupling all three techniques). In this case, a neutron beam is applied to the sample and interacts with the nucleus, undergoing inelastic scattering [84, 85] and generating an INS signal that results from the energy difference between the scattered neutron and the neutron beam (that matches the energy of the vibrational mode), similarly to the optical Raman scattering process. Obviously, optical rules do not apply when using neutrons as an excitation source. In other words, as neutron's mass is 2000 times greater than that of the electron, the inelastic scattering event involves not only energy transfer (E, cm^{-1}) but also momentum transfer ($Q, \text{\AA}^{-1}$). The momentum, $Q = k_f - k_i$, depends on the wavevector, k , defined as:

$$k = \frac{2\pi}{\lambda} \quad (2)$$

where λ is the wavelength of the incident neutron [86]. These wavelengths are within the scale of internuclear distances, contrary to optical spectroscopy where the photon wavelength is larger than the charge distribution alterations associated to excitation [87, 88]. So, k assumes a very small

value for any scattering angle and Q is also very small. Thus in both Raman and IR only the vibrational transitions at zero wavevector are visible [86] while in INS every wavevector is observable and, consequently, every vibrational mode can be detected.

The experimentally measured scattered function is defined as:

$$S(Q, \omega) = \sigma Q^2 U^2 \omega^{-Q^2 U^2} \quad (3)$$

where σ is the scattering cross section, Q is the momentum transfer in \AA^{-1} , and U is the amplitude of the vibration in \AA ($U^2 = h/4\pi\mu\omega$, h being the Plank's constant, μ the mass of the oscillator, and ω is the oscillator frequency) [85, 87].

Since the scattering function is dependent on the cross section of the nucleus, the bigger the cross section the more intense the INS signal. This is why the technique is particularly informative for groups containing a high amount of hydrogen atoms, as H's cross section is *ca.* 20 times greater than that of all other elements [56, 87] – INS spectra are dominated by data on sample's hydrogen content. Also, hydrogen scatters neutrons isotropically because it is much smaller than the wavelength of the radiation [84].

The greatest advantages of INS spectroscopy are: (i) absence of selection rules; (ii) peak intensities (represented by the scattering function) are directly proportional to the number of scattering atoms and vibrational amplitudes [56, 85, 87]; (iii) the neutron radiation is highly penetrating and the scattering is strongly sensitive to isotopic substitution. In turn, the biggest drawbacks of the technique are: (i) the fact that it is extremely costly and can only be carried out at dedicated facilities, since it relies on the generation of an efficient neutron beam either in spallation sources or in nuclear reactors; (ii) significant amount of samples is needed (1-6 g) [85, 89, 90]. Hence, INS analysis is only performed when other techniques are inadequate or don't provide all the information needed about the sample.

INS has a critical role in bone analysis, namely to confirm the presence of hydroxyl groups in the hydroxyapatite's crystal lattice [44, 56, 87, 91]. Still, as bone matrix also comprises lipids and proteins (with many hydrogen atoms) it is impossible to obtain reliable INS information on the bone's inorganic matrix lattice without prior removal of these organic components (that would overrule bioapatite's signals) [44]. Although INS is an extremely suitable technique for the study of structural changes in bone, it has been seldom used, the works by Taylor *et al.* [56] and Marques *et al.* [44] being some of the few reported studies in animal and human bone based on combined INS, FTIR and Raman measurements. The latter [44], was the first investigation of heat-induced alterations in human bones by inelastic neutron scattering.

Table 1.1 comprises the main infrared, Raman and INS vibrational wavenumbers detected for human bone samples present in literature.

1. Introduction

Table 1.1. Main infrared, Raman and INS vibrational wavenumbers for samples of human bone.

IR	Raman	INS	Assignment	Reference
		4246	Comb (OH ⁻ libration + $\nu(\text{OH}^-)$)	[44]
3573	3572	3585	$\nu(\text{OH}^-)$ (HAp)	[32, 44, 87, 92]
3300		3385	$\nu(\text{OH}^-)$ (water)	[44]
2960-2850	2978, 2940, 2882	2974	$\nu(\text{CH})$ (lipids)	[44, 93]
		2560	3 rd overt (OH ⁻ libration)	[44]
2010			Cyanamide	[25, 94]
		1941	2 nd overt (OH ⁻ libration)	[44]
1660	1616-1720	1665	Amide I (collagen)	[44, 55, 93]
1650		1650	$\delta(\text{HOH})_{\text{water}}$	[44]
1540-1580		1550	Amide II (collagen)	[44, 95]
1540			$\nu_3(\text{CO}_3^{2-})_{\text{A}}$	[45]
1494	1003		$\nu(\text{Phe})$	[55, 92, 93]
		1300-1310	1 st overt (OH ⁻ libration)	[44]
1460	1440-1460	1460	$\delta(\text{CH}_2)_{\text{lipids}}$	[44, 80, 96]
1450			Carbonates (A+B)	[25]
1415			$\nu_3(\text{CO}_3^{2-})_{\text{B}}$	[96]
1242	1215-1320	1242	Amide III (collagen)	[44, 54, 93]
1090 (sh)			$\nu_3(\text{PO}_4^{3-})$ (presence of fluorapatite)	[97]
	1070		$\nu_1(\text{CO}_3^{2-})_{\text{B}}$	[98]
1035	1046		$\nu_3(\text{PO}_4^{3-})$	[56, 92, 99]
	1100		$\nu_1(\text{CO}_3^{2-})_{\text{A}}$	[98]
1005	1005		$\nu_1(\text{HPO}_4^{2-})$	[95, 98]
960	960		$\nu_1(\text{PO}_4^{3-})$	[56, 80]
911	921, 855		$\nu(\text{C-N})_{\text{Pro}}$ (collagen)	[92, 93]
878			$\nu_2(\text{CO}_3^{2-})_{\text{A}}$	[35, 100, 101]
872			$\nu_2(\text{CO}_3^{2-})_{\text{B}}$	[35, 100, 101]
700 _w			$\nu_4(\text{CO}_3^{2-})$	[56]
700			Cyanamide	[25, 94]
710			CO (CaCO ₃)	[99]
630		650	OH _{libration} (HAp)	[44, 56, 102]
565, 603	578-617		$\nu_4(\text{PO}_4^{3-})$	[80, 92, 95]
547 <i>sh</i>			β -TCP	[103]
470	422-454		$\nu_2(\text{PO}_4^{3-})$	[54, 56, 80, 92]
343, 355 <i>sh</i>	329		$\nu_3(\text{Ca-OH})$	[104]

337	335	OH _{translation} (Hap);	[105, 106]
0-300	0-320	(Ca-PO ₄) _{translation / lattice modes} ; PO ₄ ³⁻ _{librations}	[104, 105, 107]
	250	CH ₃ torsion (proteins)	[44, 56]
228		ν_2 (Ca-OH) _{lattice modes}	[104]

**sh* shoulder; *w* - weak; *comb* - combination mode; *overt* overtone; β -TCP - β -tricalcium phosphate; δ - in plane deformation; ν - stretching; (CO₃²⁻)_A A type carbonate, (CO₃²⁻)_B B type carbonate.

1.4.2. Diffraction Methods

Diffraction is a phenomenon that occurs whenever a coherent wave is targeted onto a set of objects equally spaced, visible when the wavelength of the incident wave is of the same order of magnitude than the distance between the objects [108]. Diffraction occurs due to the interference between distinct reflected waves dependent on differences in the path travelled by the radiation, which results in variations on the amplitude – hence, path and phase differences are directly proportional.

Electromagnetic waves or particles may be used in diffraction methods, such as X-rays, neutrons and electrons [109].

In crystalline materials, atoms are equally spaced and display defined patterns, yielding a *unit cell* that is periodically repeated in three dimensions (of the same order of some Ångstroms). This renders them ideal candidates for analysis by diffraction methods [108, 109]. As the diffracted beam comprises many scattered rays and differences in the path travelled by these are related to the space between the different atoms, diffractograms reflect the crystal structure being characteristic and unique of each crystalline compound (a fingerprint), thus allowing its unmistakable identification.

1.4.2.1. X-Ray Powder Diffraction

A crystalline sample diffracts X-rays according to the Bragg law,

$$\lambda = 2d\sin\theta \quad (4)$$

for a crystal lattice with its planes equally spaced at a distance d' , a beam of perfectly monochromatic X-rays, of wavelength λ , parallel to the crystal planes, incident on the crystal at an angle θ (Bragg angle). Only the diffracted rays that are in phase with each other will constructively contribute to the diffracted beam [108].

1. Introduction

In order to carry out structure analysis of crystals by X-ray diffraction, Bragg's law is applied using X-rays of known wavelength (λ), measuring θ and thus determining the value of d , the space between different planes in the crystal. The orientation of these lattice planes, in turn, is described by indices that are the reciprocals of the fractional intercepts of the plane with the crystallographic axes, defined as (hkl) , so if the axial lengths of the plane are a , b and c , the plane makes fractional intercepts at a/h , b/k and c/l , and each plane will diffract X-rays with a different angle (θ) [108]. As inferred by Bragg's law, the glancing angles θ at each plane diffracting X-rays, depend on the interplanar spacing d , which is determined by the dimensions of the crystal lattice. This means that the atom arrangement in the lattice does not influence the positions of the X-ray reflections and consequently two chemically different compounds with similar crystal dimensions will have analogous X-ray diffractograms [110]. This feature is very useful in case of bioapatite and hydroxyapatite that become similar at some point upon thermal exposure.

For powder methods, as opposed to crystal analysis, the sample is reduced to a fine powder in order to have small crystals randomly oriented. Ideally, the highest number of different crystal orientations should be present so that, by chance, there are a few with a correct orientation for satisfying Bragg's law. In other words, considering a certain hkl reflection, a few crystals will have their (hkl) planes oriented with the correct Bragg angle for diffraction [108].

The biggest limitation of the XRD method is the fact that amorphous materials are unable to diffract X-rays. In turn, it is a non-destructive technique, sample preparation is straightforward, short acquisition times are needed and data analysis is usually simple.

1.4.2.2. Neutron Diffraction

Neutrons are neutral particles present in the nucleus of the atom, that easily penetrate most materials and can be scattered by nuclei and magnetic fields, as discussed above (sub-chapter 1.4.1.3). In neutron diffraction methods, the neutron beam is produced in a nuclear reactor or in a spallation source (that involves previous particle acceleration in a synchrotron) and must be "monochromatic" (all the neutrons in the beam have the same velocity) [109]. Similarly to X-ray diffraction, the process of neutron diffraction must follow Bragg's law.

The major difference between these two methods is that while X-rays interact with the electron cloud, providing information on the crystal lattice based on electron density (that suffers interferences from chemical binding), neutron radiation interferes with the nuclei within the sample, with both energy and momentum transfer. Hence, it depends on the atomic number (Z) and the nuclear energy levels of the sample. Information about the nuclear density can thus be obtained, including nuclear positions, and it is possible to distinguish elements with a diffraction amplitude far from the average [108, 109].

The biggest disadvantages of neutron diffraction are basically those previously mentioned for INS: an expensive technique that can be used only at dedicated facilities, and a reasonably high amount of sample needed. The advantages, in turn, when comparing with X-ray diffraction, are the high penetrating ability of the neutron beam, the dependency of the signal intensity as a function of the atomic number thus yielding information on both chemical composition and structure [108, 109].

Due to the incoherent scattering of hydrogen, mainly present in collagen and lipids, neutron diffractogram signals' are less intense and with low resolution [57]. So, once again, to analyse unburned bone samples it is necessary to remove its organic component.

1.5. Removal of Organic Constituents

As mentioned before, the vibrational bands due to bone's organic constituents largely overlap the vibrational spectral information from the inorganic components (hydroxyapatite). In the case of Raman spectroscopy, intact bone analysis is rendered even more difficult due to fluorescence from collagen and lipids.

Regarding removal of the bone's lipid constituents, Taylor *et al.* [56] suggested a defatting process with petroleum ether, which would improve further deproteinisation (collagen removal). Alternatively, a chloroform/methanol solution can be used, as proposed by Shapiro [111]. Both methods are commonly applied to bone treatment, no negative effects on the mineral lattice having been reported to this date.

Concerning deproteinisation, several protocols are available, namely with ethylenediamine [112, 113], sodium hypochlorite [113, 114], , hydrochloric acid [114], hydrogen peroxide [115], or by simply heating [32, 57, 62]. In addition, Termine and coworkers [116] suggested a deproteinisation method using hydrazine, alternatively to ethylenediamine, which has been used by many researchers since then [35, 44, 56, 87, 117]. Nevertheless, hydrazine deproteinisation has been questioned regarding its effectiveness and impact on the inorganic bone matrix, namely the loss of carbonate and acid phosphate during the procedure due to their high solubility, as well as alterations in crystallinity (possibly caused by exposure to hydrazine at 55°C) [118, 119].

Bertazzo and Bertran [118] tested hydrazine action in different calcium phosphate compounds such as, hydroxyapatite, CaHPO_4 , CaCO_3 and bone (from different animals) having conclude that bone mineral composition and morphology was not altered upon hydrazine exposure but some evidence of minor crystallinity changes were observed. From the calcium phosphates tested, CaHPO_4 showed to be the most affected by hydrazine treatment. Regarding hydrazine's efficacy for deproteinisation, these researchers detected only minor quantities of protein (less than 4%) in bone samples after the process, proving hydrazine effectiveness. Karampas *et al.* [119], in

1. Introduction

turn, investigated bone crystallinity alterations upon hydroxyapatite deproteinisation, and concluded this protocol remarkably alters bioapatite crystal size, leading to an increase of bone mineral crystallinity. However, Karampas and co-workers repeated the protocol proposed by Termine three times, which could have triggered a more marked effect on bone's inorganic matrix. According to Termine [116] and, Bertazzo and Bertran [118] organic constituents' removal by hydrazine is efficient if undergone only once, the noteworthy crystallinity changes found by Karampas being avoided by not repeating this procedure. In conclusion, Termine's protocol is prone to induce slight bone crystallinity alterations.

The most significant heat-induced alterations in bones' inorganic matrix occur from 600 to 800 °C, differences from one temperature to the next being quite small [24–26, 28, 45, 55]. Hence, any slight alteration caused by sample manipulation may influence interpretation of the results. Therefore, improved defatting and deproteinisation protocols are needed. For this reason, in this work enzymatic bone defatting (with lipase) and deproteinisation (with collagenase) procedures were assessed, based on the premise that enzymes are specific for a certain substrate. The experimental conditions of catalysis are quite similar to those verified *in vivo* and therefore, these protocols should not affect the inorganic bone.

The collagen fibril is composed of many tropocollagen molecules which in turn is a right-handed triple helix composed of two identical α -1 helices and one unique α -2 helix. These three helices have the same amino acid sequence basis: Gly – X – Y, X = proline in one third of the cases and Y = hydroxyproline [120, 121]. Concerning collagen degradation, type I collagenase was needed, since type I collagen is the predominant form in human bone. Zheng and co-workers [122] and Liu and Wang [123] subjected type I collagen from dentine to enzymatic degradation with clostridiopeptidase A, from bacterial origin (*Clostridium histolyticum*), that cleaves native collagen I at the -/-Gly bonds of the triple helical region.

As to the choice of lipase, it was based on Zhang's *et al.* work [124], that used lipase from fungus origin (*Aspergillus niger*) which catalyses hydrolysis of triacylglycerol into diacylglycerol and monoacylglycerol, and finally into glycerol and three free fatty acids.

1.6. Aims of the Study

This study aims to analyse burned and unburned human bones through vibrational spectroscopy techniques - Raman, FTIR-ATR, and INS – coupled to diffraction methods – X-ray (XRD) and neutron based. The main goal is the evaluation of heat-induced alterations in samples from a collection of non-identified modern skeletons burned under controlled conditions (400 to 1000 °C).

The present work is pioneer regarding the application of neutron diffraction methods to the study of burned human bones, and it intends to complement X-ray diffraction information on the same samples with a view to elucidate heat-induced diagenesis at the molecular level: namely the appearance of new inorganic phases within the bone, the detection of β -tricalcium phosphate (β -TCP) that is still unexplained [103], and changes in crystal structure parameters [117, 125]. This will hopefully lead to a better understanding of the heat-induced diagenesis in human skeletal remains when exposed to heat, and identify the major changes taking place at specific temperatures, which will have a major impact in both forensic and archaeological research.

2 Experimental

2. Experimental

2.1. Materials and Equipment

Table 2.1. List of reagents, equipment and software used along this work.

Reagents	
Acetone (95%)	Sigma-Aldrich, S.A., Sintra, Portugal
Calcium Chloride, CaCl ₂ .2H ₂ O	Sigma-Aldrich, S.A., Sintra, Portugal
Calcium (granular 99%)	Sigma-Aldrich, S.A., Sintra, Portugal
Collagenase from <i>Clostridium histolyticum</i>	Sigma-Aldrich, S.A., Sintra, Portugal
Ethanol (99.8%)	Sigma-Aldrich, S.A., Sintra, Portugal
Hydrazine	Sigma-Aldrich, S.A., Sintra, Portugal
Lipase from <i>Aspergillus niger</i>	Sigma-Aldrich, S.A., Sintra, Portugal
Na ₂ CO ₃	Sigma-Aldrich, S.A., Sintra, Portugal
Petroleum Ether	Sigma-Aldrich, S.A., Sintra, Portugal
Sodium Bicarbonate, NaHCO ₃ (≥ 99.7%)	Sigma-Aldrich, S.A., Sintra, Portugal
Sodium Hypochlorite (10-15%)	Sigma-Aldrich, S.A., Sintra, Portugal
TES (≥99% (titration))	Sigma-Aldrich, S.A., Sintra, Portugal
Equipment	
Analytical balance (Toledo AB54)	Mettler, Rotoquímica, Portugal
pH-meter (basic 20+)	Crison, Rotoquímica, Portugal
Rotary evaporator with vacuum	
Shaker “Vortex” (MS2 Minishaker)	IKA® Works, Frilabo, Portugal
Soxhlet extractor	
Water purification apparatus Milli-Q (Gen Pure)	TKA, Frilabo, Portugal
Commercial inverted microscope	Olympus IX71
D8 Advance X-ray powder diffractometer	Bruker, Portugal
General Materials Diffractometer (GEM) [126]	ISIS Facility, UK
Invia Reflex Raman Confocal Microscope	Renishaw
Jobin-Yvon T64000 Raman spectrometer coupled to an Olympus BH2 microscope	Horiba Jobin -Yvon, Bióptica, Portugal
Senterra II Compact Raman Microscope	Bruker, Spain

2. Experimental

TOSCA and MAPS indirect geometry time-of-flight neutron spectrometer [127, 128]	ISIS Facility, UK
Vertex 70 FTIR spectrometer, with a FT-Raman accessory kit (Ram II)	Bruker, Spain
Vertex 70 FTIR spectrometer, with Platinum ATR single reflection diamond accessory	Bruker, Portugal
Software	
aCLIMAX version 4.0.1 [129]	ISIS Facility, Rutherford Appleton Laboratory, UK
Diffac.Eva 4.2 version (AXS 2010/2016)	Bruker, Portugal
EXPGUI (graphical interface for GSAS) [130]	
General Structure Analysis System (GSAS) [131]	
LabSpec 5.0	Horiba, Villeneuve d'Ascq, France
MANTID version 3.4.0 [132]	
Opus 7.2	Bruker Optic, Germany
Origin 9.1	Origin Lab, USA

2.2. Sample Preparation

The bone samples were obtained from collection of non-identified human skeletons of the Laboratory of Forensic Anthropology of the University of Coimbra (Portugal).

The burning experiments were focused on the right humerus and femur of skeleton CC_NI_42 (*Cemitério dos Capuchos_Non Identified_Skeleton n° 42*). Prior to burning, the diaphysis of both bones was sectioned in seven pieces with an electric saw, and the mass, maximum length and diameter of each section were measured (Figure 2.1). Then the bone samples were burned under controlled conditions in an electric oven (model Barracha K-3 three-phased 14A): 400, 500, 600, 700, 800, 900 and 1000 °C, for 120 minutes, at a heating rate of 6 – 10 °C/min (Figure 2.2). After the burning process, the maximum length and diameter, and the mass of each sample were measured (Figure 2.2). Hence, values for the pre-burning and post-burning mass and dimensions were obtained for each bone section, in order to evaluate, heat induced size alterations as well as mass losses.

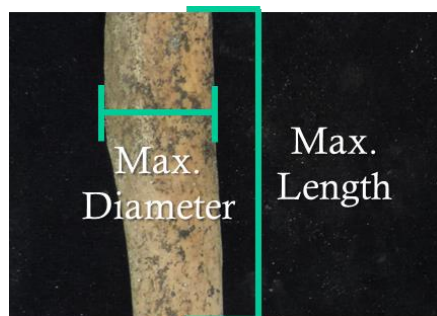


Figure 2.1. Representation of the measurement of maximum diameter and maximum length performed in bone sections prior and after the burning experiment.

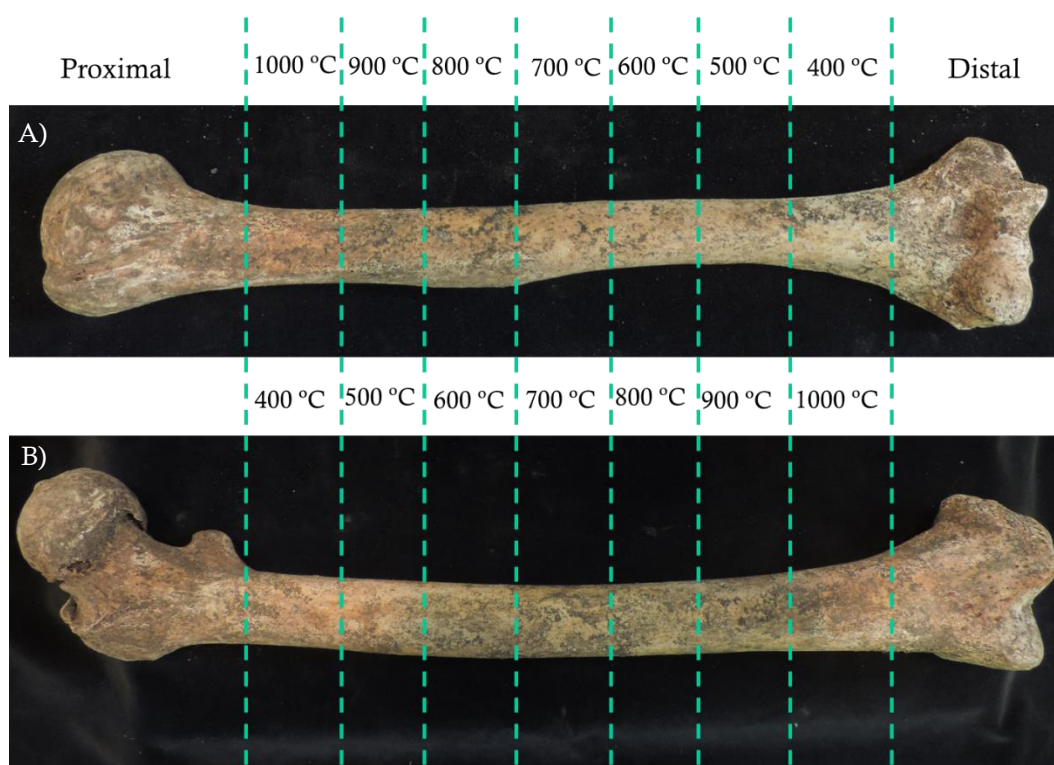


Figure 2.2. Representation of the cuts made humerus (A) and femur (B) diaphysis, from proximal to distal regions.

For each type of bone, two other sections were cut - one for the defatting and deproteinisation protocol and the other to be analysed as an intact sample.

All the samples were grinded and sifted (mesh size 400 μm), yielding a thin powder suitable for FTIR-ATR, Raman, XRD, neutron diffraction and INS analysis. Regarding the CARS experiments, 4 femur slices were prepared: unburned (intact), and burned at 400, 600 and 1000 $^{\circ}\text{C}$.

2. Experimental

2.2.1. Defatting and Deproteinisation Protocols

2.2.1.1. Petroleum Ether and Hydrazine Treatment

Chemical defatting and deproteinisation protocols were applied to a bone sample removed from skeleton CC_NI_18 in a previous study developed at the Molecular Physical-Chemistry R&D Unit, University of Coimbra (QFM), using petroleum ether and hydrazine according to reported procedures [56, 116]:

- 10 g of bone powder was soaked in petroleum ether and refluxed for approximately 10 h (in a Soxhlet extractor);
- The sample was exposed to hydrazine (120 cm³): i) at room temperature for 1 h, with constant stirring; ii) at 55 °C (with stirring), renewing hydrazine at 15 h and 24 h;
- The bone was washed: i) with ethanol 80% (100 mL), for 30 min; ii) with absolute ethanol (4x, 30 min each); iii) with acetone at 95% (3x, 30 min each);
- The sample was finally dried in a rotary evaporator under vacuum (at 60 °C); followed by a dry air flux (*ca.* 3 h).

2.2.1.2. Enzymatic Treatment

Defatting and deproteinization of bone samples was also performed through lipase and protease action. Both enzymatic digestions were undergone consecutively, starting with lipid degradation, in order to decrease sample losses and improve the efficiency of the proteolytic process. The left femur and humerus from skeleton CC_NI_42 were subject to the following treatment:

- 6.073 g of femur and 7.195 g of humerus (in separate experiments) were soaked in 200 mL Na₂CO₃/NaHCO₃ buffer solution (pH=9) containing 5% *w/v* lipase from *Aspergillus niger*, for 5 h at 40 °C, with constant stirring. The reaction mixture was then heated to 70 °C for 15 min under stirring, to inactivate the enzyme, after which the bone powder was washed with 500 mL of Na₂CO₃/NaHCO₃ buffer;
- The samples were then soaked in 200 mL of TESCA buffer (50 mM TES, 0.36 mM CaCl₂, pH=7.4), containing 0.01% *w/v* collagenase from *Clostridium histolyticum* and 4 g Ca²⁺ per mole of enzyme, for 5 h at 37 °C, with constant stirring. The enzyme was then inactivated by heating to 70 °C for 15 min;
- In order to remove non-collagenous proteins, bone powder was exposed to 100 mL of sodium hypochlorite solution at 6.25% *w/v* for 10 min, at room temperature;

- The bone powders were washed with *ca.* 2 L of TESCA buffer and filtered under vacuum;
- The samples were dried in a muffle at 110 °C, for 5 h, and then under a dry air flux for approximately 24 h.

2.3. Analytical Methodologies

2.3.1. Vibrational Spectroscopy

The FTIR spectra were recorded in a Bruker Optics Vertex 70 spectrometer, purged by CO₂-free dry air. The mid-infrared Attenuated Total Reflection spectra (FTIR-ATR, 400 - 4000 cm⁻¹) of the bone samples were recorded in pure powder on a Platinum ATR single reflection diamond accessory, with a KBr beamsplitter and a liquid nitrogen cooled wide band Mercury Cadmium Telluride (MCT) detector. The Far-InfraRed Attenuated Total Reflection spectra (FIR-ATR, 50 - 600 cm⁻¹) were also measured using pure powder on a Platinum ATR single reflection diamond accessory, using a silicon beamsplitter and a Deuterated L-alanine doped TriGlycine Sulphate (DLaTGS) detector with a polyethylene window. The spectra were corrected for the frequency dependence of the penetration deep of the electric field in ATR (considering the mean reflection index of sample 1.25), using the standard Opus software option.

In the far-IR region, FTIR-ATR spectra were the sum of 64 scans, at 2 cm⁻¹ resolution, in the mid-IR region FTIR-ATR spectra were the sum of 128 scans, at 2 cm⁻¹ resolution. The 3-term Blackman–Harris apodisation function was applied. Under these conditions, the accuracy in wavenumbers was well below 1 cm⁻¹.

Fluorescence has been known to be the major obstacle in burned bones analysis through Raman spectroscopy. Therefore, in this study different technical approaches were carried out in an attempt to overcome fluorescence interference: i) defatting and deproteinisation of the sample; ii) use of laser excitation sources with different wavelengths; iii) photobleaching; iv) CARS; and v) low temperature FT-Raman spectroscopy, acquired in several configurations and laboratories:

- At QFM-UC – in a Horiba Jobin-Yvon T64000 spectrometer in direct configuration mode (focal distance 0.640 m, aperture f/7.5), equipped with a holographic grating of 1800 grooves.mm⁻¹. The entrance slit was set to 200 µm. Rayleigh elastic scattering was rejected by a Notch filter, which reduces its intensity by a factor of 10⁶. The detection system was a liquid nitrogen cooled non-intensified 1024×256 pixels (1") CCD. The 514.5 nm line of an Ar⁺ laser (Coherent, model Innova 90C-04) was used as the excitation radiation, yielding *ca.* 10 mW at the sample position. All the spectra were recorded using an Olympus 50x

2. Experimental

objective (OlympuS 50XW, NA 1.0, wd 2 mm). A 200 μm confocal pinhole rejected signals from out-of-focus regions of the sample.

- At SCAI, University of Malaga – in a Raman microscope Invia Reflex Raman Confocal (Renishaw) spectrometer, equipped with a 785 nm HPNIR diode laser and a RemCam deep depletion CCD detection system, and coupled to a Leica, DMLM microscope with a NPLAN 50x objective. Data was recorded in the 100-3500 cm^{-1} range, at a 1 cm^{-1} resolution. 4 accumulations and an acquisition time of 10 s were used, with a laser power at the sample of 50 mW.
- At SCAI, University of Malaga – low temperature data was recorded in a 1 \times 1 camera of a Bruker Senterra Raman microscope, coupled to a CCD detector operating at -50 $^{\circ}\text{C}$. Data was collected by averaging spectra with different accumulation times (ranging from 10 s and 20 coadditions to 20 s and 10 coadditions) and powers at the sample (10 to 25 mW), with a resolution of 3 to 5 cm^{-1} , using three different excitation wavelengths (785, 633 and 532 nm). Variable temperature Raman measurements were performed, between 300 and 90 K, both with pure bone powder and in KBr pellets (to ensure a faster thermal equilibrium), using a liquid nitrogen cooled Linkam FTIR 600 stage (with a temperature stability of $<0.1^{\circ}\text{C}$).
- At SCAI, University of Malaga – using a FT-Raman accessory kit (RamII) of a Bruker Vertex 70 FT-IR spectrometer, equipped with a liquid nitrogen cooled germanium detector, with near-infrared excitation (in order to overcome fluorescence) provided by the 1064 nm line of a continuous-wave Nd:YAG laser (model CW from Klastech). The Raman scattering radiation was collected in a back-scattering configuration, with a 4 cm^{-1} spectral resolution. Averages of 1000 scans were used to obtain each spectrum, and powers ranging from 10 to 300 mW at the sample position were used in the measurements.
- At SCAI, University of Malaga – CARS images were collected using a commercial inverted microscope (Olympus IX71) with a 60x water objective and a PMT (Hamamatsu, with two filters SP 720 nm and one PF675/67 nm), to take the CARS signal of the phosphate at 697 nm (vibrational mode at 960 cm^{-1}). To obtain that signal, a pump laser at 746.7 nm (100 mW) was used, while the Stokes signal at 804.4 nm (80 mW) was generated by two picosecond Ti:Sapphire oscillators (Tsunmai, Spectra Physics) pumped by two continuous lasers at 532 nm (Millenia, Spectra Physics).

The INS experiments were performed in the indirect geometry time-of-flight, high resolution ($(\Delta E/E)$ ca. 1.25 %), broad range spectrometers MAPS [127] and TOSCA [128], at the ISIS Pulsed Neutron and Muon Source of the STFC Rutherford Appleton Laboratory, UK.

In MAPS, three incident energies were used – 650, 250 and 120 meV – to accurately observe the bands from hydroxyapatite's OH libration and stretching modes.

The samples (4 to 10 g) were wrapped in aluminium foil and fixed onto 4×4 cm thin walled aluminium cans. To reduce the impact of the Debye-Waller factor (the exponential term in equation (3)) on the observed spectral intensity, the samples were cooled to *ca.* 10 K. Data were recorded in the energy range 0 to 6000 cm⁻¹ and reduced into energy transfer spectra using the MANTID program (version 3.4.0) [132].

2.3.2. Diffraction Methods

X-ray powder diffraction measurements were carried out at the Coimbra Trace Analysis and Imaging Laboratory (TAIL, UC), in a Bruker D8 Advance X-ray powder diffractometer [133], coupled to a 1D LynxEye detector (Silicon Drift Detector), data being collected in the range 22 to 44°. The radiation used was Cu K α .

Neutron diffraction data was collected in the General Materials Diffractometer (GEM) at the ISIS Pulsed Neutron and Muon Source of the STFC Rutherford Appleton Laboratory, UK (see <http://www.isis.stfc.ac.uk/instruments/gem/>) in the scattering angle 1.1° to 169.3° range, for femur samples from the skeleton CC_NI_42, burned at 400, 700 and 1000 °C. Data was analysed by the Rietveld method, using the software GSAS-EXPGUI [130, 131].

Table 2.2 summarises which techniques were applied to each sample analysed in this study.

Table 2.2. Analytical approaches used in the analysis of femur and humerus samples exposed to heat and to the petroleum ether and hydrazine, and lipase and collagenase procedures.

Sample		Treatment	Analytical Approach
CC_NI_18	Femur	Intact	FTIR-ATR
		Petroleum ether + Hydrazine	MAPS TOSCA XRPD
		Lipase + Collagenase	
CC_NI_42	Femur	Intact	FTIR-ATR Raman 785 nm XRPD
		Lipase + Collagenase	FTIR-ATR Raman 514 nm

2. Experimental

CC_NI_42

Femur	400 °C	FTIR-ATR
		MAPS
	500 °C	TOSCA
		XRPD
	600 °C	Neutron Diffraction
		FTIR-ATR
	700 °C	MAPS
		TOSCA
	800 °C	XRPD
		Neutron Diffraction
900 °C	FTIR-ATR	
	Raman 514 nm	
1000 °C	Raman 785 nm	
	MAPS	
Intact	TOSCA	
	XRPD	
Lipase + Collagenase	FTIR-ATR	
	FTIR-ATR	
400 °C	MAPS	
	TOSCA	
500 °C	XRPD	
	FTIR-ATR	
500 °C	MAPS	
	TOSCA	
500 °C	XRPD	

CC_NI_42	Humerus	600 °C	FTIR-ATR MAPS TOSCA XRPD
		700°C	FTIR-ATR MAPS TOSCA XRPD
		800°C	FTIR-ATR Raman 514 nm Raman 785 nm MAPS TOSCA XRPD
		900 °C	FTIR-ATR Raman 514 nm Raman 785 nm MAPS TOSCA XRPD
		1000 °C	FTIR-ATR Raman 514 nm Raman 785 nm MAPS TOSCA XRPD

2.4. Quantitative Analysis of Bone Heat-Induced Alterations

In order to better visualise the spectral alterations of bone samples caused by heat exposure, several mathematical relationships were applied, which are summarized in Table 2.2.

INS and neutron diffraction quantitative analysis was based on peaks' intensity since the intensity of the signal is directly proportional to the number of scattering atoms/planes.

2. Experimental

Table 2.3. Quantitative relationships used for assessing heat-induced alterations in bone, based on FTIR, Raman and XRD data.

Method	Parameter	Spectral relationship	Reference		
FTIR	CI	Cristallinity Index	$\frac{Abs(602\text{ cm}^{-1}) + Abs(562\text{ cm}^{-1})}{Abs(590\text{ cm}^{-1})}$	[134]	
	C/P	Carbonate to Phosphate	I	$\frac{Abs(1415\text{ cm}^{-1})}{Abs(1035\text{ cm}^{-1})}$	[28, 45, 99]
			II	(API+BPI)/603	This study
	API	Type A carbonate	$\frac{Abs(1540\text{ cm}^{-1})}{Abs(603\text{ cm}^{-1})}$	[25, 96]	
	BPI	Type B carbonate	$\frac{Abs(1415\text{ cm}^{-1})}{Abs(603\text{ cm}^{-1})}$	[25, 96]	
	C/C	Carbonate (A+B) to carbonate B	$\frac{Abs(1450\text{ cm}^{-1})}{Abs(1415\text{ cm}^{-1})}$	[25]	
	OH/P	Amount of OH ⁻ groups	I	$\frac{Abs(630\text{ cm}^{-1})}{Abs(603\text{ cm}^{-1})}$	[25]
			II	$\frac{Abs(3572\text{ cm}^{-1})}{Abs(603\text{ cm}^{-1})}$	This study
			III	$\frac{Abs(340\text{ cm}^{-1})}{Abs(603\text{ cm}^{-1})}$	This study
	Raman	Mineral to matrix		$A(\nu_2(\text{PO}_4^{3-})) / A(\text{amide III})$	[54]
Mineral maturity/Crystallinity		$1 / \text{FWHM}(\nu_1(\text{PO}_4^{3-}))$	[54, 93]		
C/P		I	$A(\nu_1(\text{CO}_3^{2-})) / A(\nu_1(\text{PO}_4^{3-}))$	[93]	
		II	$A(\nu_1(\text{CO}_3^{2-})) / A(\nu_2(\text{PO}_4^{3-}))$	[135]	
OH/P		$A(\nu(\text{OH}^-)) / A(\nu_2(\text{PO}_4^{3-}))$	This study		
XRD	CI	Crystallinity index	$\frac{H(202)+H(300)+H(112)}{H(211)}$ $= (a + b + c) / h$	[38]	
	L	Crystal dimension	$L = \frac{K\lambda}{\beta \cos\theta}$ $\frac{\beta = \text{FWHM}(002)}{\beta = \text{FWHM}(310)}$	[136]	

*Absorbance intensity *Abs*, peak area *A*, peak height *H*, length *L*, full width at half maximum *FWHM*

The crystallinity index calculation by X-ray diffraction is achieved through the equation in Table 2.2, as demonstrated in Figure 2.3.

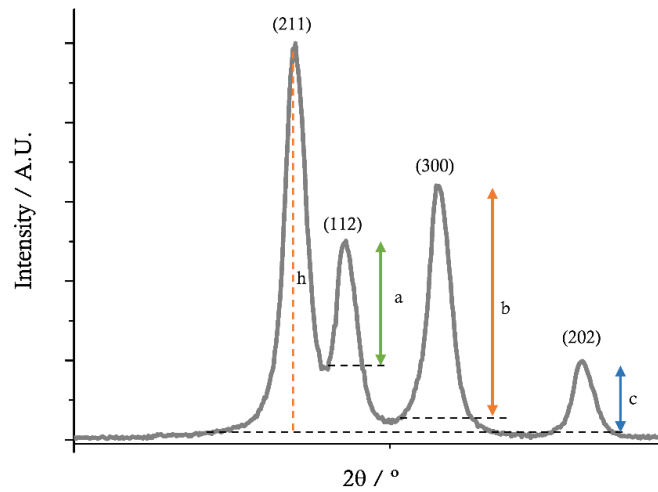


Figure 2.3. Schematic representation of the calculation of crystallinity index through XRD

The CI value is then related with the Scherrer equation ($L = \frac{K\lambda}{\beta \cos\theta}$), applied to the diffracting planes (002) and (310), with $K=0.89$ (chosen based on Wang and co-workers study [32]), $\lambda=1.54$ Å (being the wavelength of the X-ray beam) and θ is the value of the angle at the peak arises (in radians), which in this case assumes the values 0.45 rad for the (002) peak and 0.69 rad for the (310) peak.

3 Results and Discussion

3. Results

3.1. Defatting and Deproteinisation

As discussed along the Chapter 1, when the interest of the study is the inorganic component of the bone, organic constituents' removal is a necessary procedure to the analysis of the unburned bones since organic constituents' vibrational spectra overlap the inorganic components' signals, particularly in the range 1180 - 3850 cm^{-1} . Thus, the chemical alterations within bone's inorganic structure caused by hydrazine and the enzymatic protocols were evaluated first. Intact sample and petroleum ether and hydrazine, and lipase and collagenase-treated samples were analysed through FTIR-ATR and INS spectroscopies and XRPD. The results are described next.

FTIR-ATR analysis (Figure 3.1) revealed that both procedures were efficient in removing organic components. The hydrazine-treated sample spectrum only presented the bands corresponding to the inorganic matrix. Relative to the enzymatically-treated sample, although less intense, a band at 1647 cm^{-1} was present, assigned to amide I (stretching vibration mode of the carbonyl groups (C=O)) and to water deformation, evidencing that probably the collagenase digestion was not complete. Alternatively, since the amide II band (C-N stretching mode from the peptide bond) was absent, the 1647 cm^{-1} signal might be due to non-collagenous proteins within the bone. Regarding the lipase effect, the results appear to indicate that the enzymatic digestion was efficient as no bands assigned to lipids (1460 cm^{-1} and 2960 - 2850 cm^{-1}) were detected after enzymatic treatment.

A close-up of the spectra in the 450 - 1250 cm^{-1} range (Figure 3.2) disclosed the most considerable changes undergone by bone samples upon defatting and deproteinisation, mainly observable in hydrazine-treated sample. It was notable the sharpening of the band assigned to $\nu_3(\text{PO}_4^{3-})$ and also its slight red shift from 1025 to 1018 cm^{-1} . The enzyme-treated sample, in turn, presented a blue shift of this same band (to 1029 cm^{-1}). The $\nu_1, \nu_3(\text{PO}_4^{3-})$ domain has been reported to contain information about apatite stoichiometry. A peak at *ca.* 1020 cm^{-1} is indicative of non-stoichiometric apatites (containing HPO_4^{2-} and/or CO_3^{2-}), while a peak at 1030 cm^{-1} suggests stoichiometric apatites ($\text{Ca}_{10}(\text{PO}_4)_6(\text{OH})_2$) [137, 138]. Apparently, the hydrazine exposure produced a less stoichiometric bioapatite, while the enzymatic treatment yielded a more stoichiometric one.

The $\nu_1(\text{PO}_4^{3-})$ band, at 960 cm^{-1} , was considerably more evident in the treated samples. The band at 560 cm^{-1} , $\nu_4(\text{PO}_4^{3-})$, was much more intense for the hydrazine-treated sample than for the intact and enzymatically-treated samples. Comparing the spectra of intact and enzymatic-treated bones, in the 450 - 1250 cm^{-1} interval (Figure 3.2) the alterations were not so evident, besides the slight shift of the $\nu_3(\text{PO}_4^{3-})$ band to 1029 cm^{-1} , the $\nu_1(\text{PO}_4^{3-})$ band, at 960 cm^{-1} , was a little more clearly detected.

3. Results and Discussion

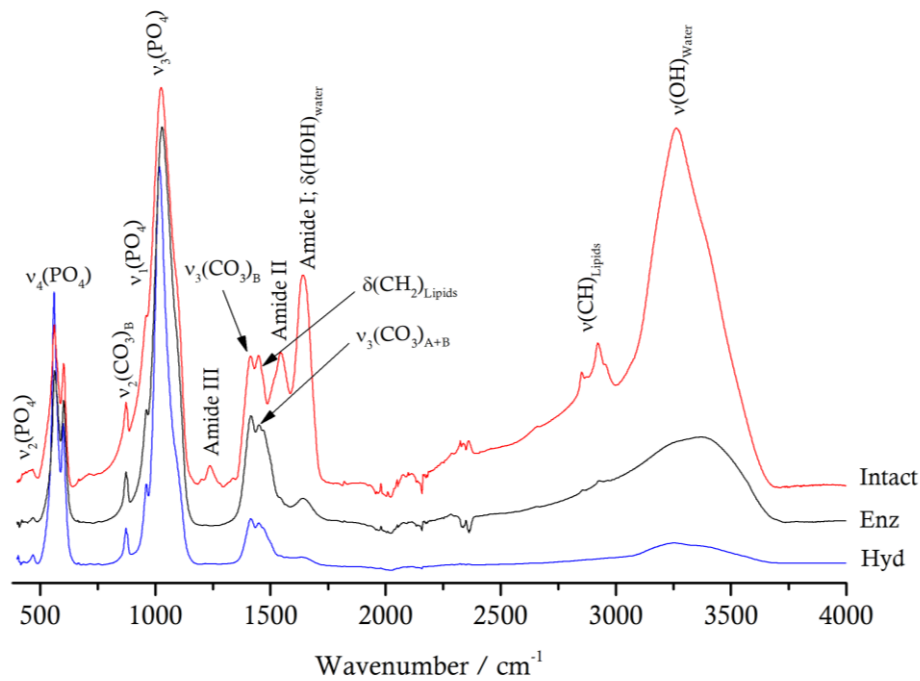


Figure 3.1. ATR spectra, in the mid-infrared region, for femur samples from skeleton CC_NI_18: intact (red); enzymatically-treated (Enz, black) and hydrazine-treated (Hyd, blue).

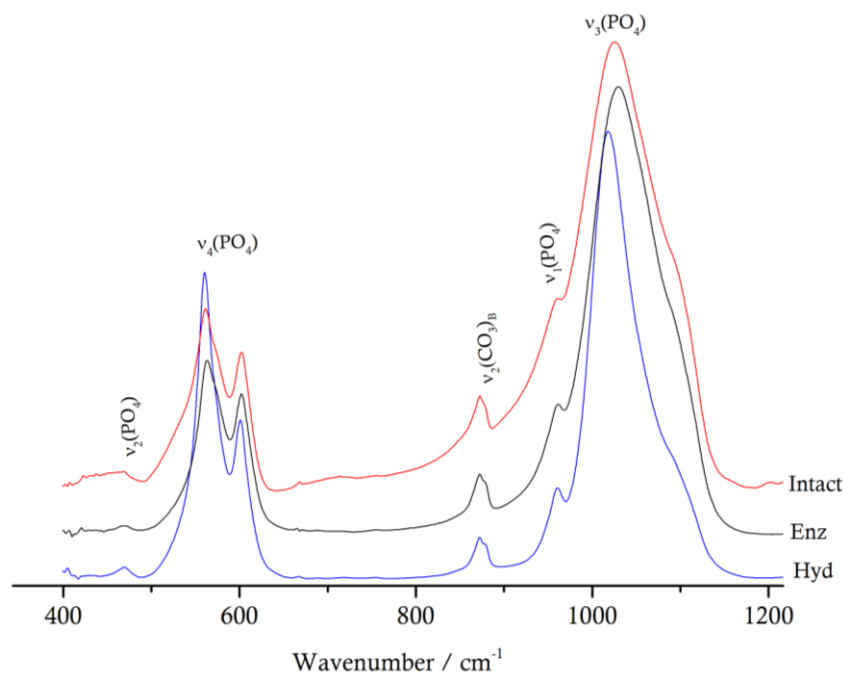


Figure 3.2. ATR spectra, in the range 420 – 1280 cm^{-1} , for femur samples from skeleton CC_NI_18: intact (red); enzymatically-treated (Enz, black) and hydrazine-treated (Hyd, blue).

Aiming at a more detailed assessment of chemical alterations, the mathematical relationships summarised in Table 2.2 were applied, which results are resumed in Table 3.1.

Table 3.1. CI, C/P, API, BPI, (API+BPI)/605 and C/C parameters obtained from the FTIR-ATR data collected for intact, hydrazine and enzymatically-treated samples of femur from skeleton CC_NI_18.

Parameter	Intact	Hydrazine Treated	Enzymatically Treated
CI	3.480	4.503	3.352
C/P-I	0.322	0.112	0.272
C/P-II	7.071	1.068	3.562
API	1.091	0.058	0.229
BPI	1.060	0.318	0.877
C/C	1.006	0.918	0.927

Analysing Table 3.1 and comparing the ratio values obtained for intact, hydrazine and enzymatically-treated samples, alterations in the crystallinity index of hydrazine exposed bone were obvious, from 3.480 to 4.503. The CI value for the enzymatically-treated bone varied from 3.480 to 3.352, which was considerably less than for the hydrazine treated sample and in opposite ways (CI decreased after the enzymatic treatment). The C/P-I ratio, in turn, decreased upon exposure to both deproteinisation and defatting procedures, although this alteration was higher for the hydrazine-treated sample (0.332 to 0.112) relative to the enzymatically-treated one (0.322 to 0.272). The C/P-II (representing the (API+BPI)/605 index) was thought to eliminate the interference of the $\delta(\text{CH}_2)_{\text{collagen+lipids}}$ band, therefore representing the total amount of carbonates (A+B) to phosphates. This index appeared highly affected by both treatments, *ca.* 86% by hydrazine washing and 50% by enzymatic treatment, and did not reflect the changes estimated with the C/C ratio because of an higher error introduced by API, which is considerably affected by the interference of amide II band that is eliminated through deproteinisation. Regarding the API values, it is clear that samples were extensively altered as a consequence of defatting/deproteinisation. However, the API values do not lead to a clear interpretation, since the 1540 cm^{-1} band, assigned to $\nu_3(\text{CO}_3^{2-})_{\text{A}}$, superimposes with the amide II band. As the organic constituents were removed from the bone samples (either through hydrazine or enzymatic treatment), the intensity of this band decreased leading to a consequent decrease of the API ratio. This effect was higher for the hydrazine-treated sample, resulting in lower API values comparing with the enzymatic treated one. Similarly, the BPI ratio diminished considerably upon hydrazine exposure, from 1.060 to 0.318. For the enzymatically-treated bone, this value underwent a less marked decrease (to 0.877). Hydrazine, in particular, affected this ratio substantially. As to the C/C ratio, it appeared slightly influenced by both protocols, but not to the same extent, the difference being probably due to the removal of lipids and consequent elimination of the partial overlapping of the 1450 and 1460 cm^{-1} bands, respectively assigned to $\nu_3(\text{CO}_3^{2-})_{\text{A+B}}$, and

3. Results and Discussion

$\delta(\text{CH}_2)_{\text{collagen+lipids}}$. Considering the results obtained for the BPI ratio, previously discussed, this decrease in C/C may also reveal a decrease in type B carbonates, that was higher in the hydrazine-treated sample. Additionally, the CI decrease observed for the enzymatic-treated sample does not make sense since it would be expected to increase with a decrease of the carbonates' amount.

Termine *et al.* [116] had already described some of these compositional changes upon hydrazine exposure, namely the CO_3^{2-} and HPO_4^{2-} slight but significant decrease. Based on this analysis, the effect of hydrazine on bioapatite's stoichiometry is difficult to interpret, since a decrease in the carbonate and hydrogen phosphate content should lead to an increase in stoichiometry and consequently, to a shift of the $\nu_3(\text{PO}_4^{3-})$ band to *ca.* 1030 cm^{-1} . A possible explanation may be the increase in vacancies within the crystal lattice caused by loss of carbonate and hydrogen phosphates, suggested to be due to carbonate and phosphate solubilisation in saturated hydrazine medium [119].

INS spectroscopic data, recorded on MAPS (Figure 3.3), left no doubts relative to the efficiency of both defatting/deproteinisation protocols currently used: contrary to what was anticipated based on infrared results, enzymatic treatment had a very limited success in removing bone's lipidic constituents (Figure 3.3, black).

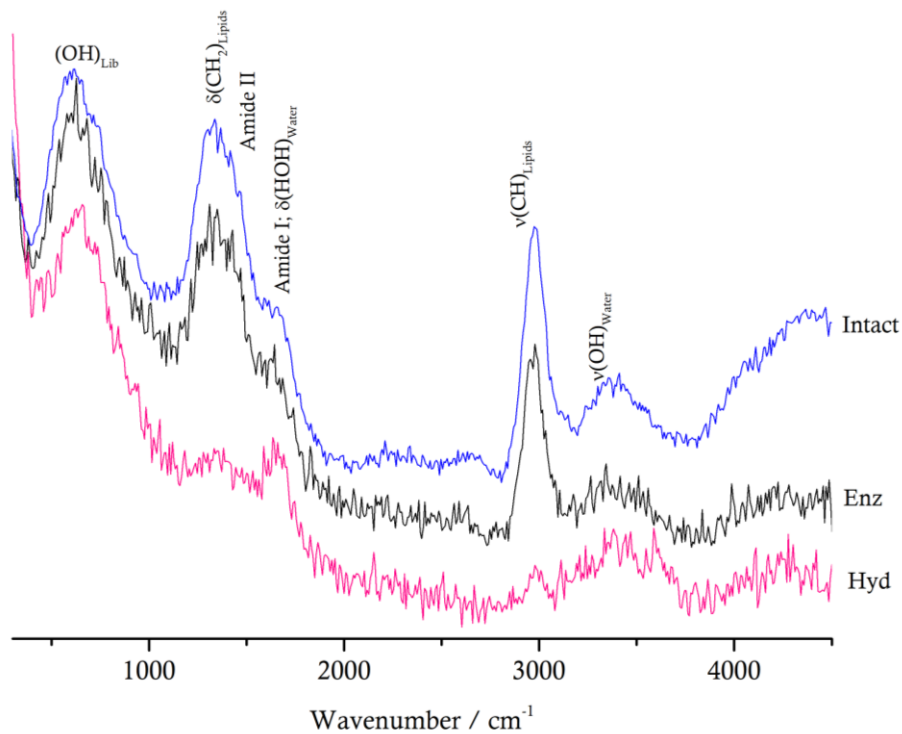


Figure 3.3. Inelastic neutron scattering spectra (obtained on MAPS) for femur samples from the skeleton CC_NI_18: intact (blue); enzymatically-treated (Enz, black), hydrazine-treated (Hyd, pink).

The bands assigned to lipids and proteins at 1460, 1650 and 2980 cm^{-1} were very intense when compared to the hydrazine-treated sample (Figure 3.4, pink), but less intense than those from the intact sample (Figure 3.4, blue), evidencing that the enzymatic digestion protocol requires optimisation. Although the petroleum ether defatting protocol was efficient, hydrazine-deproteinisation was incomplete, some proteins still present in the analysed sample (amide I band at *ca.* 1665 cm^{-1}).

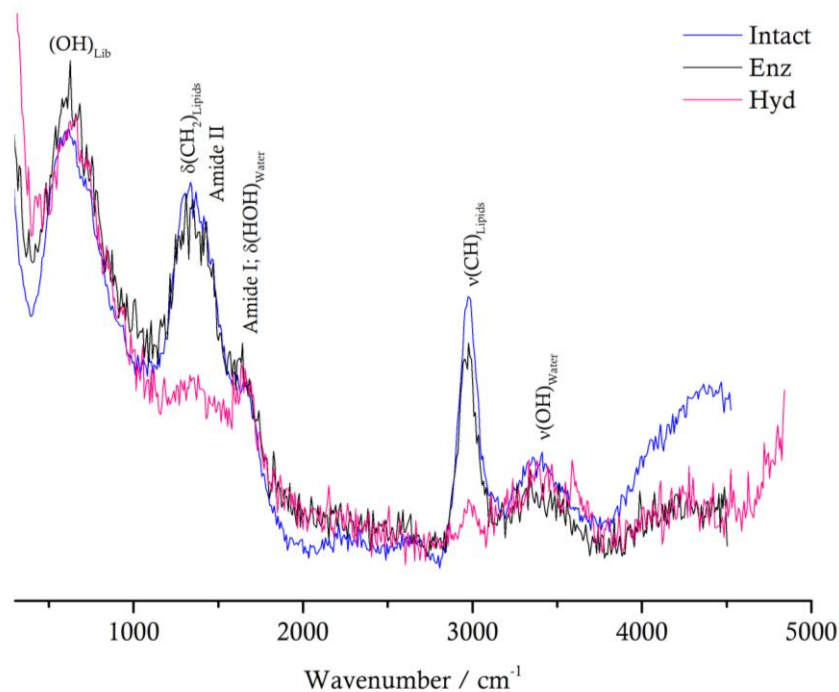


Figure 3.4. Inelastic neutron scattering spectra (obtained on MAPS) for femur samples from the skeleton CC_NI_18: intact (blue); enzymatically-treated (Enz, black), hydrazine-treated (Hyd, pink).

The results acquired in the TOSCA spectrometer, that has a much higher sensitivity than MAPS in the 0 – 2000 cm^{-1} range, allowed to conclude that hydrazine caused considerable changes within the crystal lattice, reflected in an intensity decrease of the bands at 68 - 120 cm^{-1} and 240 cm^{-1} (Figure 3.5, pink).

Regarding the crystalline lattice, however, it is not clear whether it was affected by enzymatic treatment – the superimposition of the spectra (Figure 3.6) showed the enzymatic treated sample spectrum only slightly more intense than the intact sample spectrum.

The $\nu_1(\text{CO}_3^{2-})$ band intensity, at 1056 cm^{-1} , also decreased in intensity upon both treatments (mainly for hydrazine exposure), indicating alterations in the CO_3^{2-} amount. This is in agreement with FTIR-ATR data (previously discussed).

Analysing TOSCA spectrum of the enzyme treated sample (Figure 3.5 and 3.6, black), the decrease in the intensity of the band assigned to amide II (stretching mode of the (C-N) peptide

3. Results and Discussion

bond), at 1560 cm^{-1} , indicates that collagenase was efficient in cleaving the collagen molecule (the main protein component in bone), the remaining protein degradation products and possibly non-collagenous proteins being proposed as the source of the detected amide I and III bands, at 1650 and 1300 cm^{-1} , respectively.

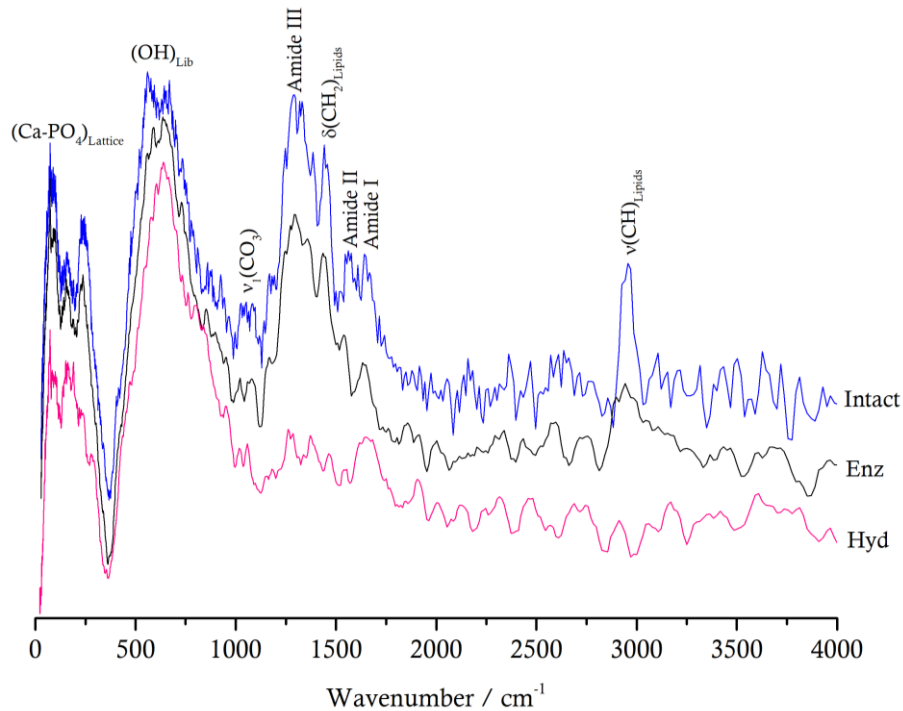


Figure 3.5. Inelastic neutron scattering spectra (obtained on TOSCA) for femur samples from the skeleton CC_NI_18: intact (blue); enzymatically-treated (Enz, black), hydrazine-treated (Hyd, pink).

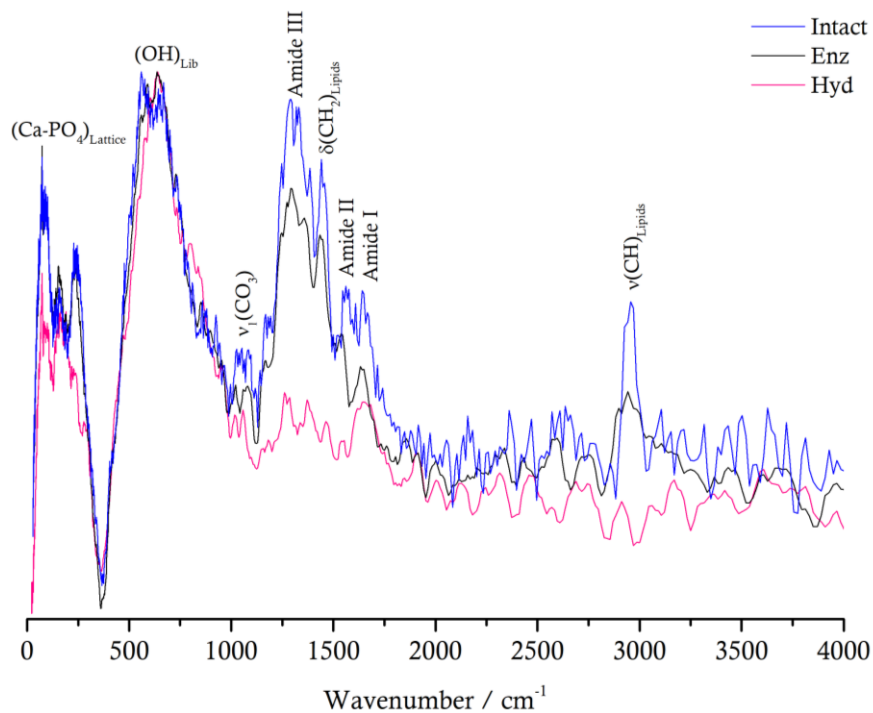


Figure 3.6. Inelastic neutron scattering spectra (obtained on TOSCA) for femur samples from the skeleton CC_NI_18: intact (blue); enzymatically-treated (Enz, black), hydrazine-treated (Hyd, pink).

Regarding the action of lipase on bone samples, there is no doubt that the digestion process was not successful. The most reasonable explanation for this fact is that bone contains many different types of lipids apart from the tri-, di- and mono-acylglycerols that are recognised by the lipase of *Aspergillus niger* that was used in this work. Actually, the soaking processes in $\text{NaHCO}_3/\text{Na}_2\text{CO}_3$ buffer specifically at pH 9 was wilful used in order to facilitate other lipids removal by saponification [124]. This was not enough to eliminate the remaining lipids not recognised by the enzyme. Another possible explanation is that the optimal pH for *Aspergillus niger* lipase is between 3 and 6.5, while the experiment was carried out at pH 9. With this in mind, higher quantities of enzyme were used to counterbalance the alkaline medium thus, the most likely reason for lipase inefficiency is probably being its inability to recognise all the lipids contained in bone tissue.

Hence, the catalysis procedure must be optimised in future studies, namely by using a mixture of different lipases and by better adjusting pH. In addition, since petroleum ether removed all the lipids content in the bone, as clearly depicted in Figures 3.5 and 3.6, one other alternative to the sole use of *Aspergillus niger* lipase may be to perform the petroleum ether washing, although it takes several hours. Also, this procedure did not show any negative effects on the bone's mineral lattice. Regarding protein removal, hydrazine washing, similarly to collagenase treatment, still leaves traces of protein in the bone.

XRPD analysis revealed clear differences between intact and treated bone (both with hydrazine and enzyme). The main alterations that stood out from the diffractograms in Figure 3.7 were the sharpening of the diffraction peaks (002), (112), (300) and (202) and the increased intensity of the (002) peak, especially for the hydrazine-treated sample, evidencing an increase in the sample's crystallinity. Table 3.2 comprises the calculated CI ratio and crystals' thickness and length for the untreated and treated (hydrazine and enzyme) bone samples. Interestingly, hydrazine was found to strongly affect crystal's length (*c*-axis, from 4.436 to 5.682), while its effect in crystals' thickness was inexistent.

Surprisingly enough, enzymatic treatment caused an increase in these three parameters, the effect on thickness and length being of the same magnitude but much less considerable than for the hydrazine treatment.

Summarising all the information obtained, hydrazine increased the crystallinity index concomitantly with a decrease in carbonates, although its efficiency removing the organic constituents was remarkable. On the other and, enzymatic defatting and deproteinisation showed to be much less effective, an improvement of the experimental protocol being required. The enzymatic procedure, applied in this study for the first time, was also seen to cause alterations within the bone's inorganic matrix, which were probably caused by exposure to sodium hypochlorite (NaClO) and not necessarily due to the enzymatic digestion itself. Although the treatment with NaClO only lasted for 10 min (at room temperature) and the concentration of the solution was quite low (6.25% *w/v*), this possibility cannot be discarded [113]. In fact, the two

3. Results and Discussion

enzymes used, specific for particular lipids and type I collagen, do not interact with the inorganic constituents of bone.

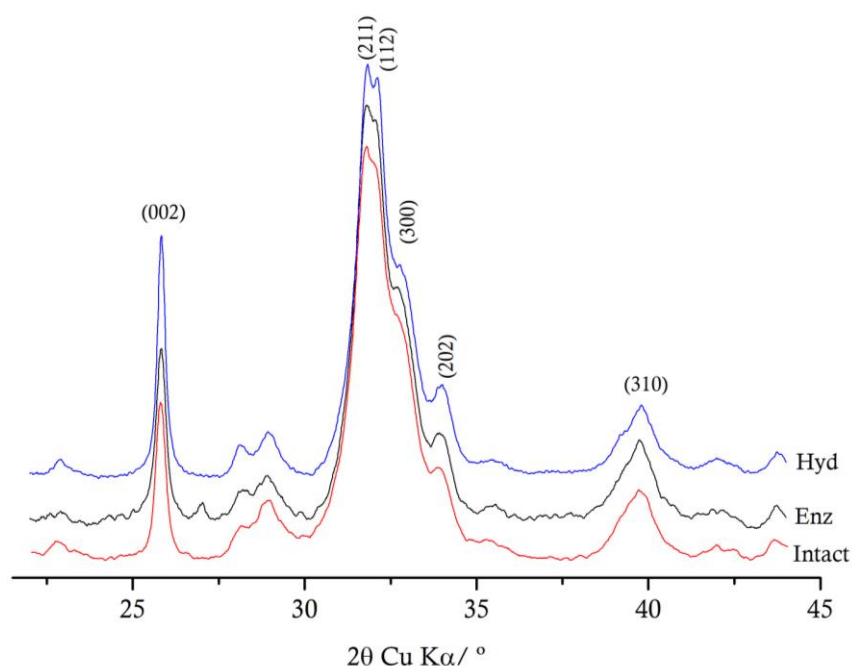


Figure 3.7. X-Ray diffractograms obtained in the range 22 - 43°, using Cu K α radiation for femur samples from the skeleton CC_NI_18: intact bone sample (red); enzymatically-treated sample (Enz, black), hydrazine-treated sample (Hyd, blue).

Table 3.2. CI and crystals' thickness and length (Å), obtained from the X-ray diffraction data for the intact, hydrazine and enzymatically-treated samples of femur from the skeleton CC_NI_18.

Parameter	Intact	Hydrazine Treated	Enzymatically Treated
CI	0.026	0.075	0.060
Thickness (Å)	1.576	1.575	1.764
Length (Å)	4.436	5.682	4.637

Although the enzymatic treatment caused slight changes within bioapatite, comparing with petroleum ether and hydrazine exposure, these were significantly less marked. The enzymatic procedure takes only a few hours, it is not necessary to renew the solutions (considerably decreasing the quantity of reagents needed), no complex experimental setups are needed and the experiment is not expensive. Attending to these advantages, optimisation of the enzymatic protocol is perfectly justifiable and carries enormous potential.

3.2. Heat-induced Macroscopic Alterations

Figure 3.8 is an assembly of the visual alterations undergone by bones, in general – also observed in the samples used in this work - from low to high burning temperatures, based on photographic records of studies accomplished at the Laboratory of Forensic Anthropology of the University of Coimbra.

As observed by Shahack-Gross *et al.*, Shipman *et al.* and others [27, 46, 47], at 400 °C bones had a dark grey colouration, what indicates charring. Above 500 °C bones had lighter colours, indicating calcination. Also shape and dimensions were seriously affected, particularly at high burning temperatures (>700 °C). These macroscopic alterations, at shape and dimensions' level, caused by the heating process in the bone sections under study were evaluated through mass, maximum length and diameter measurement. The percentage of alteration undergone by each sample upon controlled burning are resumed in Table 3.3.

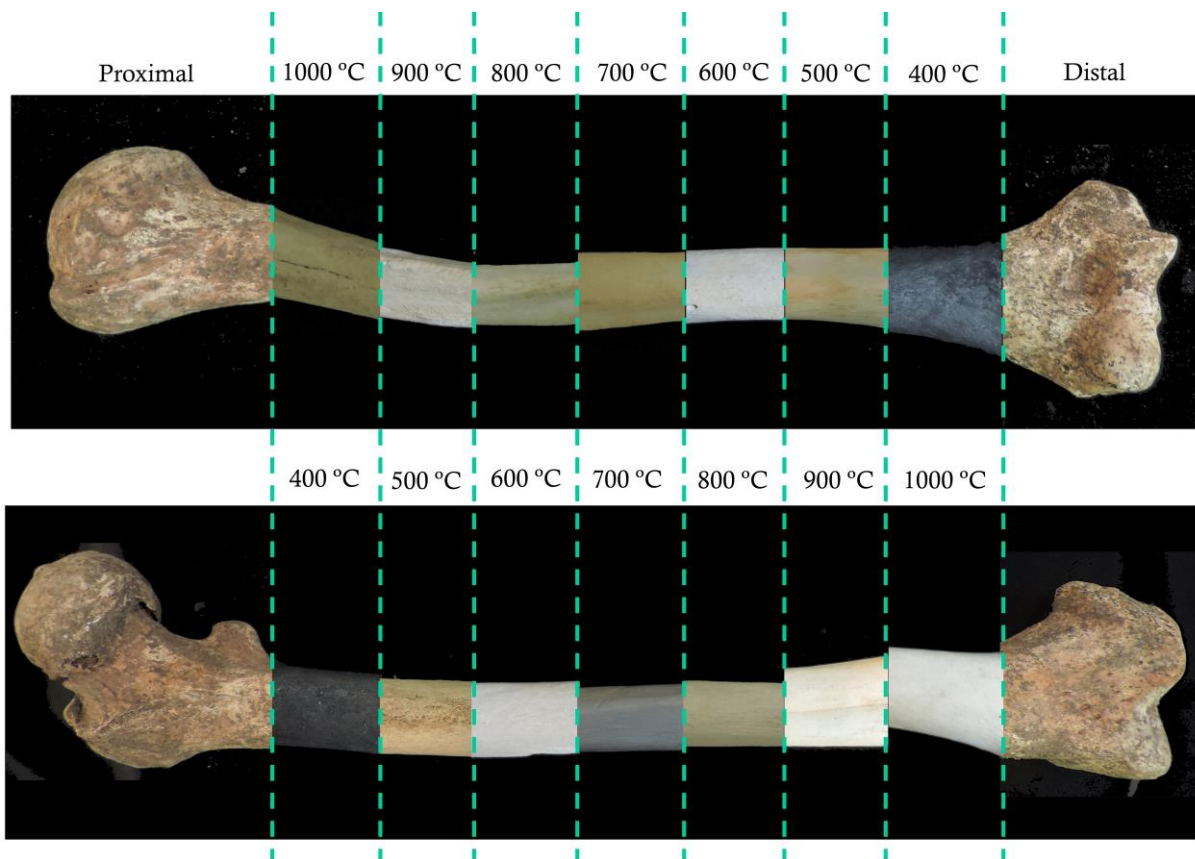


Figure 3.8. Photographic assembly of the heat induced colour alterations caused by the exposure from 400 to 1000 °C, based on the records of studies from the Laboratory of Forensic Anthropology of the University of Coimbra, verified in the samples of this work.

Table 3.3. Pre- and post-burning values of mass (g), maximum length and maximum diameter (mm) of femur and humerus slices burned at different temperatures (°C), for 120 min. The respective percentage of these features after the burning experiment are also presented (heat induced macroscopic alterations, HIMA).

Bone	Pre-Burning Measurements			Post-Burning Measurements			HIMA (%)			
	Mass	Max. Length	Max. Diameter	Temperature	Mass	Max. Length	Max. Diameter	Mass	Length	Diameter
Femur	14.960	32.020	35.800	400	11.590	31.280	31.800	-22.527	-2.311	-11.173
	16.300	39.000	28.350	500	11.440	38.800	27.530	-29.816	-0.513	-2.892
	9.640	39.620	25.610	600	6.330	38.960	25.310	-34.336	-1.666	-1.171
	12.630	42.760	26.530	700	8.130	42.180	25.080	-35.629	-1.356	-5.466
	11.330	31.080	26.800	800	7.130	30.440	23.460	-37.070	-2.059	-12.463
	13.640	38.520	27.170	900	8.460	33.960	16.660	-37.977	-11.838	-38.682
	12.780	37.640	30.610	1000	7.890	32.950	26.420	-38.263	-12.460	-13.688
Humerus	7.820	34.620	23.720	400	6,200	35.550	22.740	-20.716	2.686	-4.132
	6.090	24.750	20.500	500	4.330	25.350	19.540	-28.900	2.424	-4.683
	6.680	26.950	20.710	600	4.350	26.470	19.620	-34.880	-1.781	-5.263
	8.000	30.460	21.080	700	5.060	30.010	20.250	-36.750	-1.477	-3.937
	7.600	28.180	20.070	800	4.760	27.560	19.470	-37.368	-2.200	-2.990
	7.900	29.180	19.700	900	4.890	28.400	17.610	-38.101	-2.673	-10.609
	9.570	32.340	25.780	1000	5.910	30.470	21.420	-38.245	-5.782	-16.912

It was found that femur and humerus had completely different behaviours when exposed to heat (Figures 3.9 and 3.10), femur assuming highly fluctuating values as temperature rose. The biggest mass losses (Figure 3.9 and 3.10, dark blue curve) occurred upon exposure up to 600 °C, for both bones. The exposure to temperatures beyond 400 °C resulted in *ca.* 80% of the initial mass for femur and humerus, occurring its decrease from 400 to 600 °C (*ca.* 65% of the initial mass was kept). From 600 to 1000 °C in both bones, mass slightly decreased reaching its lowest value of *ca.* 60%.

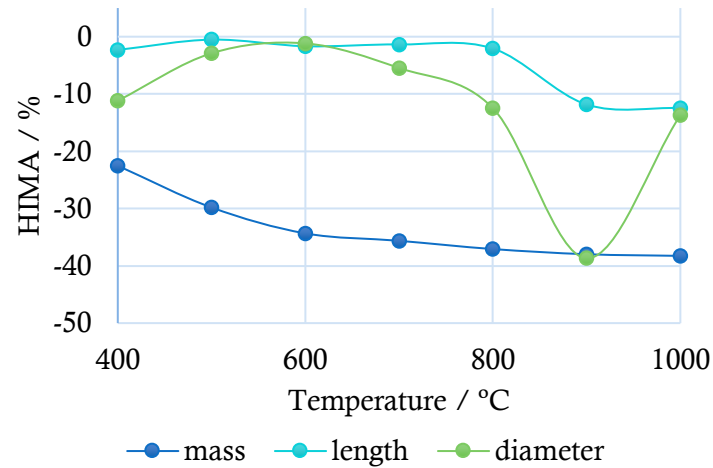


Figure 3.9. Graphic representation of the heat-induced macroscopic alterations (HIMA) in mass (dark blue), maximum length (light blue) and diameter (green), as a function of temperature, for femur slices from skeleton CC_NI_42.

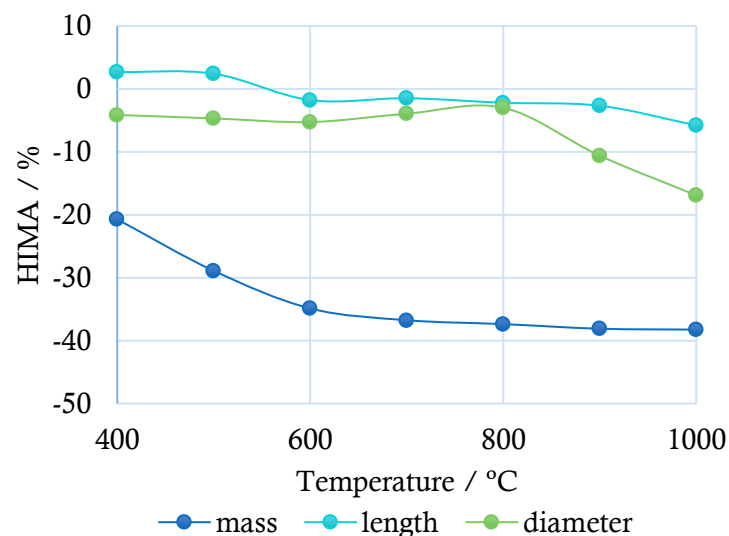


Figure 3.10. Graphic representation of the heat-induced macroscopic alterations (HIMA) in mass (dark blue), maximum length (light blue) and diameter (green), as a function of temperature, for humerus slices from skeleton CC_NI_42.

3. Results and Discussion

Regarding the variation in maximum length, for femur (Figure 3.9, light blue curve), it was not superior to 2% except from 800 to 900 °C (up to 12%). Interestingly, for humerus (Figure 3.10, light blue curve), exposure to 400 and 500°C caused a longitudinal (max. length) expansion (more than 2%), slightly decreasing for higher temperatures.

Diameter changes (Figure 3.9, light green curve), were very fluctuating for femur samples. Exposure to 400 °C caused the transversal shrinking (max. diameter) of the bone section by 11%, its expansion occurring above 400 °C, starting to decrease above 600 °C. At 900 °C maximum diameter reached its lowest value of *ca.* 60% of its initial dimension, increasing abruptly once more (to 86%) at 1000 °C. For the humerus, the maximum diameter remained relatively constant up to 800 °C (Figure 3.10, light green curve), while it decreased gradually from 800 to 1000 °C (97% to 83% of the initial dimension).

As proved by the previous analysis of the macroscopic variations of bones' features with temperature, different bones from the same individual had distinct behaviours when exposed to heat. *In vivo*, bone is a live tissue and the composition along the same bone varies as a consequence of the constant bone resorption/regeneration metabolic processes [29, 30, 33, 139-141], suggesting that the dissimilar macroscopic response of different bones to the heating process is related to the submicroscopic compositional and structural variations between them. Therefore, it is expected that the analysis through spectroscopic and diffraction techniques (described in the next section) is able to reveal the source of these differences in order to relate them with the measured macroscopic changes.

3.3. Heat-induced Sub-microscopic Alterations

3.3.1. Fourier Transform Infrared Spectroscopy

FTIR-ATR data was collected in the far-IR and mid-IR regions for intact, enzymatically defatted and deproteinised, and burned femur and humerus samples. The results are presented in Figures 3.11 (A) and (B), respectively.

By analysing Figure 3.11, it is possible to conclude that both bones contained fluorapatite, reflected by the presence of a shoulder in the $\nu_3(\text{PO}_4^{3-})$ band, at 1090 cm^{-1} . As the temperature increased up to 600 °C organic material was destroyed, the biggest losses being observed from the intact samples to the samples burned at 400 °C, which is in agreement with the mass losses related with the macroscopic changes caused by heating. The bands assigned to the organic component completely disappeared from the spectra above 700 °C, concomitantly, the bands assigned to lattice vibrational modes, in the range 0 - 420 cm^{-1} (far-IR region), got sharper and more defined indicating more ordered crystalline lattices (Figure 3.12).

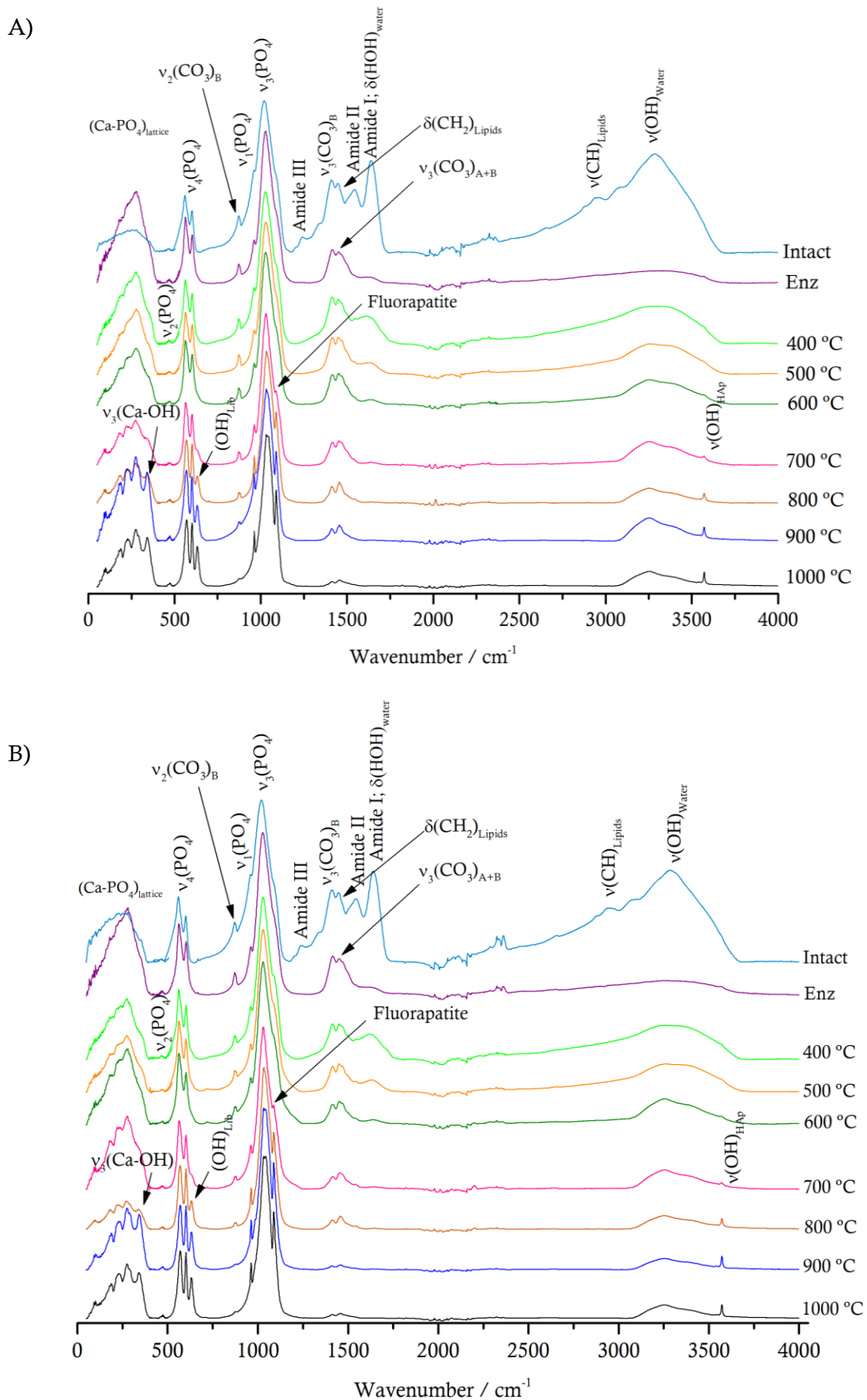


Figure 3.11. ATR spectra, in the far and mid-IR regions for: (A) femur samples and (B) humerus samples of the skeleton CC_NI_42: intact, enzymatically-treated (Enz) and burned from 400 to 1000 °C.

3. Results and Discussion

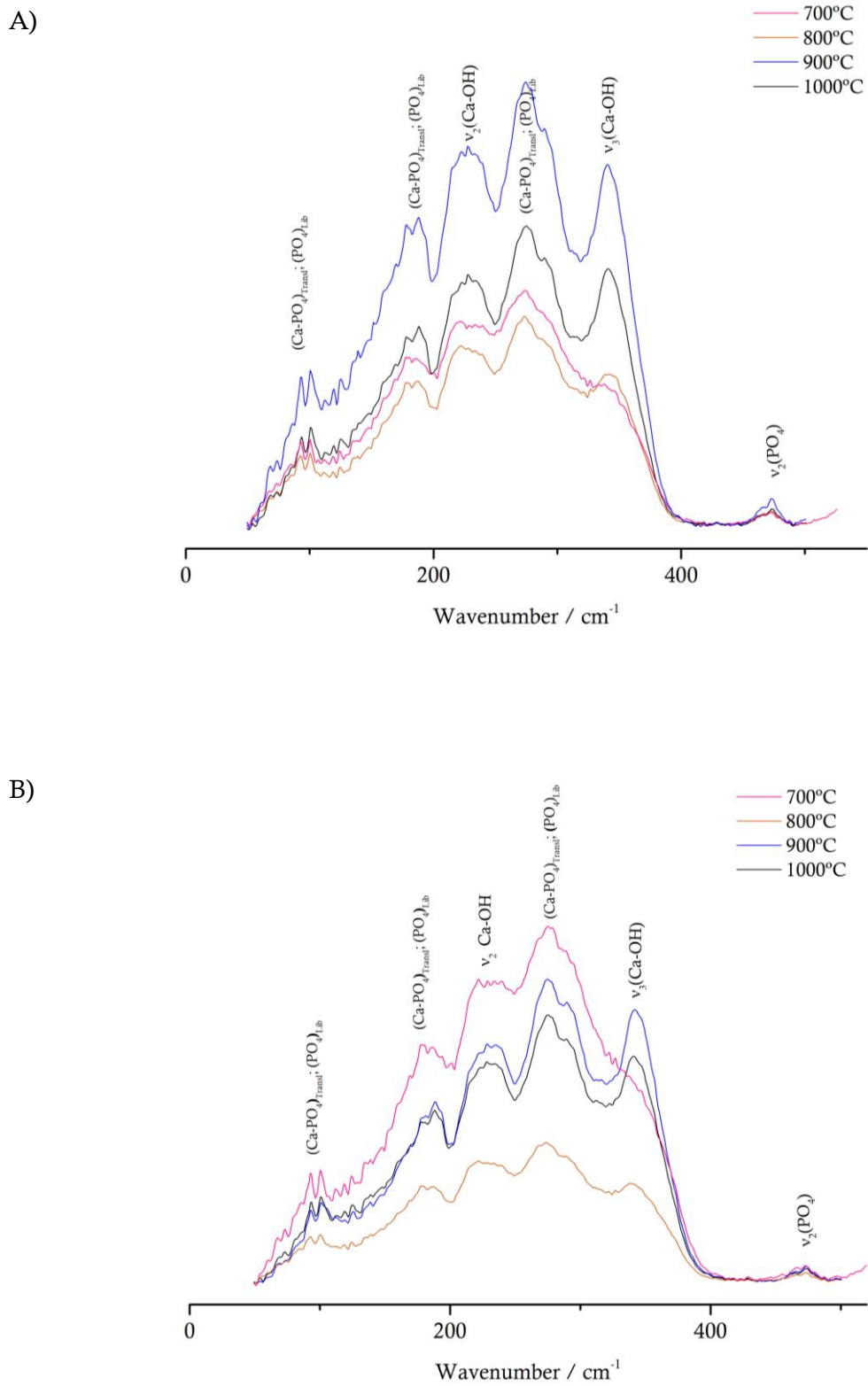


Figure 3.12. ATR spectra, in the far-IR region for (A) femur and (B) humerus samples of the skeleton CC_NI_42: burned at 700 °C (pink), 800 °C (brown), 900 °C (dark blue) and 1000 °C (black).

The fact that the bands in the far-IR region were less intense in the sample burned at 800 °C when compared to those burned at 700 and 900 °C (Figure 3.12) might suggest a transitional mineral structure, that was accompanied by the appearance of a band at 340 cm⁻¹ assigned to $\nu_3(\text{Ca-OH})$. This interesting feature may be a unique characteristic of samples burned between 700 and 800 °C, being very promising to estimate the exact temperature of exposure corresponding to the detection of this feature.

The spectral range from 500 – 700 cm⁻¹ (Figures 3.11 (A) and (B)) includes the $\nu_4(\text{PO}_4^{3-})$ vibrational mode which is characterised by two well defined bands at 562 and 602 cm⁻¹. Interestingly enough, the band at 562 cm⁻¹ suffered a shift to *ca.* 570 cm⁻¹ above 700 °C. These two signals at 562 and 602 cm⁻¹ are the consequence of the anisotropic electric field of the crystal lattice, that causes the degeneracy of the $\nu_4(\text{PO}_4^{3-})$ mode which splits into those two well defined features [101]. The previous hypothesis, of an intermediate crystal structure appearing between 700 °C and 800 °C, is reinforced by the shift of the $\nu_4(\text{PO}_4^{3-})$ band to 570 cm⁻¹ which suggests a different environment of the PO_4^{3-} groups. Besides this feature, a band at 630 cm⁻¹, assigned to OH⁻ librational mode, started to occur in the spectra of the samples burned between 700 and 800 °C.

Analysing the remaining spectral region, from 700 to 1850 cm⁻¹ (Figure 3.13), a very interesting feature was observed in the $\nu_1\nu_3(\text{PO}_4^{3-})$ domain. Beyond 700 °C, there was a sharpening of the band at *ca.* 960 cm⁻¹ ($\nu_1(\text{PO}_4^{3-})$), the shoulder at 1090 cm⁻¹ ($\nu_3(\text{PO}_4^{3-})_{\text{Fluorapatite}}$) became a well-defined peak, and there was a progressive deviation of the $\nu_3(\text{PO}_4^{3-})$ feature from 1020 cm⁻¹ to 1030 cm⁻¹, from the intact sample to the sample burned at 700 °C. From 800 to 1000 °C, this peak split into two, in femur (A): one at 1030 cm⁻¹ and the other at 1040 cm⁻¹ for the samples burned at 800 and 900 °C (the second peak in the sample burned at 1000 °C arising at 1044 cm⁻¹); in humerus (B): the sample burned at 800 °C displayed two peaks at 1030 and 1040 cm⁻¹ (for the remaining temperatures the second peak appeared at 1044 cm⁻¹).

As previously discussed, the $\nu_3(\text{PO}_4^{3-})$ band at 1020 cm⁻¹ is indicative of non-stoichiometric apatites, while a signal at 1030 cm⁻¹ indicates stoichiometric apatites [138]. The shift of this feature from the unburned to the burned sample at 700 °C indicates that bioapatite became stoichiometric between 400 and 700 °C. At 800 °C, the $\nu_3(\text{PO}_4^{3-})$ signal maximum got “flat”, which was, in fact, the appearance of another peak nearby. The $\nu_1\nu_3(\text{PO}_4^{3-})$ domain comprises contributions from many vibrational modes of the phosphate group in different environments [107, 137]. The definition of other $\nu(\text{PO}_4^{3-})$ vibrations in the spectra may support the existence of a different mineral phase starting to appear above 700 °C, since it suggests different phosphate environments, and consequently the hypothesis of a transitional mineral structure between 700 and 800 °C. On the other hand, this split of the $\nu_3(\text{PO}_4^{3-})$ band may also be caused by an increase in spectral resolution due to peaks sharpening.

3. Results and Discussion

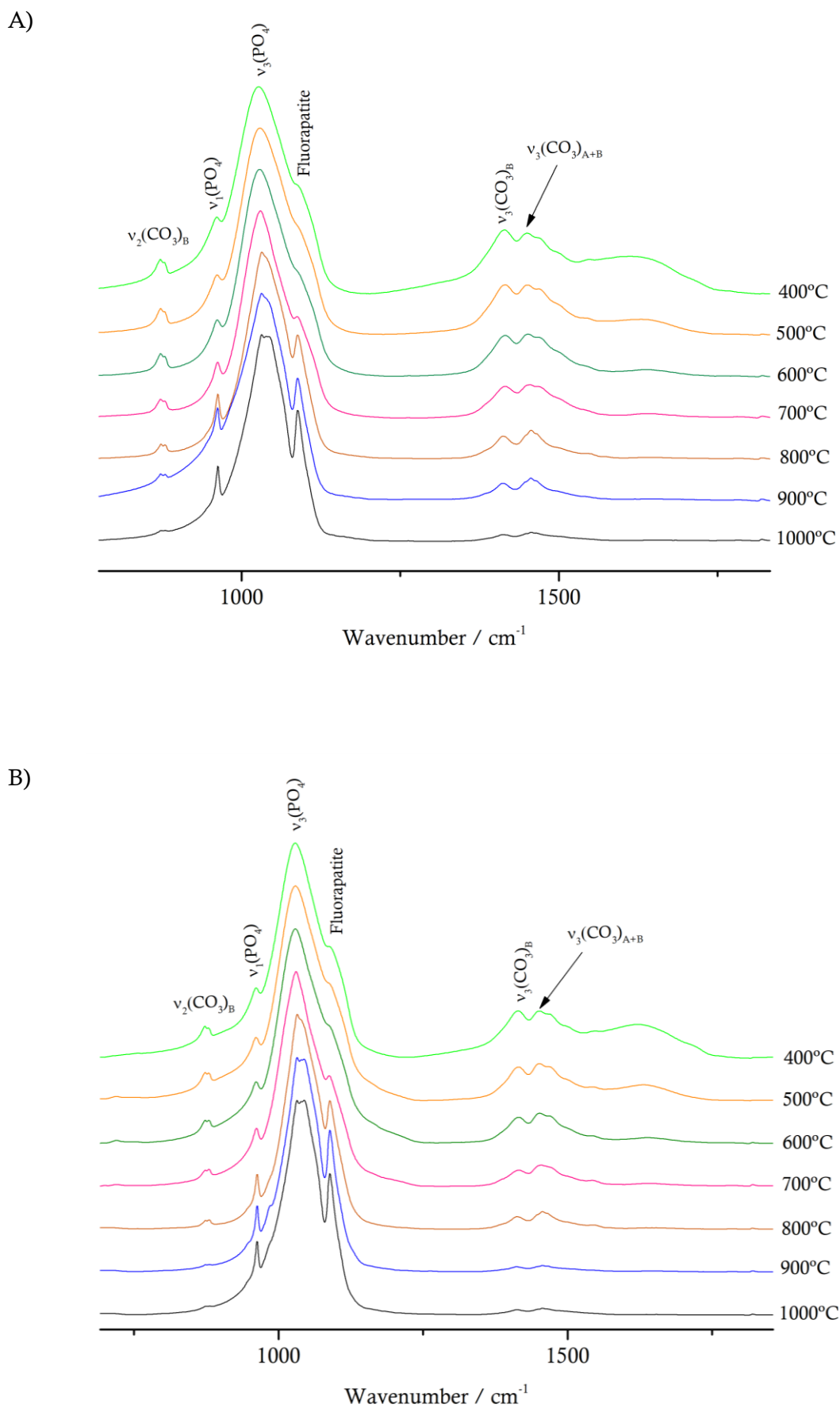


Figure 3.13. ATR spectra, in the 700 – 1850 cm^{-1} range for: (A) femur samples and (B) humerus samples of the skeleton CC_NI_42: burned from 400 to 1000°C.

The bands at 873, 879, 1415, 1450 and 1540 cm^{-1} are assigned to vibrational modes from carbonates (see Table 1.1), their intensity decreasing as temperature increased, as expected.

The band corresponding to the OH^- stretching mode from hydroxyapatite appeared at 3572 cm^{-1} in samples heated above 700 $^{\circ}\text{C}$, its intensity increasing with an increase in temperature.

To better analyse heat-induced chemical alterations in femur and humerus individually, and to better visualise the differences between these two types of bones, the mathematical relationships resumed in Table 2.2 were applied, the results being comprised in Table 3.4.

Table 3.4. CI, C/P, API, BPI, OH/P and C/C parameters calculated through FTIR-ATR data, for femur and humerus samples from the skeleton CC_NI_42: intact, enzymatically-treated and burned from 400 to 1000 $^{\circ}\text{C}$ for 120 min.

	Sample	CI	C/P	API	BPI	OH/P			C/C
						I	II	III	
Femur	Intact	3.709	0.310	0.952	1.077	-	-	-	0.962
	Enzymatically Treated	3.891	0.218	0.179	0.691	-	-	-	0.940
	400	3.590	0.306	0.499	0.928	-	-	-	0.989
	500	3.520	0.241	0.269	0.735	-	-	-	1.065
	600	3.590	0.195	0.185	0.587	-	-	-	1.115
	700	4.037	0.148	0.139	0.437	-	0.048	-	1.145
	800	4.759	0.107	0.072	0.278	0.455	0.163	0.487	1.120
	900	4.900	0.079	0.047	0.187	0.549	0.212	1.063	1.235
	1000	5.516	0.031	0.032	0.074	0.630	0.225	0.772	1.276
Humerus	Intact	3.729	0.355	1.157	1.224	-	-	-	0.982
	Enzymatically Treated	3.622	0.236	0.200	0.723	-	-	-	0.947
	400	3.805	0.217	0.372	0.645	-	-	-	1.046
	500	3.715	0.155	0.193	0.472	-	-	-	1.192
	600	3.650	0.121	0.121	0.375	-	-	-	1.261
	700	4.037	0.074	0.079	0.219	-	0.029	-	1.452
	800	4.804	0.057	0.049	0.154	0.472	0.175	0.329	1.534
	900	5.121	0.024	0.024	0.060	0.588	0.211	0.862	1.157
	1000	5.142	0.023	0.023	0.058	0.618	0.208	0.700	1.213

These values are graphically represented, to easily observe the tendencies and dependencies of each parameter with temperature. Note that the C/P-II index $((\text{API}+\text{BPI})/605)$ was not calculated, because it showed to be useless once it does not reflect the total carbonate content (thus not eliminating the interference of lipids from the C/C parameter) due to amide II band interference in the API parameter.

3. Results and Discussion

All the comparisons were made relative to the intact sample (for each type of bone), except the API parameter that was compared with the deproteinised sample. The decision of using the intact sample as a reference is justified in order not to introduce more factors of variation (*e.g.* enzymatic procedure introduces alterations and its significance was not completely evaluated). Since the API parameter was the most affected one by the presence of the organic material, not allowing its comparison with the burned samples because it is overestimated due to amide II band overlap, only this one was compared with the deproteinised sample.

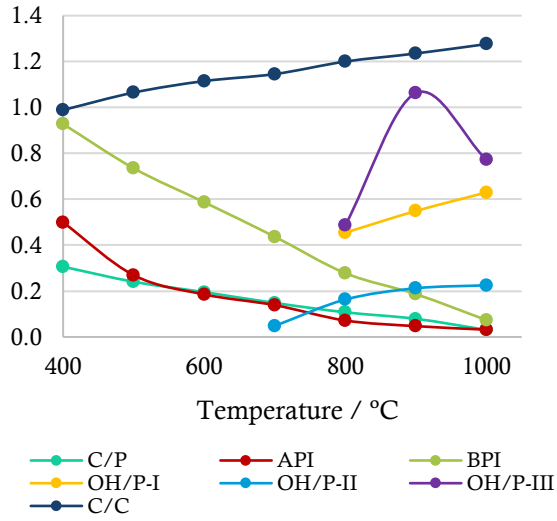
Figure 3.14 clearly showed that, although femur and humerus had different behaviours with temperature, overall all the calculated parameters had the same tendency as the temperature increased, *e. g.* the BPI parameter (light green) in femur (A) constantly decreased from 400 to 1000 °C; in humerus (B) as temperature increased the decrease in BPI was more abrupt, reaching a plateau value at 900 °C. Despite this different behaviour, the effect of temperature ends up being the same which, in this case, was well reflected in the BPI decrease.

The C/C parameter (Figure 3.14 (A) and (B), dark blue curve) had the most distinct variation with an increase in temperature, between humerus and femur. While in femur (Figure 3.14 (A)), it progressively increased from 0.962 to 1.276, in humerus (Figure 3.14 (B)) it increased from 0.982 to 1.534 at 800 °C then decreasing to 1.157 at 900 °C and slightly rising again to 1.213 at 1000 °C. This C/C value represents the relationship between carbonates (A+B) to carbonates B, its increase thus reflecting a different proportion of type A to type B carbonates caused by a rise of A carbonates or a decrease of B carbonates. However, any of these seem to make sense based on BPI (Figure 3.14 (A) and (B), light green) and API (Figure 3.14 (A) and (B), dark red) curves, which progressively decreased. On the other hand, the API parameter is highly doubtful because, in both unburned samples and samples burned at low temperatures the A carbonate band at 1540 cm⁻¹ is superimposed with the amide II feature of charred organic material.

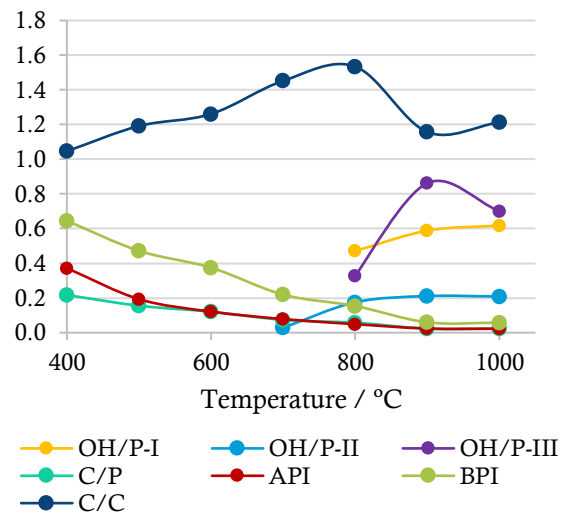
This temperature dependence of the C/C parameter had already been reported by Snoeck *et al.* [25]. According to Holcomb and Young [142], an increase in type A carbonates occurs from 600 to 800°C, due to the reaction between type B carbonates and CO₂ intermediates, which explains the opposite relationship observed for the C/C ratio. However, based on BPI and C/P curves (Figure 3.14 (A) and (B), light green and turquoise) the most reliable explanation for this increase in C/C as a consequence of temperature increase was the marked decrease in B carbonates relatively to A carbonates.

Holcomb and Young [142] also suggested that an A carbonates decrease at low burning temperatures with a concomitant increase of OH⁻ groups through reaction of carbonate with water and consequent release of CO₂ and OH⁻, the latter replacing type A carbonate. The results presented here showed an increase of OH⁻ above 800 °C, suggesting that OH⁻ groups progressively replace A type carbonates at high heating temperatures.

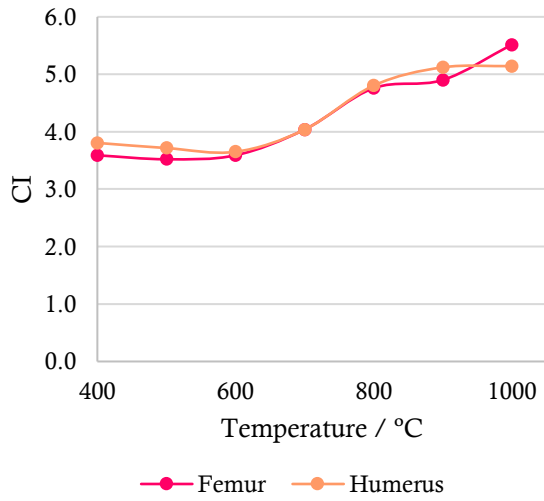
A)



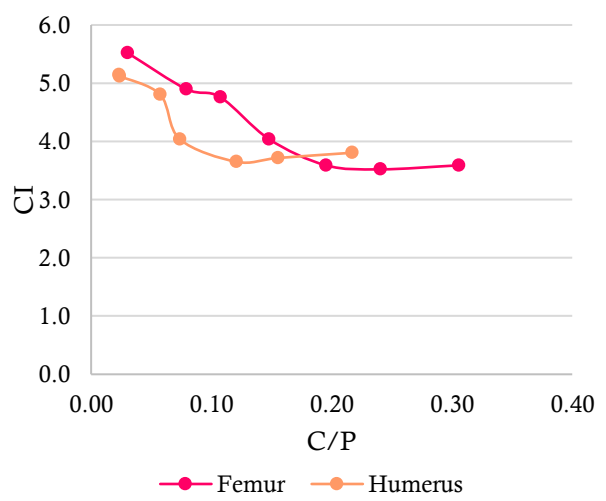
B)



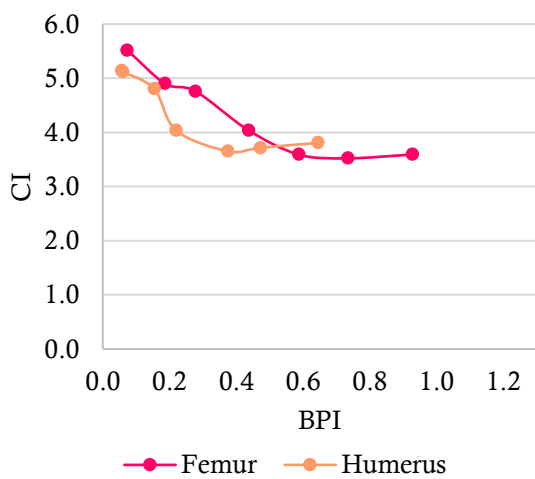
C)



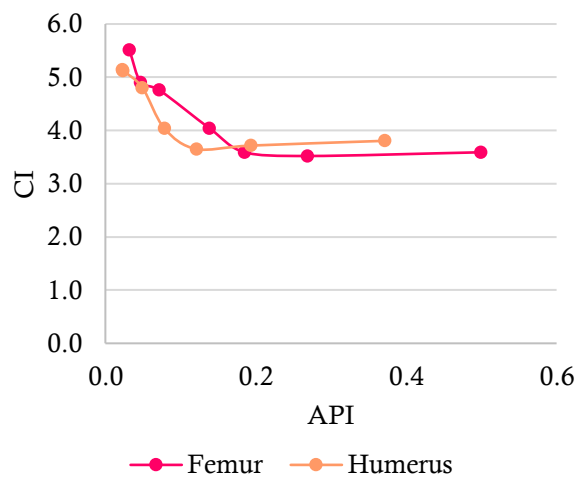
D)



E)



F)



3. Results and Discussion

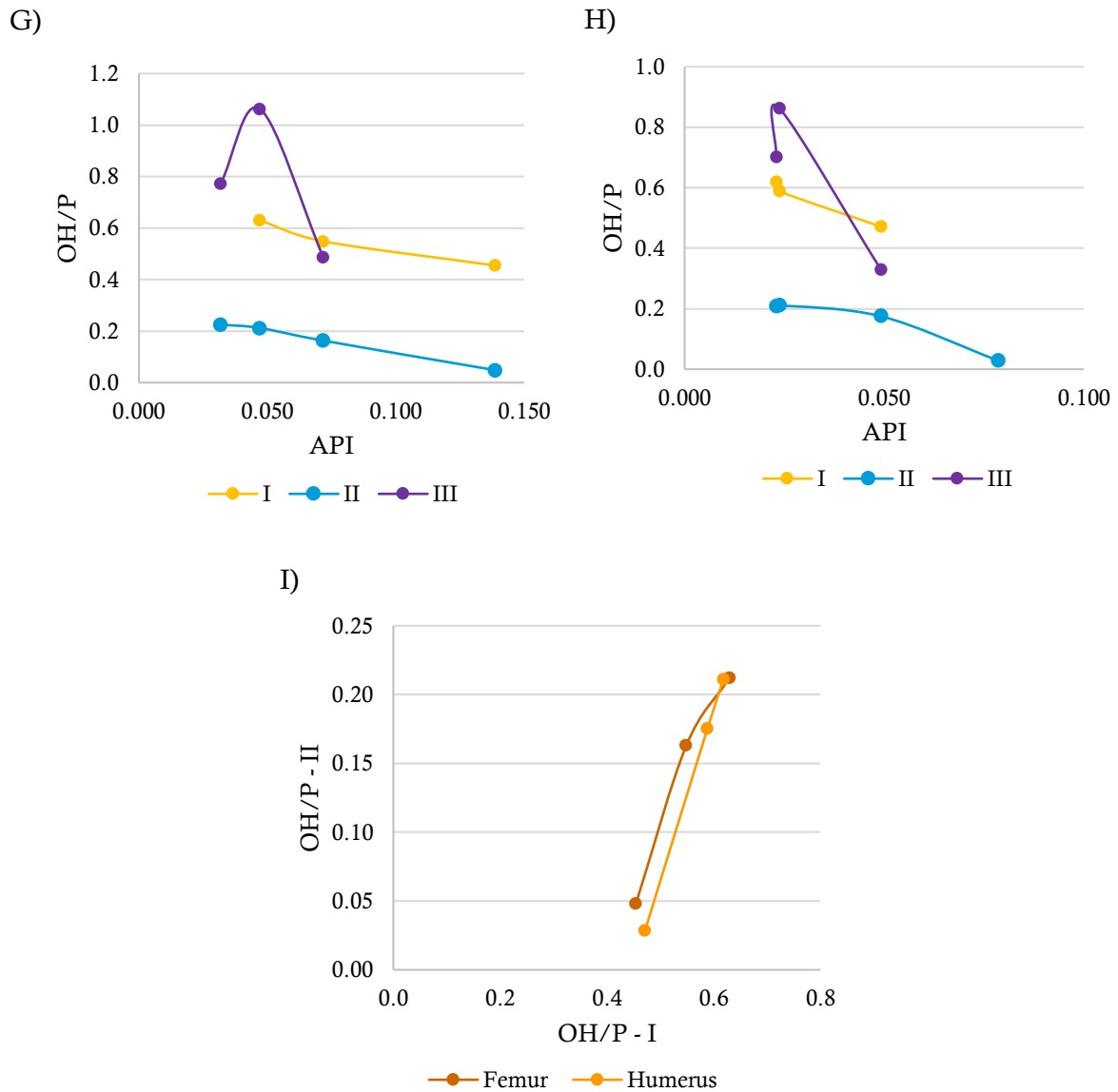


Figure 3.14. Graphic representation of the parameters' variation calculated using FTIR-ATR data: C/P (turquoise), OH/P (I, yellow; II, light blue; III, purple); BPI (light green), API (dark red), C/C (dark blue), as a function of temperature, for (A) femur and (B) humerus bone samples from skeleton CC_NI_42; CI for femur (dark pink) and humerus (light pink): (C) as a function of temperature, (D) as a function of C/P, (E) as a function of BPI and (F) as a function of API; (G) femur OH/P-I (yellow), II (light blue) and III (purple) as a function of API; (H) humerus OH/P-I (yellow), II (light blue) and III (purple) as a function of API; (I) OH/P-II as a function of OH/P-I in femur (orange) and humerus (brown).

Alterations in CI (Figure 3.14 (C)) with temperature were quite similar between femur and humerus. Both bones showed a slight decrease in crystallinity up to 600 °C, confirming the results obtained by Castillo *et al.* [14] who analysed histological changes in bone tissue as a consequence of heating and reported the appearance of irregular and not geometrically distributed crystallites at 600 °C. Crystallinity in femur and humerus started to increase between 600 and 700 °C. Femur

reached a plateau phase between 800 and 900 °C, increasing again at 1000 °C, while in humerus this plateau phase occurred between 900 and 1000 °C.

The slight crystallinity decrease observed up to 600 °C must be verified by XRD analysis, as presently verified (see section 3.3.4.1), although this decrease may be caused by the contraction of the collagen fibrils upon heating [121]. The alterations in the crystallinity of bioapatite started between 600 °C and 700 °C, due to the thermal shielding effect of the organic matrix which protects the inorganic moiety until its total destruction.

The relationship between CI and C/P was inversely proportional: as CI increased C/P-I decreased (Figure 3.14 (D)). Interestingly, analysing the CI values as a function of BPI (Figure 3.14 (E)), the curve had exactly the same profile as CI vs. C/P-I relationship. The same did not occur with the plot representing CI vs. API suggesting that C/P-I and BPI represent the same, have the same behaviour upon heating, and display the same relationship with CI, thus being redundant ratios. Accordingly, only one of them should be used. Although, for burning temperatures above 800 °C the carbonate content is very low, its calculations being unreliable, if of study interest the most suitable ratio for its estimation is BPI, since, as already discussed, the band assigned to $\nu_3(\text{PO}_4^{3-})$ has contributions from other vibrational modes of phosphate which interfere within this signal, rendering the C/P calculation a little confusing.

In this study, two new mathematical relationships related to the OH⁻ bone content were introduced: OH/P-II, based on the stretching OH⁻ band at 3572 cm⁻¹, and OH/P-III, based on the $\nu_3(\text{Ca-OH})$ band at 340 cm⁻¹. These ratios, as well as OH/P-I (based on the OH libration band at 630 cm⁻¹, proposed by Snoeck *et al.* [25]) were only applied to samples heated above 800 °C because the corresponding peaks were only detected from this temperature on. Presently, the OH/P-II ratio was also applied for the samples burned at 700 °C, as the 3572 cm⁻¹ signal was already visible (upon band deconvolution with Gaussian function).

As clearly visible in Figure 3.14 (A) and (B), for both femur and humerus the purple, yellow and light blue curves (respecting to OH⁻ content) had the same behaviour with an increase in temperature: OH/P-I and OH/P-II gradually increased while OH/P-III reached its lowest value at 800 °C, the highest at 900 °C and an in-between value at 1000 °C. The OH⁻ content is directly related to the type A carbonate content – in theory, the higher the amount of type A carbonates the lower is the OH⁻ content, as depicted in Figure 3.14 (G) and (H) by OH/P-I (yellow curve) and OH/P-II (light blue curve), and in Figure 3.14 (I) (OH/P-I and OH/P-II increased concomitantly, this behaviour being common for both bones). The profile curve of the OH/P-III plot as a function of temperature (Figure 3.14 (G) and (H), purple) was completely different relative to the OH/P-I and OH/P-II curves, but similar in both femur and humerus, suggesting that this ratio is probably related to a different environment of the (Ca-OH) bond within the lattice. OH/P-III has great potential for the estimation of the burning temperature within the 700 - 1000 °C range, because the 340 cm⁻¹ peak appeared at some point between 700 and 800 °C, indicating temperatures of exposure higher than 700 °C. Also, it seems to display a very characteristic curve assuming distinct values at

3. Results and Discussion

each heating temperature. Obviously, this hypothesis should be tested in different types of bones (apart from femur and humerus) from distinct individuals, as well as for different periods of heating exposure.

3.3.2. Raman Spectroscopy

3.3.2.1. Raman Microspectroscopy with a 514 nm Laser Line

Unburned samples were impossible to analyse by Raman spectroscopy using a 514 nm laser line, the organic components of bone completely overriding the spectrum due to fluorescence.

Regarding the evaluation of the efficiency of the protocols for defatting and deproteinisation of the bone samples, an enzymatically-treated femur sample was analysed (Figure 3.15).

As already verified, the enzymatic procedure was not completely efficient. In an attempt to obtain a spectrum, different areas of the sample were tested, looking for an area with less interference of fluorescence. When a range with a significant Raman signal was found, the sample was subject to photobleaching for *ca.* 2.30 h, despite the possibility of chemical alteration caused by excessive exposure to the laser radiation [76]. Analysing Figure 3.15, only the peaks $\nu_1(\text{PO}_4^{3-})$ at 960 cm^{-1} , $\nu_3(\text{PO}_4^{3-})$ at 1046 cm^{-1} and $\nu_1(\text{CO}_3^{2-})$ at 1070 cm^{-1} were visible. The calculation of the Raman parameters in Table 2.2 although not totally reliable, were possible for the relationships related to clearly detected peaks, namely maturity/crystallinity ratio (0.071) and C/P-I (0.142), after baseline subtraction in the range $915 - 1200\text{ cm}^{-1}$. The C/P-I value, in particular, is doubtful because the $\nu_3(\text{PO}_4^{3-})$ and $\nu_1(\text{CO}_3^{2-})$ bands are partially overlapped (Figure 3.15).

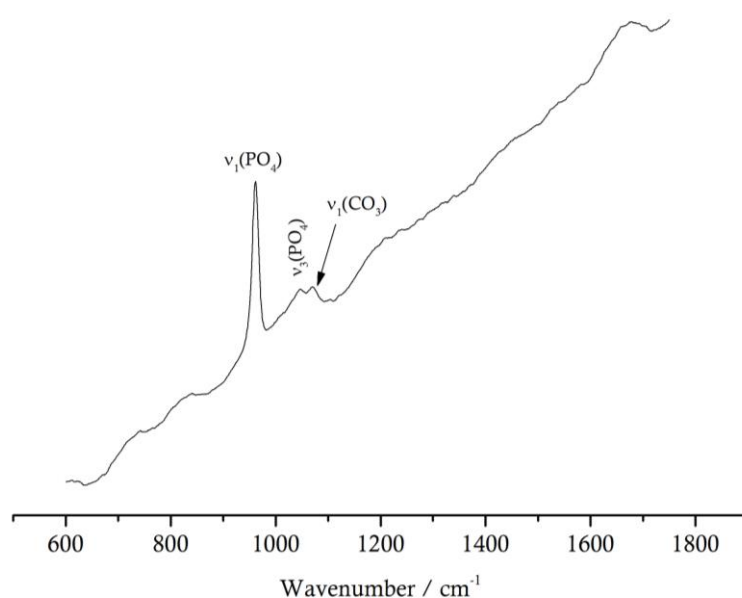


Figure 3.15. Raman spectrum of the enzymatically-treated femur sample from the skeleton CC_NI_42, collected with a laser line of 514 nm, in the range 600 – 1800 cm⁻¹.

Bachman and Ellis [143] proved that although collagen is the major source of fluorescence, the mineral fraction may also be fluorescent due to the fact that bioapatite is a halophosphate (may contain fluorine and/or chlorine, which is verified by the detection of fluorapatite in FTIR-ATR spectra). This means that the fluorescence in the enzymatically-treated sample may not be caused only by the organic material, unsuccessfully removed.

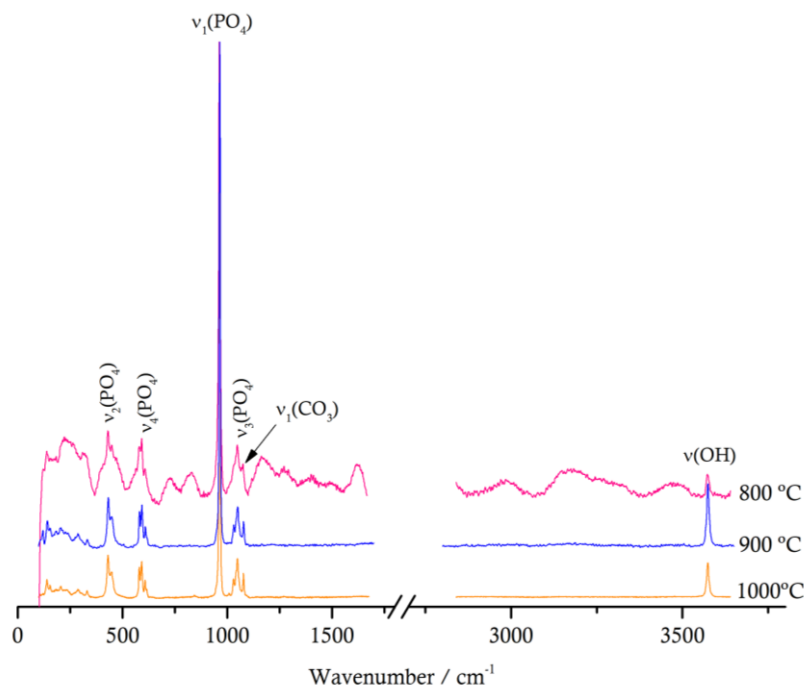
Since the organic constituents (lipids and proteins) of bone burn out up to 600 °C, it was thought that would be possible to analyse those samples burned at 700 °C. However, fluorescence from the samples saturated the CCD detector, and only those burned above 800 °C were possible to analyse with the 514 nm laser line. Yet, the 800 °C sample was still subject to photobleaching for 1.30 h (Figure 3.16). It seems that the presence of the halogens within the crystal lattice are the source of the fluorescence of the samples burned between 600 and 800 °C [143]. The occurrence of a re-crystallisation phase between 700 and 800°C, with the consequent exclusion of the halogen activator atoms from the lattice, is a possible explanation for the absence of fluorescence above 800 °C.

Figure 3.16 includes the Raman spectra (after baseline subtraction) of the samples heated at 800, 900 and 1000 °C, for femur (A and B) and humerus (C and D).

In both sets of spectra, peaks got sharper as temperature increased, especially those assigned to $\nu_2(\text{PO}_4^{3-})$, at 430 cm^{-1} , $\nu_4(\text{PO}_4^{3-})$ at 591 cm^{-1} , $\nu_3(\text{PO}_4^{3-})$ at 1049 cm^{-1} and $\nu_1(\text{CO}_3^{2-})$ at 1076 cm^{-1} . The OH⁻ stretching band at 3573 cm^{-1} was more intense for the samples burned at 900 °C.

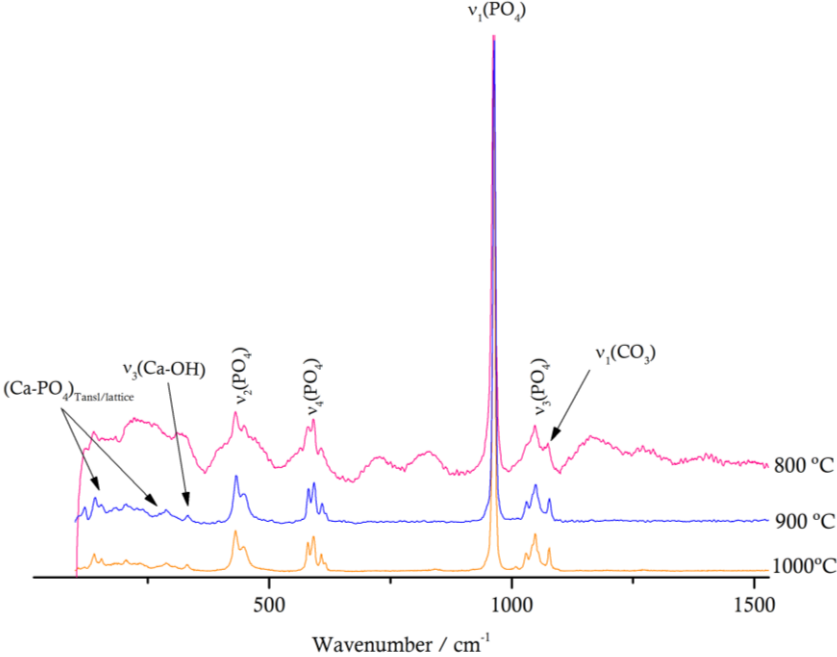
The band assigned to $\nu_3(\text{Ca-OH})$, at 330 cm^{-1} , and the $(\text{Ca-PO}_4)_{\text{translation/lattice modes}}$, below 320 cm^{-1} , started being visible in the samples burned at 900 and 1000 °C, due to interference of fluorescence however, their intensity was very low and unchangeable from 900 to 1000 °C.

A)

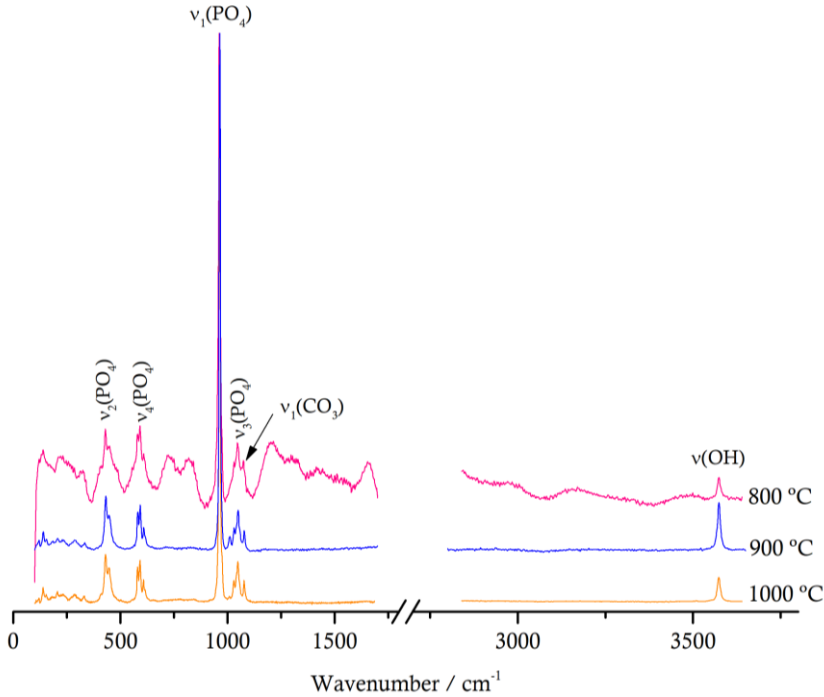


3. Results and Discussion

B)



C)



D)

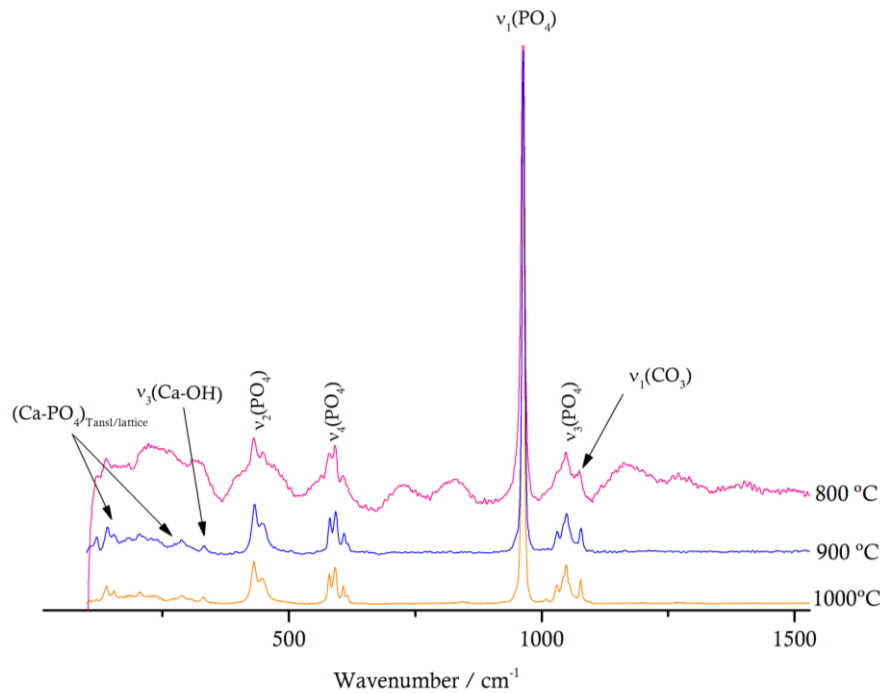


Figure 3.16. Raman spectra, collected with the laser line of 514 nm, of samples from the skeleton CC_NI_42: (A) femur samples burned from 800 to 1000 °C, in the range 0 - 3800 cm^{-1} , (B) femur samples burned from 800 to 1000 °C in the 270 – 1200 cm^{-1} range, (C) humerus samples burned from 800 to 1000 °C, in the range 0 - 3800 cm^{-1} , (D) humerus samples burned from 800 to 1000 °C in the 270 – 1500 cm^{-1} range.

Similarly to the procedure analysis followed for the infrared data, the mathematical relationships comprised in Table 2.2 related to Raman analysis were applied. Table 3.5 summarises the calculated parameters, graphically represented in Figure 3.17, obtained for the femur and humerus samples under study.

Table 3.5. Calculation of the maturity/crystallinity, C/P and OH/P parameters for femur and humerus from skeleton CC_NI_42, upon burning at temperatures of 800, 900 and 1000 °C, for 120 min, obtained through Raman spectroscopy with a 514 nm laser line.

Sample	Temperature	Maturity/Crystallinity	C/P		OH/P
			I	II	
Femur	800	0.120	0.153	0.117	0.061
	900	0.153	0.293	0.092	0.530
	1000	0.180	0.239	0.070	0.318
Humerus	800	0.108	0.212	0.147	0.057
	900	0.138	0.136	0.048	0.383
	1000	0.150	0.155	0.049	0.219

3. Results and Discussion

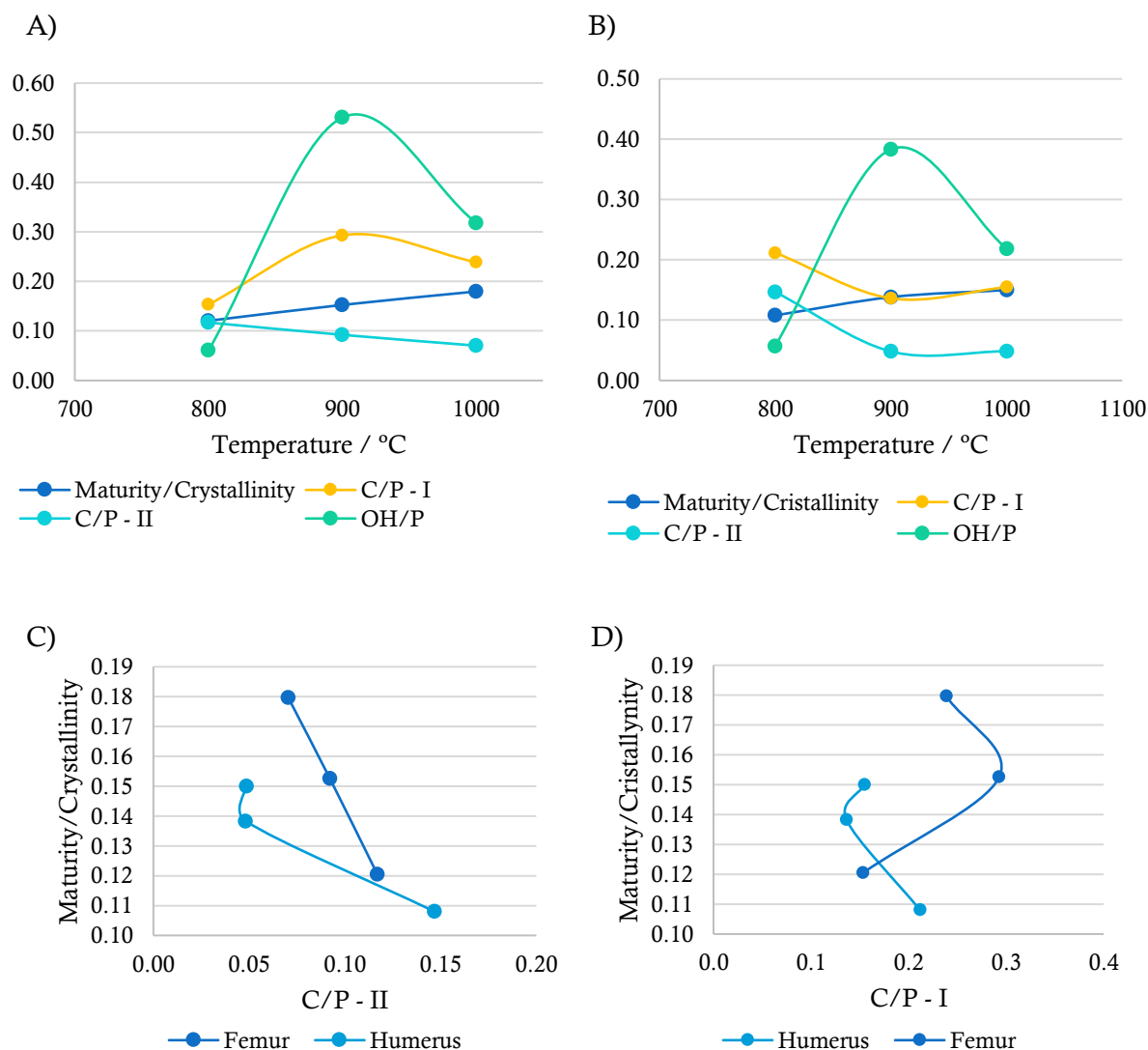


Figure 3.17. Graphic representation of the parameters' variation as a function of temperature, based on Raman data (with a 514 nm laser line): C/P-I (yellow), C/P-II (light blue); OH/P (turquoise); Maturity/Crystallinity (dark blue), for femur (A) and humerus (B) bone samples from skeleton CC_NI_42; (C) Maturity/Crystallinity as a function of C/P-II for femur (dark blue) and humerus (light blue); (D) Maturity/Crystallinity as a function of C/P-I for femur (dark blue) and humerus (light blue).

Contrary to the infrared results, the OH⁻ content calculation based on the $\nu(\text{OH})$ band, at 3573 cm^{-1} , did not gradually increased with temperature. In Raman, this ratio had its lowest value at $800\text{ }^{\circ}\text{C}$, the highest at $900\text{ }^{\circ}\text{C}$ and an in-between value at $1000\text{ }^{\circ}\text{C}$, for both types of bone (Figure 3.17 (A) and (B)). Since Raman intensities are not directly proportional to concentration (contrary to FTIR), the OH Raman profile did not show the gradual increment observed by FTIR-ATR.

The maturity/crystallinity ratio (Figure 3.17 (A) and (B)) increased with temperature in both types of bone (femur and humerus), corroborating the infrared results. Since crystallinity increases with temperature, the maturity of the crystals will also be higher because the crystal lattice is more ordered; consequently, this parameter increased with temperature.

Surprisingly, the C/P-I and C/P-II ratios (Figure 3.17 (A) and (B)), which represent the type B carbonate to phosphate content (based on the $\nu_1(\text{PO}_4^{3-})$ band at 960 cm^{-1} and $\nu_2(\text{PO}_4^{3-})$ at 430 cm^{-1} , respectively) had completely different behaviours as a function of temperature for each type of bone. While in femur the C/P-I increased from 800 to 900 °C, reaching its highest value at 900 °C and decreasing again at 1000 °C (intermediate value), C/P-II displayed gradual decreasing values as temperature increased. In humerus, C/P-I decreased from 800 to 900 °C, remaining constant at 1000 °C, and C/P-II decreased from 800 to 900 °C, slightly increasing at 1000 °C. Also, crystallinity and maturity of the bioapatite crystals is entirely related to carbonate content. As maturity/crystallinity increases it is expected that the C/P ratio decreases, which is consistent with the C/P-II ratio results (Figure 3.17 (C)).

The fact that C/P-I did not reflect this dependency with temperature and crystallinity (Figure 3.17 (D)) is probably related to the fact that the $\nu_1(\text{PO}_4^{3-})$ band suffers interference from tissue orientation (*i.e.* the orientation of the crystal layers within bioapatite) [136, 144].

3.3.2.2. Raman Microspectroscopy with a 785 nm Laser Line

Since the Ar^+ laser line at 514 nm did not allow the collection of Raman spectra for bones burned below 800 °C, a diode laser line at 785 nm was tested on these samples.

Figure 3.18 represents the Raman spectrum of the intact bone sample.

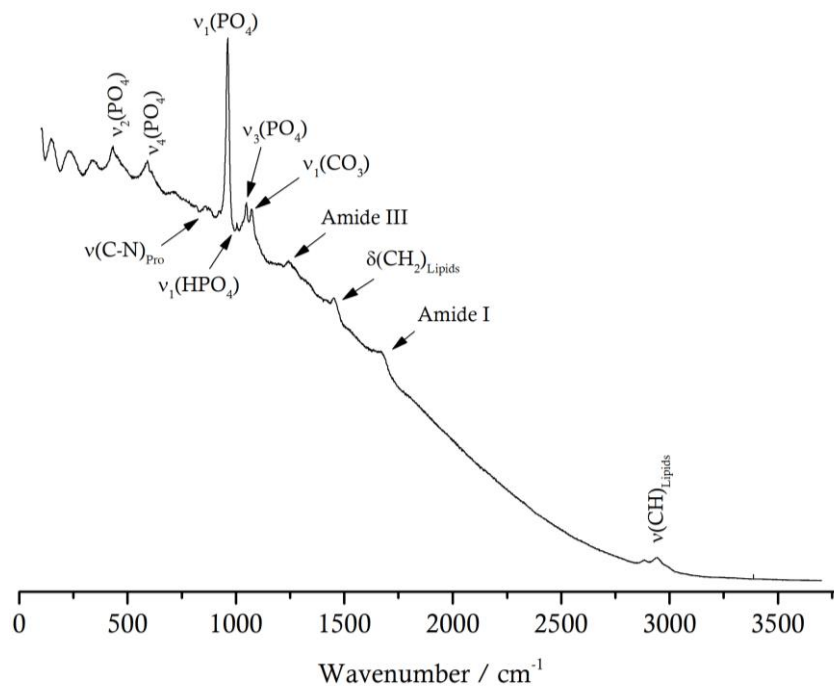


Figure 3.18. Raman spectrum of an unburned femur sample from skeleton CC_NI_42, collected with a 785 nm laser line, in the range 0 – 3750 cm⁻¹.

3. Results and Discussion

Despite the presence of some fluorescence, all the Raman signals of bioapatite and organic components were visible: $\nu_2(\text{PO}_4^{3-})$, $\nu_4(\text{PO}_4^{3-})$, $\nu(\text{CN})_{\text{Pro}}$, $\nu_1(\text{PO}_4^{3-})$, $\nu_1(\text{HPO}_4^{2-})$, $\nu_3(\text{PO}_4^{3-})$, $\nu_1(\text{CO}_3^{2-})$, amide III, $\delta(\text{CH}_2)_{\text{Lipids}}$, amide I and $\nu(\text{CH})_{\text{Lipids}}$ (at 430, 590, 858, 960, 1003, 1049, 1070, 1241, 1454, 1675 and 1883-2941 cm^{-1} , respectively), allowing to calculate the ratios comprised in Table 2.2.

The maturity/crystallinity ratio for the unburned bone was, as expected, very low (Table 3.6). The mineral to matrix ratio, in turn, reflects the amount of mineralization of bone, being naturally quite high. C/P showed higher values for the unburned bone sample, as expected, when compared with burned femur analysed with a 514 nm laser line.

Table 3.6. Calculation of the maturity/crystallinity, C/P and OH/P parameters for an unburned femur sample from skeleton CC_NI_42, through Raman spectroscopy with a 785 nm laser line.

Maturity/Crystallinity	C/P		Mineral/Matrix
	I	II	
0.062	0.422	0.192	2.562

Even though the 785 nm laser enabled the acquisition of the spectrum of the unburned bone sample, the same did not occur for the samples burned below 800 °C. These results are presented in Figures 3.19 and 3.20.

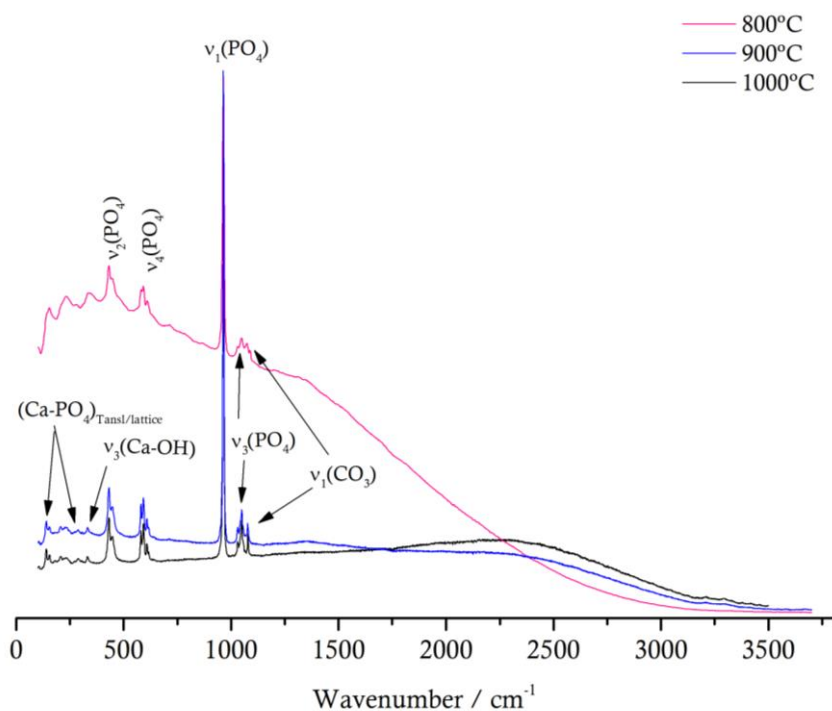
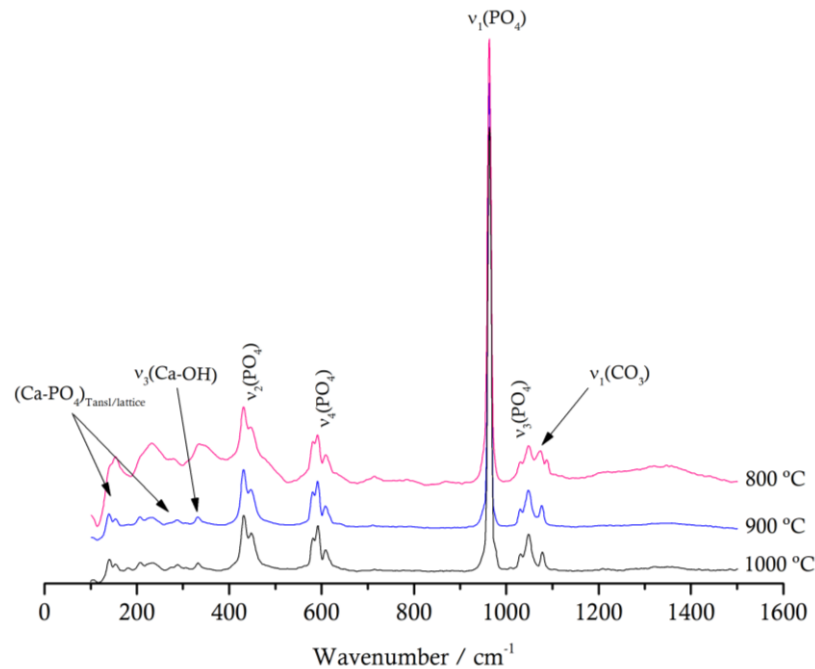


Figure 3.19. Raman spectra, in the range 0 – 3750 cm^{-1} collected with the laser of 785 nm of femur samples from the skeleton CC_NI_42, burned between 800 and 1000 °C.

In Figure 3.19, the absence of the band at 3573 cm^{-1} was noteworthy. As the 785 nm laser is less energetic than the 514 nm one, some vibrational modes are not visible, namely the $\nu(\text{OH}^-)$ band at 3573 cm^{-1} , hindering calculation of the OH/P ratio.

Figure 3.20 (A) and (B) contain the Raman spectra of the samples burned at 800 , 900 and $1000\text{ }^\circ\text{C}$ for femur and humerus samples, respectively. As temperature increased the peaks got sharper and well defined, similarly to the results obtained with the 514 nm laser.

A)



B)

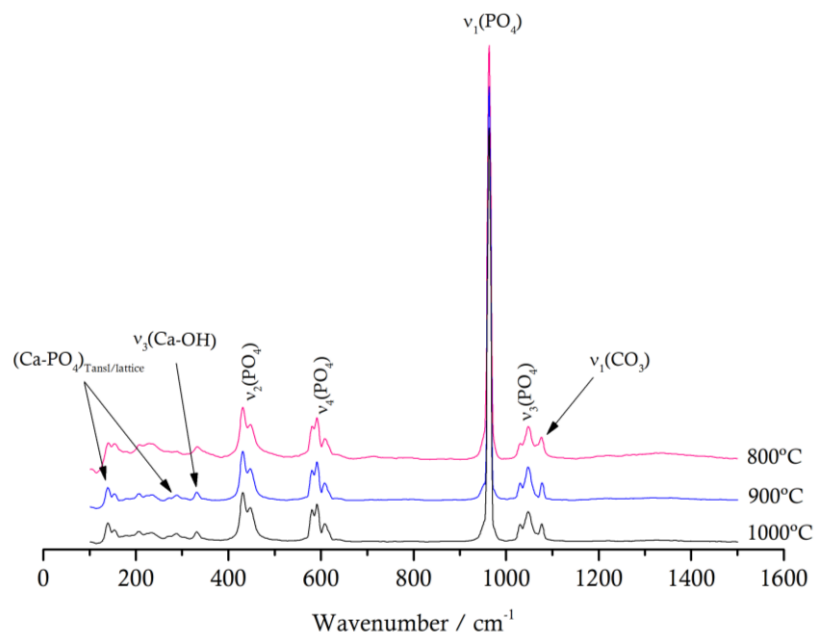


Figure 3.20. Raman spectra, in the range $0 - 1600\text{ cm}^{-1}$ collected with the laser of 785 nm of bone samples from the skeleton CC_NI_42: (A) femur and (B) humerus, burned between 800 and $1000\text{ }^\circ\text{C}$.

3. Results and Discussion

Comparing the results obtained with both laser lines, no significant shifts were observed. However, due to the lower energy of the 785 nm radiation the weaker vibrational modes were not visible with this laser.

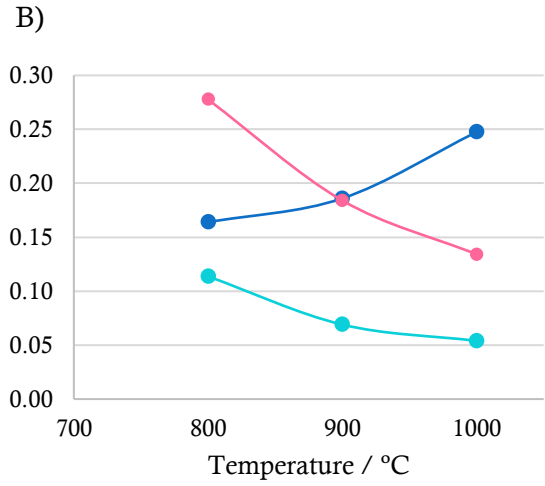
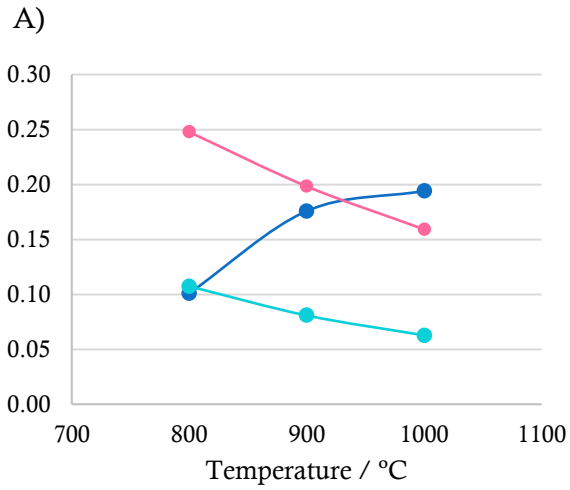
The ratios in Table 2.2 were also calculated with the Raman data obtained with the 785 nm laser (Table 3.7) and are compared with the 514 nm results in Figure 3.21.

Table 3.7. Calculation of the maturity/crystallinity and C/P parameters for femur and humerus bone samples from skeleton CC_NI_42, burned at different temperatures (°C), based on Raman data with the 785 nm laser.

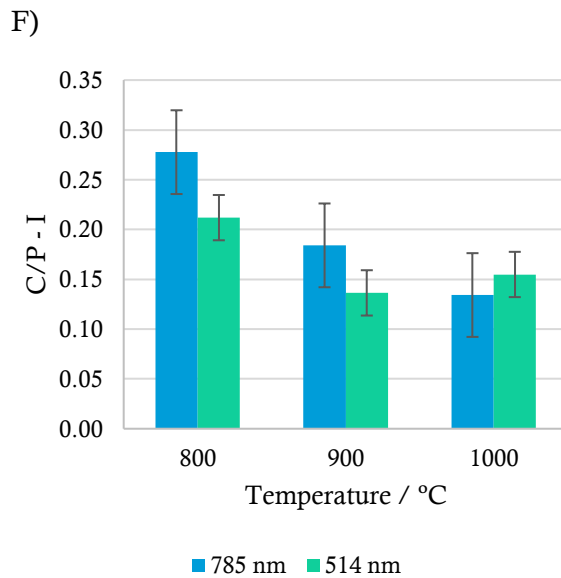
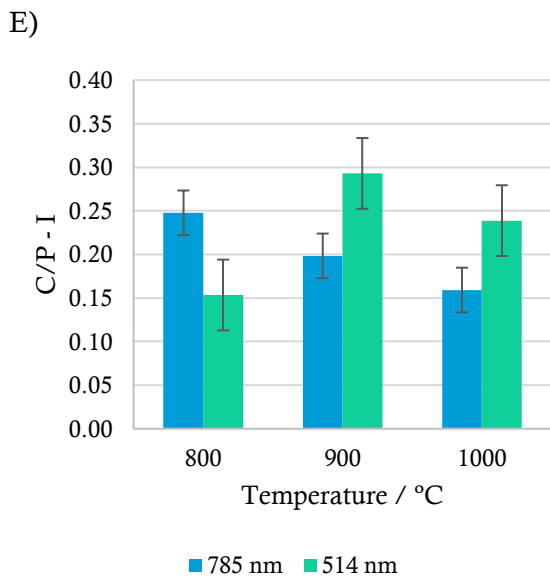
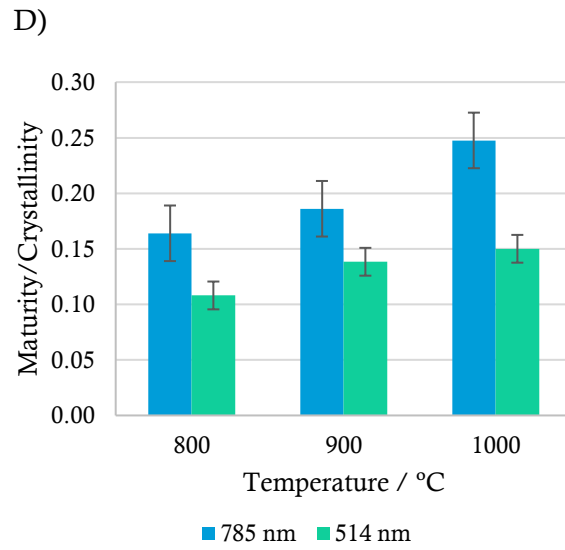
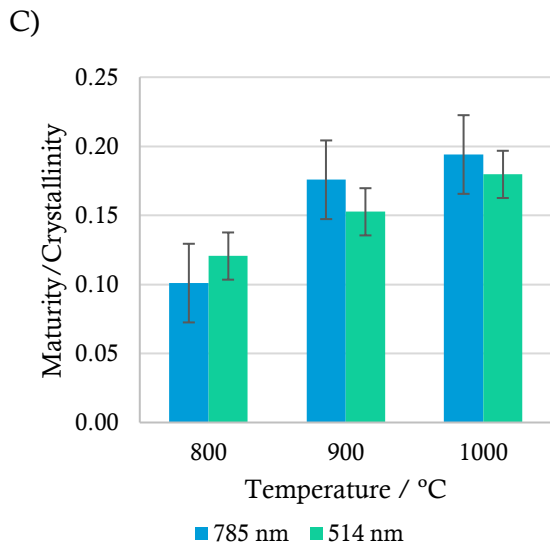
Sample	Temperature	Maturity/Crystallinity	C/P	
			I	II
Femur	800	0.101	0.248	0.107
	900	0.176	0.198	0.081
	1000	0.194	0.159	0.063
Humerus	800	0.164	0.278	0.114
	900	0.186	0.184	0.069
	1000	0.248	0.134	0.054

It is important to assess any possible difference between both sets of results, as these are relevant for the development of a new bioanthropological method. Figure 3.21 (A) and (B) revealed that the temperature dependency of the parameters calculated through the spectral data collected with the 514 and 785 nm lasers was the same: maturity/crystallinity increased, C/P-I and C/P-II decreased as temperature increased. The only parameter that varied with the laser energy was C/P-I: with the 785 nm laser line, it decreased as temperature rose, for both bones, as expected since the carbonate content is progressively lower; with the 514 nm laser, it increased for femur, with an increase of temperature (Figure 3.21 (C)). This opposite result reflected the tissue orientation effect on the the $\nu_1(\text{PO}_4^{3-})$ mode, confirming that C/P-II is a better parameter than C/P-I. In fact, its behaviour was more consistent when analysing distinct types of bone and different laser lines.

In Figure 3.21 (C) to (H) the values obtained for all the parameters, at distinct temperatures, using different excitation sources, were compared for femur and humerus. Apart from the temperature dependency of each parameter for being the same in both bones, all ratios (except the C/P-I, as mentioned above) displayed the same behaviour with an increase in temperature and both laser lines produced results leading to identical conclusions, indicating that the technique may be applied to forensic samples independently of the Raman excitation source.



● Maturity/Crystallinity ● C/P - I ● C/P - II ● Maturity/Crystallinity ● C/P - I ● C/P - II



3. Results and Discussion

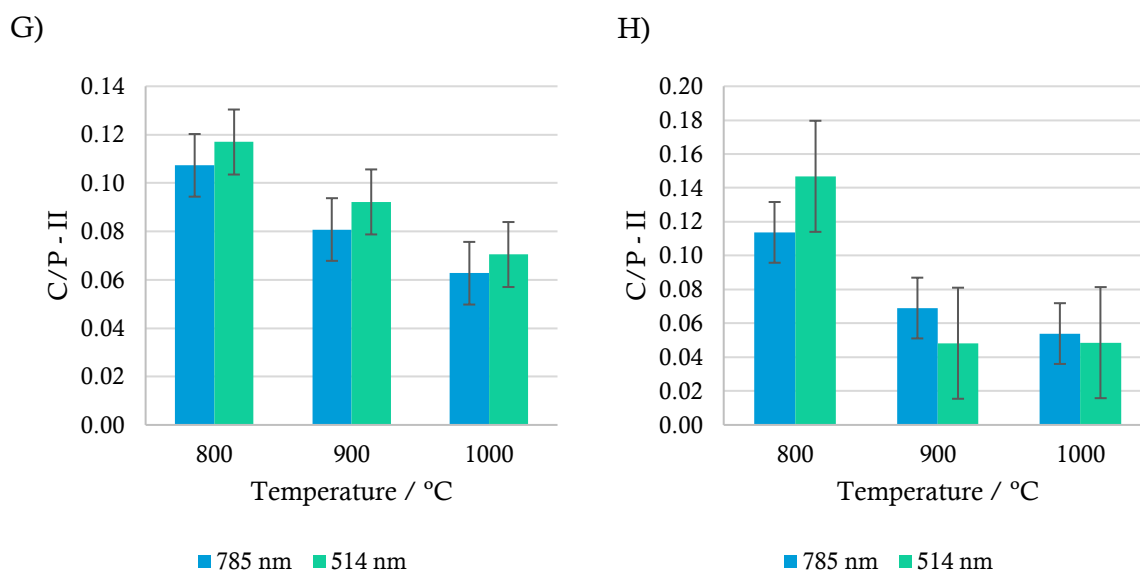


Figure 3.21. Graphical representation of the temperature dependence of the calculated parameters using Raman data obtained with the 785 nm laser: C/P-I, C/P-II, and Maturity/Crystallinity for femur (A) and humerus (B) bone samples from skeleton CC_NI_42; (C), (E) and (G) Maturity/Crystallinity, C/P-I and C/P-II for femur, from data obtained with the 514 nm (turquoise) and 785 nm (blue) lasers; (D), (F) and (H) Maturity/Crystallinity, C/P-I and C/P-II for humerus, from data obtained with the 514 nm (turquoise) and 785 nm (blue) lasers.

3.3.2.3. *FT-Raman Spectroscopy, Low Temperature FT-Raman and CARS Spectroscopies*

In order to obtain the Raman spectra of the samples burned at low and intermediate temperatures (below 700 °C), Fourier transform Raman (FT-Raman, 1064 nm laser line), low temperature Fourier transform Raman (LT-FT-Raman) and Coherent Anti-Stokes Raman (CARS) spectroscopies were applied. The results for the humerus samples burned at 700 and 400 °C are comprised in Figure 3.22.

Both spectra were expected to display similar results to those obtained with the 514 nm and 785 nm laser lines, maintaining the particular characteristics of each sample: for the bone burned at 400 °C (B), remaining organic material was expected to be observed ($\delta(\text{CH}_2)_{\text{Lipids}}$, amide I and $\nu(\text{CH})_{\text{Lipids}}$ at 1241, 1454, 1675 and 1883-2941 cm^{-1} , respectively), along with relatively broad peaks from bioapatite ($\nu_2(\text{PO}_4^{3-})$, $\nu_4(\text{PO}_4^{3-})$, $\nu_1(\text{PO}_4^{3-})$, $\nu_3(\text{PO}_4^{3-})$, $\nu_1(\text{CO}_3^{2-})$, at 430, 590, 960, 1049, 1070, respectively). For the sample burned at 700 °C, in turn it would be foreseen to detect only the peaks related to bioapatite. In both cases, the spectra could not be obtained with either 514 or 785 nm lasers, due to fluorescence.

Since a change of the excitation source wavelength appears not to be enough to overcome fluorescence CARS experiments were carried out, this being considered a suitable approach for

Raman analysis of low temperature burned bones, once the result signal is blue-shifted and more intense than the Stokes Raman scattering, which may possibly overcome fluorescence. In order to perform CARS analysis, the pump laser was scanned to 746.7 nm, to obtain an image from the distribution of phosphates at 960 cm^{-1} ($\nu_1(\text{PO}_4^{3-})$). However, no image could be obtained, because the sample slice was too irregular rendering microscope focusing impossible and thus hindering a proper image collection. Further optimisation of the sample preparation procedure is therefore needed.

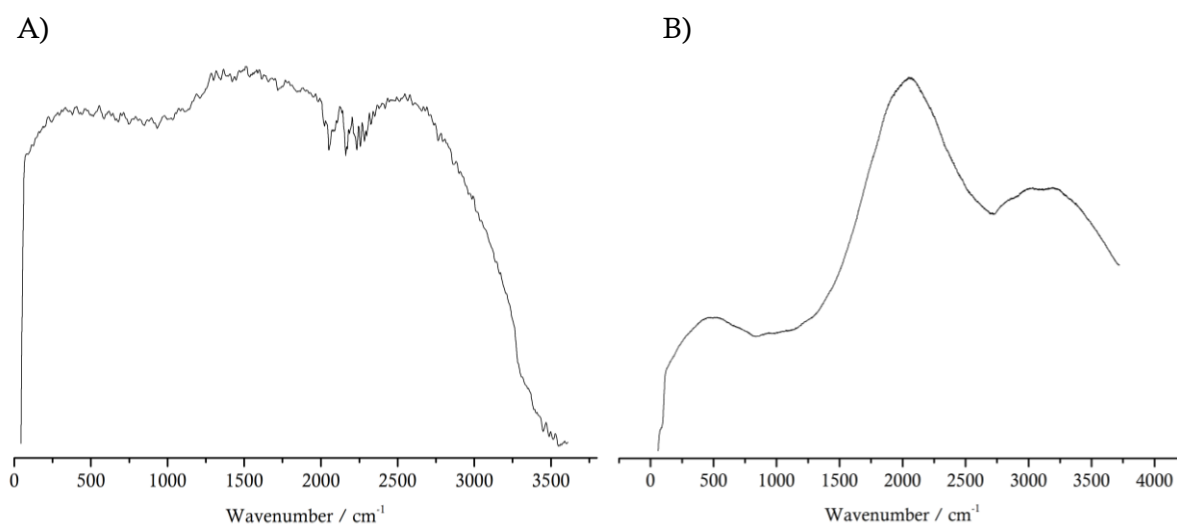


Figure 3.22. (A) FT-Raman spectrum of humerus sample from the skeleton CC_NI_42, burned at 700°C; (B) Low Temperature FT-Raman spectrum of humerus sample from the skeleton CC_NI_42, burned at 400°C.

3.3.3. Inelastic Neutron Scattering Spectroscopy

INS analysis was performed in the MAPS and TOSCA spectrometers. While the latter has a higher sensitivity in the 0 to 2000 cm^{-1} range, MAPS's sensitivity is higher above 2000 cm^{-1} .

Figure 3.23 (A) and (B), contains TOSCA results for the femur and humerus burned samples, respectively. As temperature increased, the peaks got gradually sharper and more defined, the biggest alterations taking place above 700 °C . At lower temperatures, the presence of traces of organic matter lead to severe peak broadening due to protein and lipids high hydrogen content, the OH⁻ libration at 650 cm^{-1} and the lattice vibrational modes ($0 - 500\text{ cm}^{-1}$) being the only visible bands. Between 600 and 700 °C the organic material was totally destroyed (peaks related to the inorganic matrix started appearing at 700 °C), confirming the previous results.

3. Results and Discussion

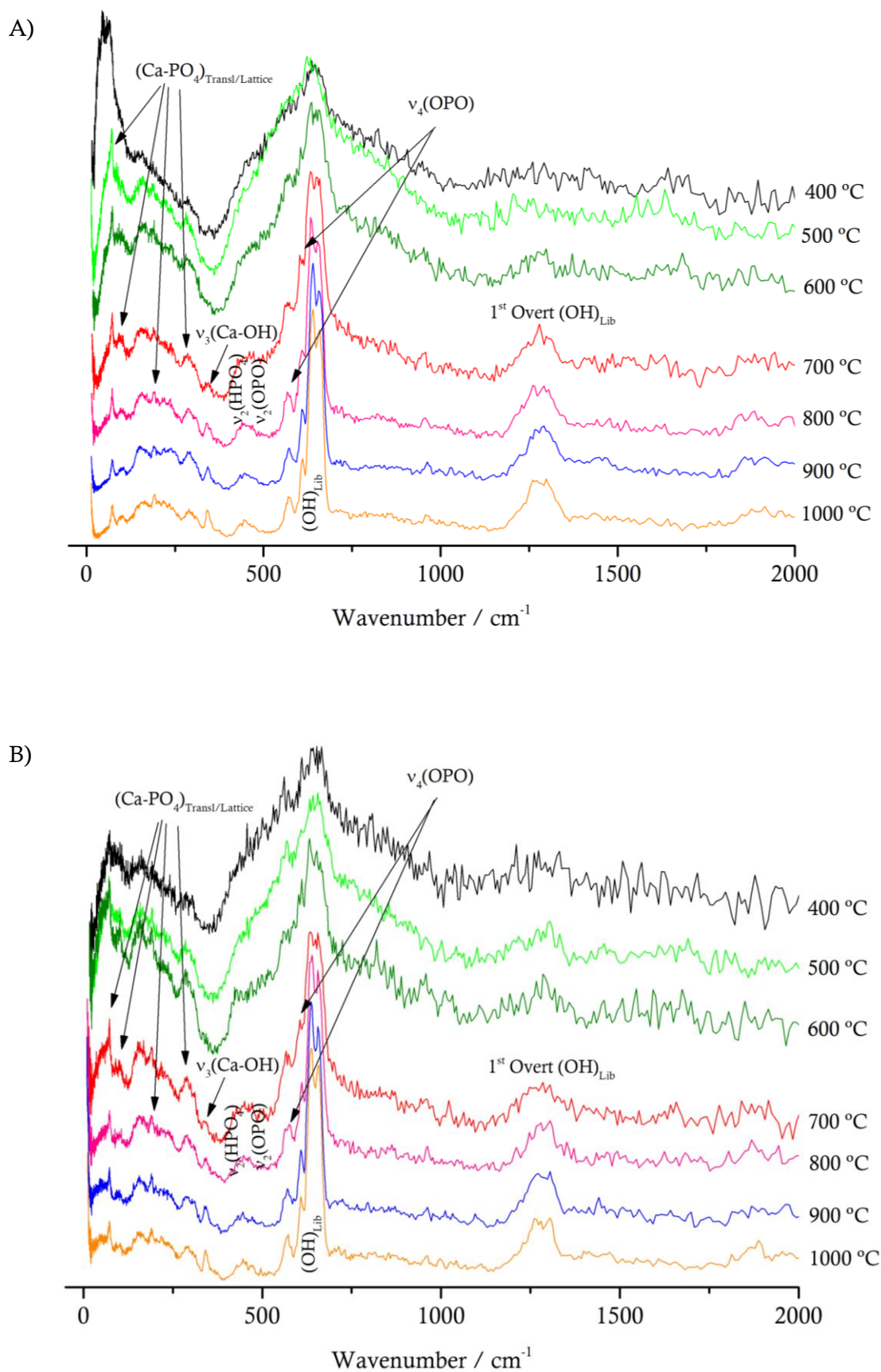


Figure 3.23. Inelastic neutron scattering spectra, collected in TOSCA, for femur (A) and humerus (B) samples from the skeleton CC_NI_42 burned between 400 and 1000°C.

INS data collected in TOSCA, in the 0 - 500 cm^{-1} interval is especially informative regarding alterations within the crystal lattice, allowing to confirm the analysis based on infrared spectroscopy in the far-IR region. Similarly to IR data, the peak assigned to $\nu_3(\text{Ca-OH})$, at 340 cm^{-1} , started to appear at 700 $^{\circ}\text{C}$, being clearly visible at 800 $^{\circ}\text{C}$ and above. As temperature increased, it gradually increased in intensity, indicating a larger number of (Ca-OH) bonds with a different environment within the crystal lattice. The bands assigned to the vibration of (Ca-PO₄) from the lattice, at *ca.* 160, 190 and 290 cm^{-1} , were progressively more intense, suggesting more ordered lattices. The features at 400 – 500 cm^{-1} assigned to $\nu_2(\text{HPO}_4^{2-})$ and to $\nu_2(\text{OPO})$ were observed in samples burned above 800 $^{\circ}\text{C}$, suggesting (in agreement with FTIR-ATR results) the presence of a different phosphate environment in the lattice. The peak at 1280 cm^{-1} assigned to first overtone of the OH⁻ librational mode, occurred for samples burned above 700 $^{\circ}\text{C}$, corroborating the previous estimation by FTIR-ATR regarding the OH⁻ band appearance (between 700 and 800 $^{\circ}\text{C}$).

The band at 640 cm^{-1} respecting the OH⁻ librational mode appeared split above 600 $^{\circ}\text{C}$, in femur (Figure 3.23 (A)), one of these peaks is at 632 cm^{-1} and the other at 657 cm^{-1} , in the samples burned at 600, 700 and 800 $^{\circ}\text{C}$. In the samples burned at 900 and 1000 $^{\circ}\text{C}$ the first peak appeared shifted to 639 cm^{-1} . In humerus (Figure 3.23 (B)), the OH⁻ librational mode split was visible above 700 $^{\circ}\text{C}$, exhibiting the first peak at 634 cm^{-1} and the second at 657 cm^{-1} . For the samples burned at 800, 900 and 1000 $^{\circ}\text{C}$ this first peak was shifted to 637 cm^{-1} . Suggesting different environments of the H atoms as temperature increases.

MAPS results (Figure 3.24 (A) and (B)) showed a band profile progression with temperature very similar to that observed through TOSCA: the bands from the organic components disappeared above 600 $^{\circ}\text{C}$, the inorganic constituents of bone standing out above 700 $^{\circ}\text{C}$.

The OH⁻ libration, at 653 cm^{-1} was progressively sharper as temperature increased and underwent a shift to 642 cm^{-1} , in humerus and to 655 cm^{-1} , in femur. The first, second and third overtones of the OH⁻ librational mode, at 1305, 1911 and 2586 cm^{-1} started being visible in samples heated above 700, 800 and 1000 $^{\circ}\text{C}$, respectively, giving reliable estimations of temperature exposure. The OH⁻ stretching band at 3593 cm^{-1} started to be detected in humerus samples burned at 600 $^{\circ}\text{C}$, being shifted to 3587 cm^{-1} as temperature increases.

These shifts in the OH⁻ librational and OH⁻ stretching bands have already been reported for femur, by Marques *et al.* [44], suggesting that heating does not eliminate the structural differences caused by the intrinsic features of each bone.

In femur samples, the combination band ((OH⁻)_{lib}+ ν (OH)) appeared at 4224 cm^{-1} , while in humerus it was observed at 4232 cm^{-1} , for temperatures above 700 $^{\circ}\text{C}$.

3. Results and Discussion

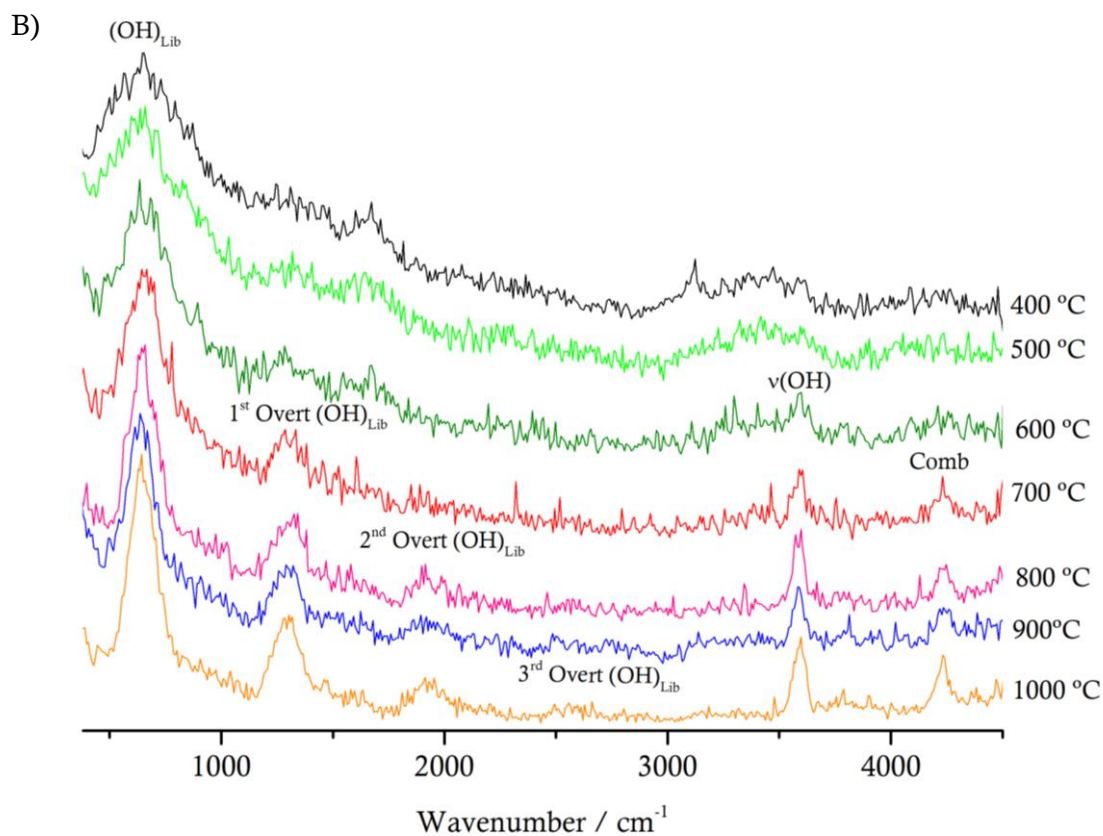
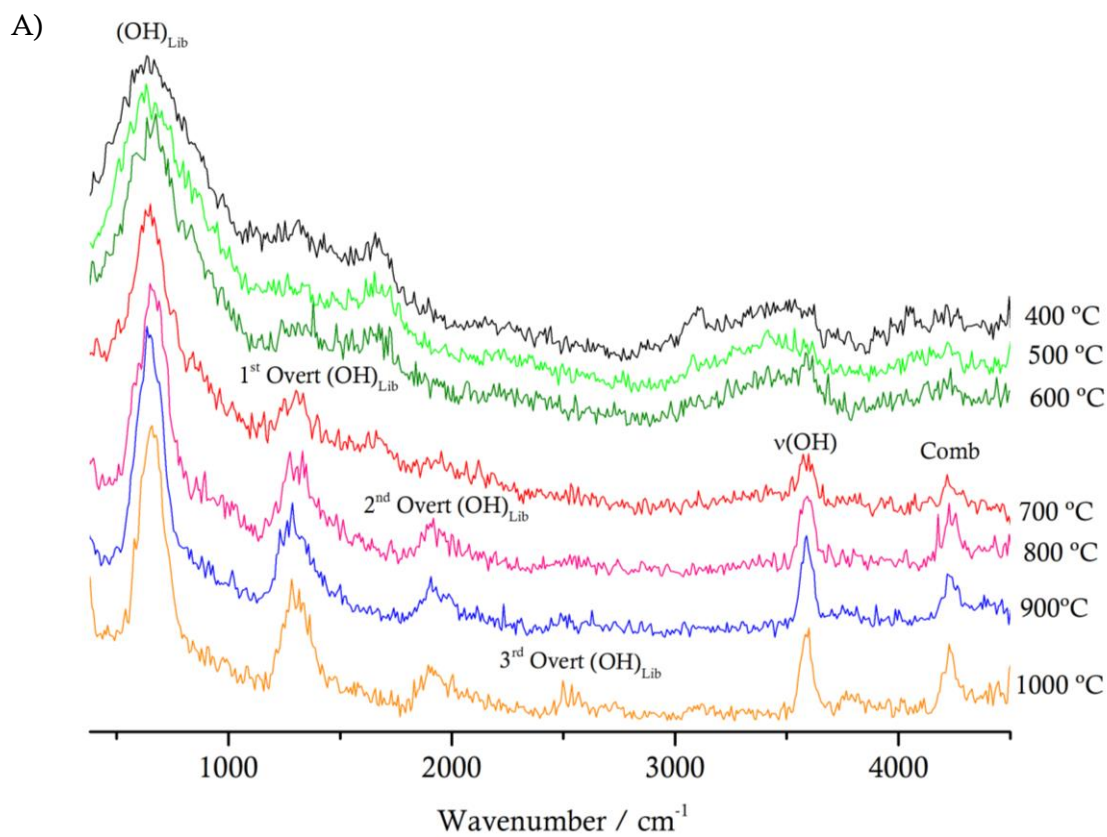
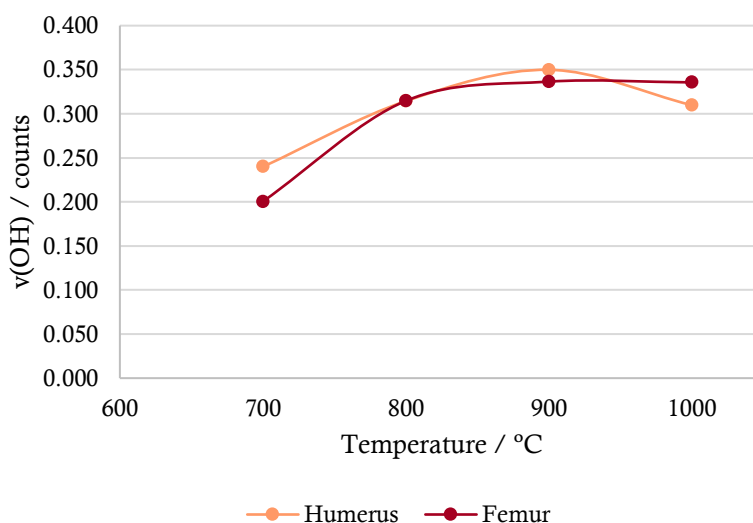


Figure 3.24. Inelastic neutron scattering spectra, collected in MAPS, for bone samples from skeleton CC_NI_42, burned at temperatures between 400 and 1000 °C: femur (A) and humerus (B).

Once INS is especially sensitive to H atoms, and the intensity of the bands is directly proportional to the number of scattering atoms, it is a good moment to compare INS data with the OH content estimation obtained by FTIR-ATR and Raman (Figure 3.25).



3.25. Graphical representation of the temperature dependence of the $\nu(\text{OH})$ INS band intensity, for humerus and femur samples from skeleton CC_NI_42.

By analysis of Figure 3.25 it is possible to conclude that the estimation based on the FTIR-ATR OH/P-II parameter (Figure 3.14 (A) and (B), light blue curves, and Table 3.4) agrees with the INS data (corresponding to the OH⁻ stretching band): in femur, the OH⁻ content increased from 700 to 900 °C, remaining relatively constant for higher temperatures, while in humerus it increased with temperature reaching its highest value at 900 °C and then slightly decreasing at 1000 °C.

3.3.4. Diffraction Methods

3.3.4.1. X-Ray Powder diffraction

Regarding the study of the effect of heating on the crystallinity of bioapatite, and the formation of new inorganic phases, X-ray powder diffraction (XRPD) was performed. Besides the diffracting plane profile, the crystallinity index was also evaluated as well as the dimension of the crystals through length and thickness calculation (based on Table 2.2).

The biggest disadvantage of XRPD is the fact that amorphous compounds do not yield a XRPD signal. Due to the low crystallinity of bioapatite, the XRPD diffractograms of unburned and

3. Results and Discussion

low temperature burned samples displayed overlapping peaks (as evidenced in Figure 3.26) with low intensity (not visible in the Figure 3.26 due to the normalisation function applied to the diffractograms).

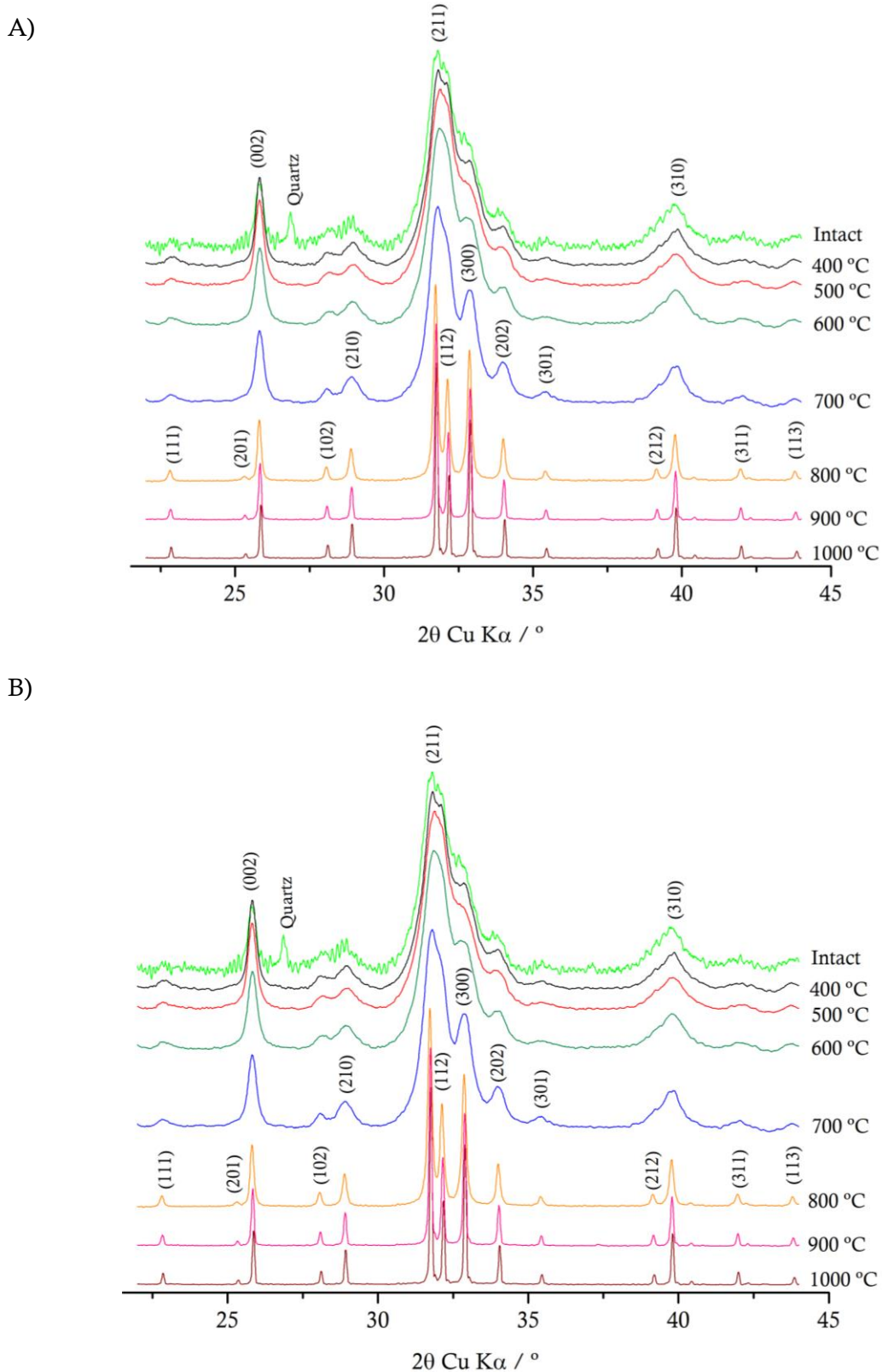


Figure 3.26. X-ray diffractograms, in the range 22 - 43°, using Cu K α radiation, for bone samples from skeleton CC_NI_42: intact and burned at temperatures between 400 and 1000 °C; femur (A) and humerus (B).

Observing Figure 3.26 it is possible to conclude that in both types of bone (femur and humerus), only above 800 °C the peaks got sharper and defined. Two distinct mineral phases were clearly observed at temperatures below 700 °C and above 800 °C, corroborating the previously discussed transitional lattice structure in the 700 – 800 °C temperature range, based on vibrational data.

Interestingly enough, unburned samples displayed a peak at 26.9°, indicating the presence of quartz (diffracting plane (101); consequent of post-burial diagenesis) [38], that was not present in the burned samples (Figure 3.26). Regarding the possible formation of new mineral phases, no additional phases were visible in the diffractograms. As temperature increased above 800 °C, the mineral phase progressed to a purest form of hydroxyapatite.

The crystallinity index calculation by X-ray powder diffraction is based on the reflections of the planes (211), (112), (300) and (202), according to the XRPD CI relationship described in Table 2.2 and Figure 2.3. Relating CI with the values obtained through the Scherrer equation, it is established a connection between peak width and the crystal size effect [145]. Applying the Scherrer equation to (002) and (310) diffracting peaks it is obtained the information on crystals length (*c*-axis) and thickness (perpendicular to the *c*-axis), respectively [136]. Table 3.8 and Figure 3.27 summarise the values of the dimensions of the crystals and the crystallinity obtained for each bone sample under analysis.

Table 3.8. Calculated CI and crystal thickness and length (Å), through XRD results, for femur and humerus samples from skeleton CC_NI_42: intact and burned at temperatures between 400 and 1000 °C.

Sample	Temperature	Thickness	Length	CI
Femur	Intact	1.730	4.508	0.034
	400	1.728	4.868	0.036
	500	1.596	4.462	0.021
	600	1.643	4.201	0.052
	700	2.270	4.564	0.237
	800	10.468	9.991	1.202
	900	16.294	14.445	1.270
	1000	18.290	15.963	1.293
Humerus	Intact	1.592	4.577	0.042
	400	1.991	5.136	0.067
	500	1.651	4.842	0.038
	600	1.787	4.481	0.078
	700	2.525	4.824	0.326
	800	7.681	7.328	0.980
	900	17.297	15.372	1.275
	1000	18.328	16.260	1.293

3. Results and Discussion

In unburned samples, the crystallinity of bioapatite was close to zero (Figure 3.27 (A) and (B), light green curve), with crystal dimensions around 2 Å thickness and 5 Å length, reflecting small, long and thin crystals, consistent with disordered structures with high lattice strain.

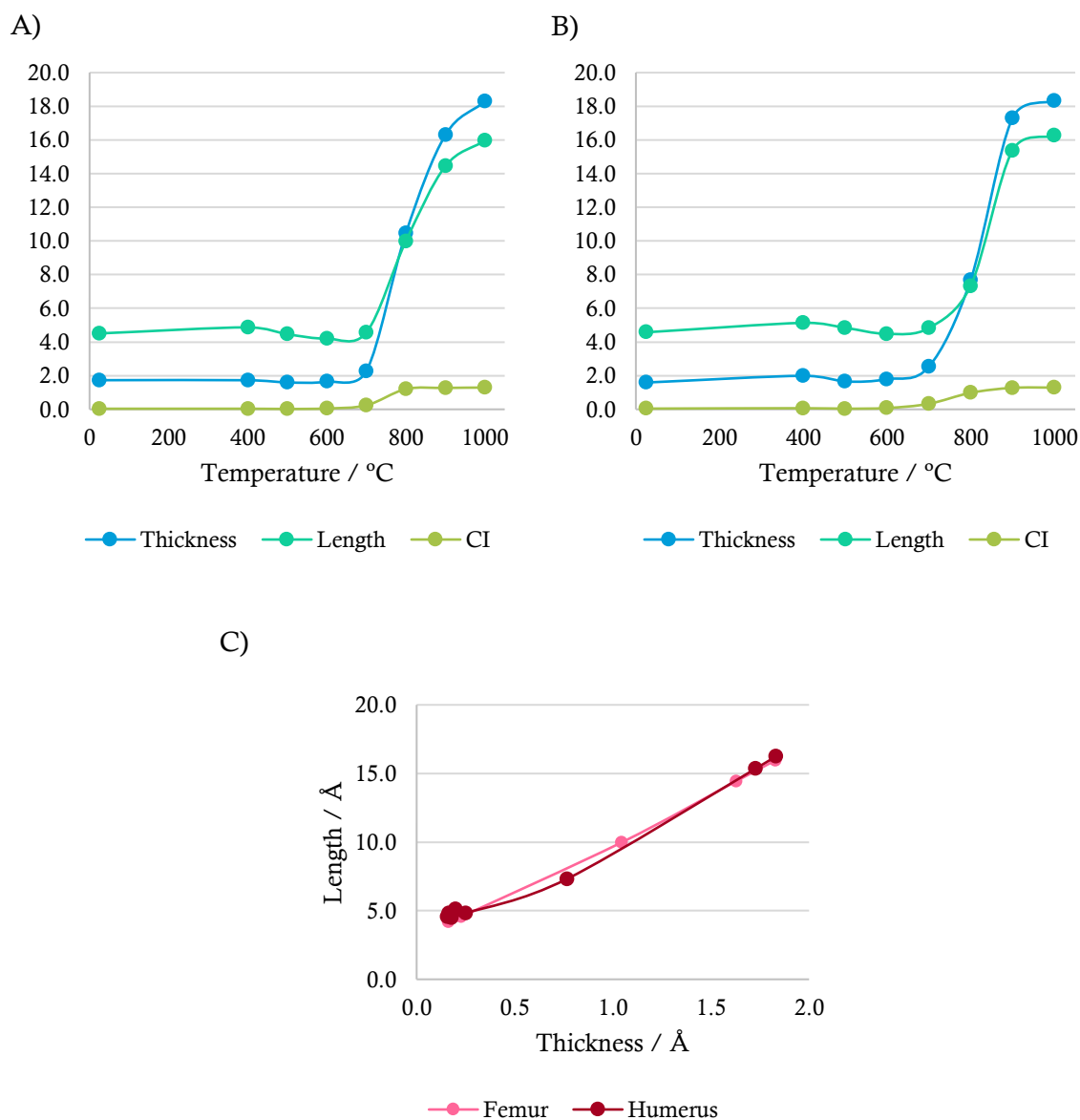


Figure 3.27. Graphical representation of the temperature dependence of CI and crystals thickness and length calculated through XRD data, for femur (A) and humerus (B) samples from skeleton CC_NI_42; (C) Crystals length variations as a function of crystals thickness, in femur and humerus.

Surprisingly, crystal length slightly decreased from 400 to 600 °C in both femur and humerus, contrary to thickness values that remained constant (Figure 3.27 (A) and (B), turquoise curve). This decrease in crystal length is consistent with the observed reduction of the CI ratio calculated through FTIR-ATR data. The mineralisation of collagen is parallel to the orientation of the

collagen fibres, *i.e.* the crystal *c*-axis is parallel to the collagen fibres [146]. As already mentioned, the collagen contracts when the temperature increases probably dragging the inorganic crystals and consequently causing the observed decrease in crystal length.

Crystal dimensions and crystallinity were highly affected by heating above 700 °C (Figure 3.27). CI values increased mostly from 700 to 800 °C, with only a small increment upon exposure to higher temperatures (>800 °C). Length and thickness suffered major changes for temperatures above 700 °C. Thickness increased in femur from 2.270 Å, at 700 °C, to 18.290 Å at 1000 °C (Figure 3.27 (A) and (B), light blue), while length rose from 4.564 to 15.963 Å in the same range of temperatures. Humerus crystal thickness increased from 2.525 to 18.328 Å, and crystal length from 4.824 to 16.260 Å, from 700 to 1000 °C. Comparing crystals thickness and length, the former undergone a larger variation, reflected in big, roundish crystals, and consequently more ordered and less strained crystal lattices. This kind of response to heating was identical for both femur and humerus, as depicted in Figure 3.27 (C).

The shape of the crystals is thought to be related to polymorphic transitions within the mineral phase. According to Ma and Liu [147], long and thin crystals (“belt-shaped”) are more common in monoclinic hydroxyapatite, while round-like crystals are preferentially found in hexagonal hydroxyapatite, suggesting that from unburned to 700 °C burned samples bioapatite is mainly monoclinic, with a transition to hexagonal hydroxyapatite occurring between 700 and 800 °C, as previously observed by Piga *et al.* [61]. Monoclinic polymorphic apatite differs from the hexagonal form in the orientation of the OH⁻ groups within the *unit cell*: in monoclinic apatite they are oriented in the same direction along the same column and in the opposite direction in the next column, while in hexagonal apatite adjacent OH⁻s are oriented in contrary directions. Cell parameters *a*, *b* and *c* are also different for each polymorphic mineral phase: hexagonal hydroxyapatite displays a P6₃/m space group symmetry, with *a*=*b*=9.43 Å, *c*=6.88 Å and $\gamma=120^\circ$, and monoclinic hydroxyapatite has a P 2₁/c space group symmetry, with *a*=9.43, *b*=2*a*, *c*=6.88 and $\gamma=120^\circ$ [147]. These reported results are in complete agreement with the previously discussed analysis through vibrational techniques regarding crystal composition and structure alterations between 700 and 800 °C.

3.3.4.2. Neutron Diffraction

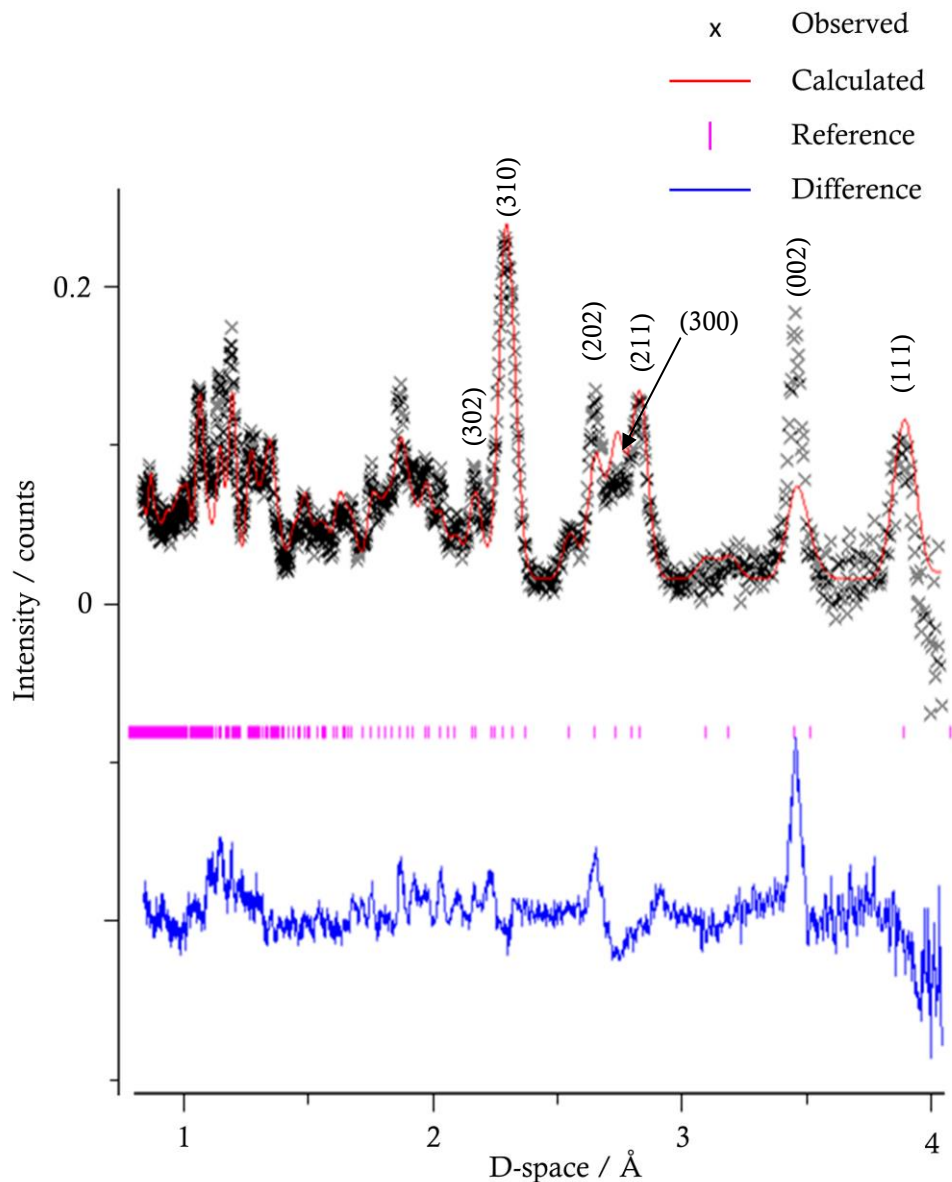
Neutron diffraction experiments were performed for femur samples burned at 400, 700 and 1000 °C. Data was analysed by the Rietveld method, using the software GSAS-EXPGUI. In Figure 3.28, the results are expressed as a function of *d*-space, in Ångstroms, which corresponds to the region also presented in the XRPD results. The Rietveld method consists on the fitting of the observed experimental data (black crosses) with a calculated function (red curve) based on a reference (vertical pink and turquoise dashes). In the present case, the reference was the XRPD

3. Results and Discussion

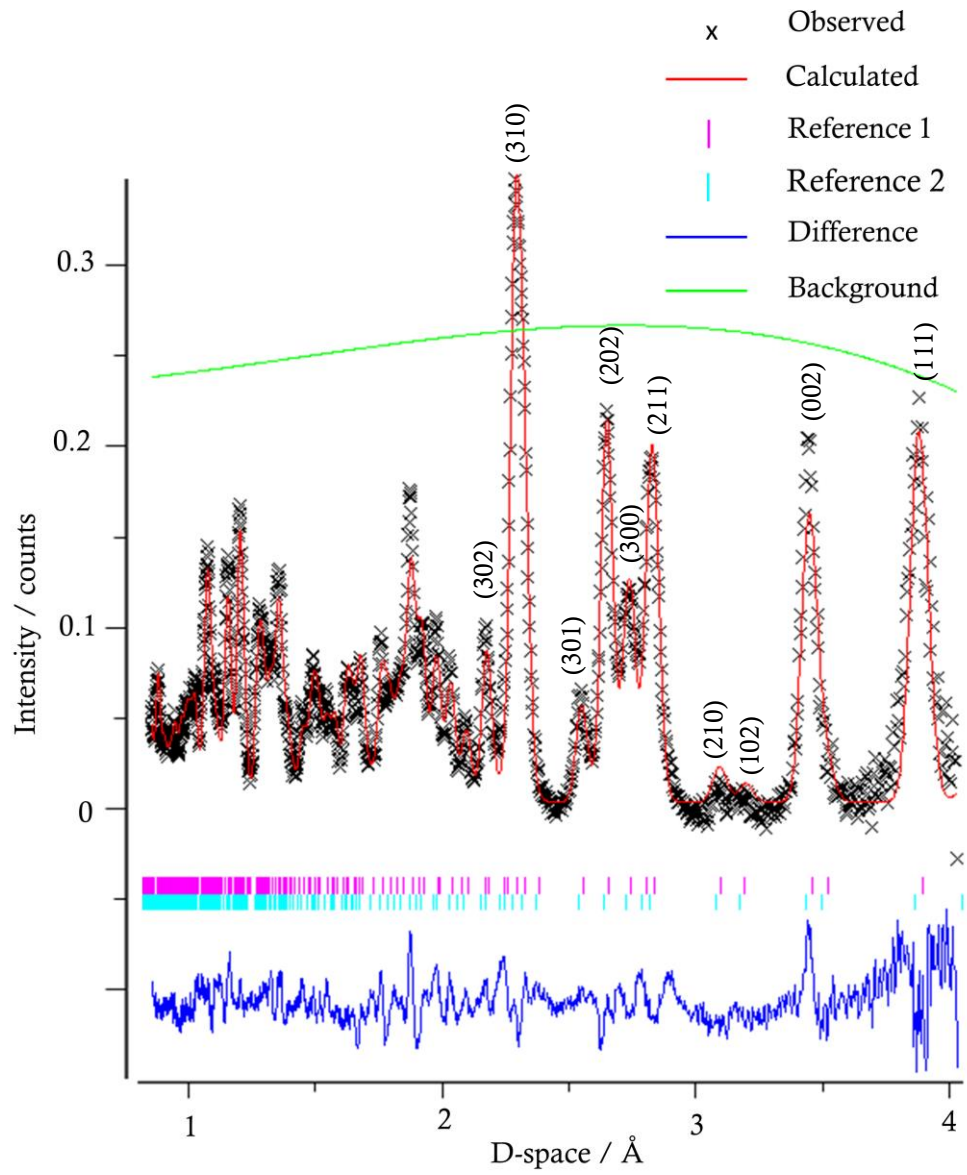
data for carbonated apatite and hydroxyapatite. The better the fitting, the closer to a straight line is the difference between the observed and calculated diffraction patterns.

Figure 3.28 evidenced notable differences between the samples burned at 400 °C (A) and 700 °C (B), and that burned at 1000 °C (C). It were clearly observed, at least, two different mineral phases, as proved by XRPD (Figure 3.26). The observed diffraction patterns obtained for all the analysed samples (Figure 3.28, black crosses) revealed the sharpening of the peaks as temperature increased, peaks also got more intense and more defined, suggesting more ordered lattices and corroborating the previous analysis by vibrational techniques and XRPD.

A)



B)



3. Results and Discussion

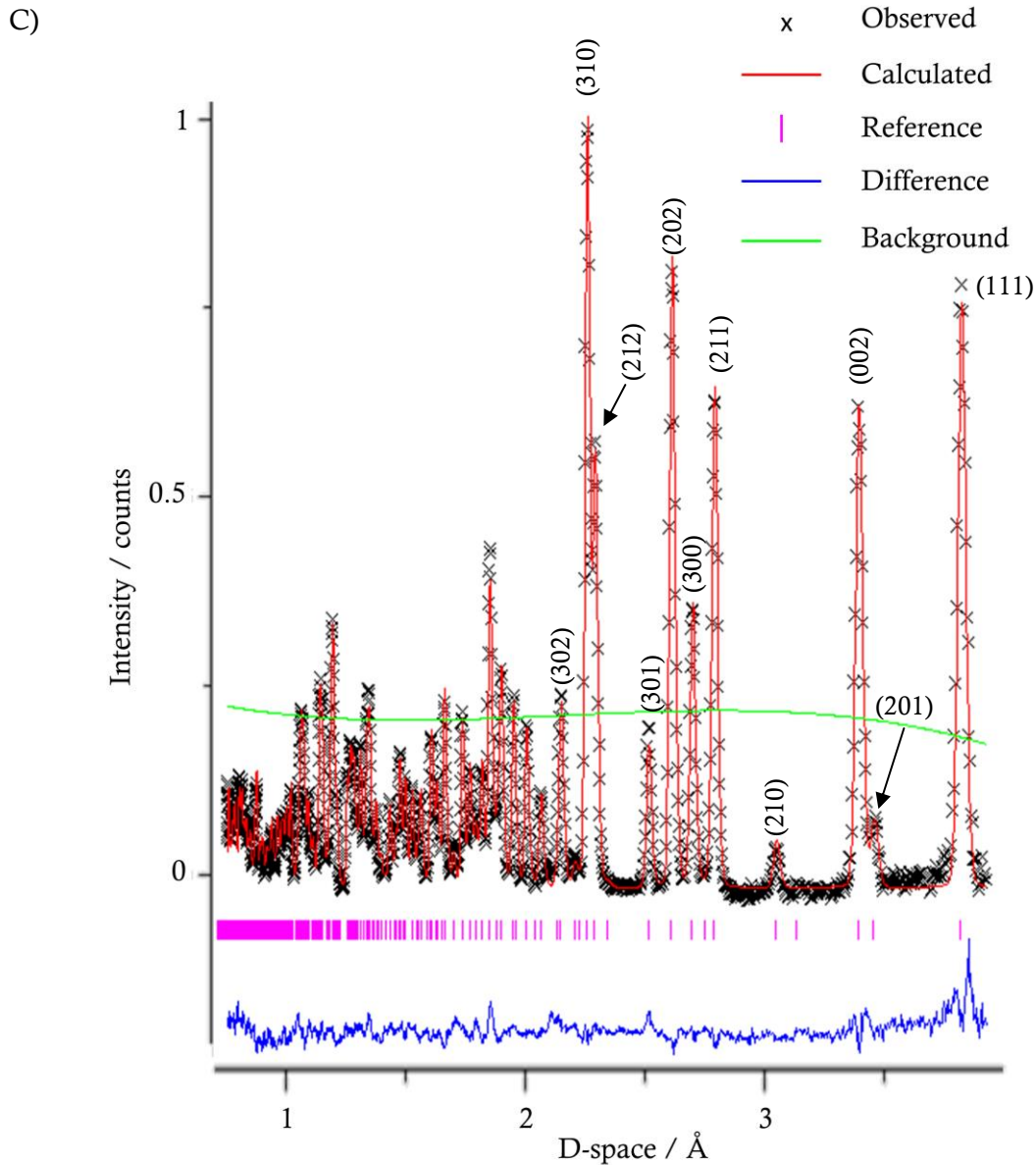


Figure 3.28. Neutron diffractograms, in the 0 – 4 Å range, for femur samples from skeleton CC_NI_42, burned at 400 °C (A), 700 °C (B) and 1000 °C (C).

The (300) diffraction peak, at 2.73 Å, is related to the a -axis. It is suggested that the a -axis is dependent on type A carbonate content, causing peak broadening [125]. In fact, the diffractogram of the 400 °C sample displayed this peak broadened and overlapped with the (202) and (211) peaks at 2.63 and 2.81 Å, respectively. For the sample burned at 700 °C the (300) diffracting peak was perfectly visible, although partially overlapped with the (202) and (211) peaks, which is consistent with the remaining results (higher A carbonates content for samples burned at low temperatures). Type B carbonates are related to crystallite orientation along the c -axis [100], its presence within the lattice is seen to prompt contraction of the a -axis and expansion of the c -axis, with the consequent broadening of the (002) peak.

Similarly to XRPD, the (310) reflects crystal thickness. Analysing (002) and (310) full width at half maximum (FWHM) and intensity values (Figure 3.29 (A) and (B), turquoise and light green), the concomitant peak sharpening and increasing intensity as temperature increases was clearly visible, the biggest alterations occurring above 700 °C, especially in the (310) peak, corroborating XRPD results: long and thin crystals, acquiring rounded shapes at increasing temperatures.

The (111) diffracting peak, at 3.89 Å, was proposed by Benmarouane *et al.* [57] to be related to the crystallinity index. These authors found that 3 days heating at 625 °C did not alter bone's crystallinity (hydroxiapatite being taken as a reference). It was proved that heating does cause an increase in crystallinity. Also, the (111) peak was affected to the same magnitude as the (310) one (Figure 3.28 (A) and (B), light blue), suggesting that its alteration is related to crystal thickness changes as well. However, in the X-ray diffractogram this peak did not show considerable changes, thus being poorly informative.

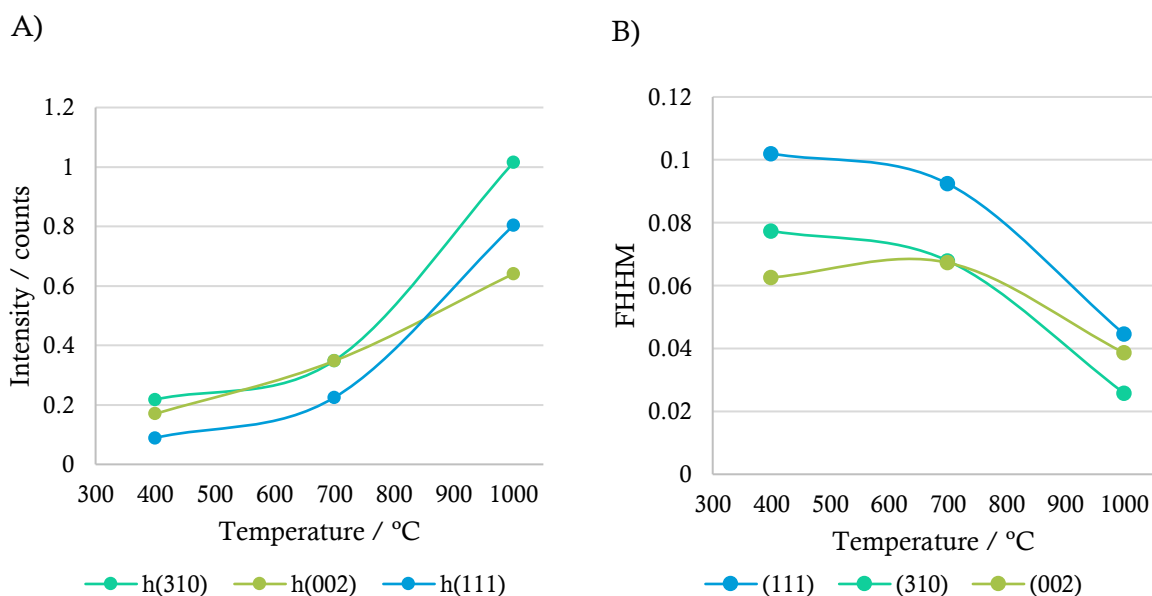


Figure 3.29. Graphical representation of the temperature dependence, observed through neutron diffraction, for: the (002) (light green), (111) and (310) (turquoise) diffracting peaks intensity (A); the (002) (light green), (111) and (310) (turquoise) diffracting peaks FWHM (B).

It is important to refer that the calculated refinement used for the samples burned at 400 and 700 °C encountered serious problems, since the X-ray structure chosen as a reference model was not the right one. In fact, the refinement was calculated using the X-ray reference of hexagonal carbonated apatite with no H atoms, which is inconsistent with the previously discussed results, that does consider H atoms (including neutron diffraction itself). Firstly, no doubts are left as to

3. Results and Discussion

the presence of OH⁻ groups within bioapatite's crystal structure. Secondly, according to the XRPD data, monoclinic apatite was mostly present in unburned and burned samples up to 700 °C.

For the refinement of the sample burned at 700 °C carbonated apatite and hydroxyapatite structure models were applied, since hydroxyapatite signals started to appear as 700 °C. Although both phases (carbonated apatite and hydroxyapatite) are very similar, and overlap significantly, the observed peaks of the 700 °C burned sample were preferentially located at *d*-spacing values relative to carbonated apatite. However, the carbonated apatite reference currently used was not correct (due to the lack of H atoms), rendering the fitting of the refinement incorrect and far from perfect for the sample burned at 700 °C. Besides, there is the possibility of the existence of an intermediate lattice structure, hypothesised in the light of the vibrational and XRPD data presently gathered, probably being necessary one or two more reference phases in order to obtain a perfect fit.

Fitting of the sample burned at 1000 °C was performed using the hexagonal hydroxyapatite structure model. All the peaks of hydroxyapatite fitted perfectly, corroborating the presence of a pure form of hydroxyapatite in bones heated at 1000 °C (or higher temperatures).

It is of utmost importance to note that all the conclusions of this study are, probably, dependent on the burning period. In fact, in this study, the burning experiments were performed during 120 min, being possible that these observed heat-induced alterations at molecular level are different for shorter or longer periods of time exposed to heat. Although, summarising all the submicroscopic heat-induced alterations obtained in this study:

- i) **FTIR-ATR**, through the calculation of several parameters: CI, which decreased up to 600 °C, increasing at higher temperatures, being suitable for estimating the burning temperature for middle range temperatures (600 – 800 °C). C/P, that gradually decreased with increasing temperatures, being a good parameter for samples burned at low temperatures. BPI, which decreased as temperature increases, proved to be redundant with the C/P ratio; however when type B carbonate content calculation is of interest, for high burning temperatures, the BPI ratio is more appropriate. API, shown to be a quite doubtful parameter due to the contribution of the amide II band at low burning temperatures, overestimating this value. OH/P, tested with different vibrational peaks: while OH/P-I is based on the OH⁻ librational band at 630 cm⁻¹, OH/P-II is based on the OH⁻ stretching band, at 3572 cm⁻¹ and OH/P-III relies on the (Ca-OH) stretching frequency. These three ratios were only calculable for samples burned above 700 °C, OH/P-III having great potential for burning temperature estimation between 700 and 1000 °C and also able to yield information on the crystal lattice polymorphic transition. C/C increased with an increase in temperature (contrary to what was concluded based on the remaining parameters), due to the marked decrease of type B carbonates (more noticeable than the identical process for carbonates A).

- ii) **Raman spectroscopy**, ideal for the analysis of samples burned above 800 °C, when fluorescence interference does not occur. Similarly to infrared analysis, Raman supported an increase in crystallinity and a concomitant decrease in type B carbonate content. Using excitation sources with different wavelengths, the magnitude of the calculated alterations was found to be in the same range. Regarding the C/P ratios, it was proved that C/P-II, based on $\nu_2(\text{PO}_4^{3-})$, is more consistent for different types of bone and distinct lasers lines.
- iii) The **CARS** technique, that has great potential for overcoming fluorescence in low temperature burned bones. It is, however, essential to optimise the sample preparation protocol (namely the slicing process), in order to obtain a good enough image.
- iv) **INS spectroscopy**, preferably using different spectrometers with complementary characteristics (TOSCA and MAPS, in this work). These neutron results allowed to assign all vibrational modes of the samples, for the whole temperature range probed, and lead to the identification of crucial biomarkers of heat-induced changes. Additionally, they confirmed the information previously obtained by FTIR-ATR and Raman: intensification and definition of the peaks as temperature increases, reflecting an increase in OH content, as well as different environments within the crystal lattice and more ordered structures, with the biggest alterations taking place above 700 °C.
- v) **X-ray diffraction**, that corroborated variations in the crystal structure between 700 and 800 °C, at polymorphic transition from monoclinic to hexagonal apatite, and an increase in crystal dimensions upon temperature increase.
- vi) **Neutron diffraction**, which allowed to locate hydrogen atoms within bioapatite, at the different burning conditions, and also corroborated XRPD data. Although neutron data contains much more information than conventional X-Ray powder diffraction, further studies are needed in order to correct for the technical issues currently found, with a view to extract all the information contained in the neutron diffractograms of the bone samples.

These observed submicroscopic features can be related to the macroscopic ones. The biggest mass losses observed in burned bone occurred at 400 °C, consistent with the largest losses of organic material, also verified by FTIR-ATR. In both bones, these drops occurred up to 600 °C, being accompanied by a slight decrease in CI and a diminished carbonate content. The decrease in femur diameter was submicroscopically coupled to an increase in crystallinity, associated to a monoclinic-to-hexagonal polymorphic transition (related to OH/P-III parameter), a decrease in carbonate content and also to the highest OH⁻ amount (calculated by OH/P-I and OH/P-II FTIR-ATR parameters, by OH/P Raman ratio and the INS intensity of the OH⁻ stretch band). Between

3. Results and Discussion

800 and 900 °C, these last alterations related with the OH⁻ content also occurred, concomitantly with the biggest decrease in bone length.

In humerus, the macroscopic alterations are less evident than in femur. Only diameter showed more significant changes between 800 and 900 °C, concomitantly with the highest OH⁻ amount (calculated by the OH/P-III FTIR-ATR parameter, the OH/P Raman ratio and the INS OH⁻ stretch peak intensity).

These markedly distinct macroscopic behaviours, when the submicroscopic changes were so similar between bones, are probably related to the fact that bone composition is not the same in the same skeleton: bone composition from proximal to distal region varies due to the metabolic processes of resorption and regeneration over life, resulting in different bone compositions at the moment of death; post-burial diagenetic alterations result in more ordered crystal lattices, beyond the incorporation of some ions and minerals (*e. g.* fluorine and quartz). The extension of these diagenetic changes are obviously dependent on post-burial period, type of soil in contact with the remains and the environmental factors, such as weather and flora. These differences are not completely eliminated by heating, as clearly proved by the INS results. However, the most reliable explanation is that the present study was performed for bone sections, which is not exactly the same as subjecting a whole bone to heat. When an entire bone is burned, the macroscopic parameters are prone to change in a somewhat different way.

4 Conclusions

4. Conclusions

Regarding the enzymatic bone defatting and deproteinisation protocol, it was concluded that, although the need of optimisation of the experimental procedure and the occurrence of some alterations in the crystallinity index related to the decrease in the amount of type B carbonates, these were very slight when compared to hydrazine effect in the bioapatite constitution. This protocol thus retains an enormous potential as an alternative to solvent washing chemical.

The application of neutron scattering techniques in the study of burned bones yielded very valuable information, especially on the samples burned above 600°C. Being the most reliable technique for the estimation of heat-induced alterations in bone, INS cannot, however, become a routine method in forensic science. In turn, this technique is essential for identifying reliable spectral biomarkers, thus supporting the data obtained through infrared and Raman spectroscopies, that can be developed as precious tools for day-to-day use in forensic laboratories.

X-ray diffraction methods, in addition, showed to be crucial for evaluating alterations in the lattice structure as well as in the mineral phases' composition. Further studies applying neutron diffraction to human bones, burned under controlled conditions in a wide temperature range will add to the conventional X-ray diffraction data already gathered, which is expected to help to decode mineral phases transitions as well as the presence of halogen atoms (hypothesized to be the cause of fluorescence often observed in this type of samples).

In order to overcome fluorescence, a useful technique is CARS spectroscopy. This, however, requires very smooth bone slices, which involves a significant improvement of the sample preparation process.

The establishment of new bioanthropological methods should be based on parameters that are consistent for all types of bones, as temperature increases. Based on the present study the parameters that best respected this rule are CI, BPI, C/P, OH-I, OH-II and OH-III, collectable by infrared spectroscopy. Maturity/crystallinity, C/P-II and OH/P, calculable by Raman spectroscopy, as well as CI and crystal's length and thickness obtainable by XRD. Some of these parameters showed to have great potential regarding temperature estimation, namely OH/P-III (FTIR-ATR) and OH/P obtained through Raman (not with a 785 nm exciting radiation). Further studies are still needed to confirm the present conclusions, using more bones from the same skeleton, as well as from different skeletons, exposed to controlled temperatures for different periods of time. The application of these parameters (except C/P) are more appropriate for samples burned above 700 °C, as under this temperature little alterations were found to occur due to the presence of bone's organic matrix that protects the inorganic moiety from heat. Estimation of changes at low temperatures, therefore, must be based on collagen degradation.

4. Conclusions

In conclusion, FTIR-ATR showed to be the most adequate technique for a daily analysis in forensic laboratories. Firstly, since all of them are usually equipped with mid-FTIR apparatus, the analysis is not destructive, requires a very small amount of sample and hardly any sample preparation, the interferences are easily eliminated, the collected results are extremely rich in information on both the organic and inorganic components of bone and the quantitative parameters are calculated through peak's intensity rendering the analysis very easy and fast. Besides, INS results corroborate the results obtained through FTIR-ATR, proving its reliability. Coupling X-ray diffraction to the FTIR-ATR results, the analysis becomes stronger and more complete.

5

References

1. Blau S, Briggs CA (2011) The role of forensic anthropology in Disaster Victim Identification (DVI). *Forensic Sci Int* 205:29–35. doi: 10.1016/j.forsciint.2010.07.038
2. Cattaneo C (2007) Forensic anthropology: developments of a classical discipline in the new millennium. *Forensic Sci Int* 165:185–193. doi: 10.1016/j.forsciint.2006.05.018
3. İşcan MY (2001) Global forensic anthropology in the 21st century. *Forensic Sci Int* 117:1–6. doi: 10.1016/S0379-0738(00)00433-3
4. İşcan MY (2005) Forensic anthropology of sex and body size. *Forensic Sci Int* 147:107–112. doi: 10.1016/j.forsciint.2004.09.069
5. Steyn M, Patriquin ML (2009) Osteometric sex determination from the pelvis-Does population specificity matter? *Forensic Sci Int*. doi: 10.1016/j.forsciint.2009.07.009
6. World Health Organization (2011) Burn Prevention: success stories and lessons learned. http://apps.who.int/iris/bitstream/10665/97938/1/9789241501187_eng.pdf. Accessed 22 Oct 2016
7. Ubelaker DH (2009) The forensic evaluation of burned skeletal remains: A synthesis. *Forensic Sci Int* 183:1–5. doi: 10.1016/j.forsciint.2008.09.019
8. Schwark T, Heinrich A, Preuße-Prange A, Von Wurmb-Schwark N (2011) Reliable genetic identification of burnt human remains. *Forensic Sci Int Genet* 5:393–399. doi: 10.1016/j.fsigen.2010.08.008
9. Andersen L, Juhl M, Solheim T, Borrman H (1995) Odontological identification of fire victims - potentialities and limitations. *Int J Legal Med* 107:229–234. doi: 10.1007/BF01245479
10. Woisetschläger M, Lussi A, Persson A, Jackowski C (2011) Fire victim identification by post-mortem dental CT: Radiologic evaluation of restorative materials after exposure to high temperatures. *Eur J Radiol* 80:432–440. doi: 10.1016/j.ejrad.2010.06.012
11. Thompson TJU (2016) Anthropology: Cremated Bones – Anthropology. *Encycl Forensic Leg Med* 1:177–182. doi: 10.1016/B978-0-12-800034-2.00024-0
12. de Becdelievre C, Thiol S, Santos F, Rottier S (2015) From fire-induced alterations on human bones to the original circumstances of the fire: An integrated approach of human cremains drawn from a Neolithic collective burial. *J Archaeol Sci Reports* 4:210–225. doi: 10.1016/j.jasrep.2015.08.030
13. Gonçalves D, Thompson TJU, Cunha E (2011) Implications of heat-induced changes in bone on the interpretation of funerary behaviour and practice. *J Archaeol Sci* 38:1308–1313. doi: 10.1016/j.jas.2011.01.006
14. Castillo RF, Ubelaker DH, Acosta JAL, de la Fuente GAC (2013) Effects of temperature on bone tissue. Histological study of the changes in the bone matrix. *Forensic Sci Int* 226:33–37. doi: 10.1016/j.forsciint.2012.11.012
15. Thompson TJU (2004) Recent advances in the study of burned bone and their implications

5. References

- for forensic anthropology. *Forensic Sci Int* 146:203–205. doi: 10.1016/j.forsciint.2004.09.063
16. Thompson TJU, Chudek JA (2007) A novel approach to the visualisation of heat-induced structural change in bone. *Sci Justice* 47:99–104. doi: 10.1016/j.scijus.2006.05.002
 17. Brough AL, Morgan B, Rutty GN (2015) The basics of disaster victim identification. *J Forensic Radiol Imaging* 3:29–37. doi: 10.1016/j.jofri.2015.01.002
 18. Zgonjanin D, Petkovi S, Maletin M, et al (2015) Case report : DNA identification of burned skeletal remains. *Forensic Sci Int Genet Suppl Ser* 5:446–448. doi: 10.1016/j.fsigss.2015.09.176
 19. Harbeck M, Schleuder R, Schneider J, et al (2011) Research potential and limitations of trace analyses of cremated remains. *Forensic Sci Int* 204:191–200. doi: 10.1016/j.forsciint.2010.06.004
 20. Pérez L, Sanchis A, Hernández CM, et al (2017) Hearths and bones: An experimental study to explore temporality in archaeological contexts based on taphonomical changes in burnt bones. *J Archaeol Sci Reports* 11:287–309. doi: <http://dx.doi.org/10.1016/j.jasrep.2016.11.036>
 21. Gonçalves D, Cunha E, Thompson TJU (2014) Estimation of the pre-burning condition of human remains in forensic contexts. *Int J Legal Med* 129:1137–1143. doi: 10.1007/s00414-014-1027-8
 22. Keough N, L'Abbé EN, Steyn M, Pretorius S (2015) Assessment of skeletal changes after post-mortem exposure to fire as an indicator of decomposition stage. *Forensic Sci Int* 246:17–24. doi: 10.1016/j.forsciint.2014.10.042
 23. Vassalo AR, Cunha E, de Carvalho LAEB, Gonçalves D (2016) Rather yield than break: assessing the influence of human bone collagen content on heat-induced warping through vibrational spectroscopy. *Int J Legal Med* 130:1647–1656. doi: 10.1007/s00414-016-1400-x
 24. Etok SE, Valsami-Jones E, Wess TJ, et al (2007) Structural and chemical changes of thermally treated bone apatite. *J Mater Sci* 42:9807–9816. doi: 10.1007/s10853-007-1993-z
 25. Snoeck C, Lee-Thorp JA, Schulting RJ (2014) From bone to ash: Compositional and structural changes in burned modern and archaeological bone. *Palaeogeogr Palaeoclimatol Palaeoecol* 416:55–68. doi: 10.1016/j.palaeo.2014.08.002
 26. Munro LE, Longstaffe FJ, White CD (2007) Burning and boiling of modern deer bone: Effects on crystallinity and oxygen isotope composition of bioapatite phosphate. *Palaeogeogr Palaeoclimatol Palaeoecol* 249:90–102. doi: 10.1016/j.palaeo.2007.01.011
 27. Shipman P, Foster G, Schoeninger M (1984) Burnt bones and teeth: an experimental study of color, morphology, crystal structure and shrinkage. *J Archaeol Sci* 11:307–325. doi: 10.1016/0305-4403(84)90013-X
 28. Ellingham STD, Thompson TJU, Islam M (2016) The Effect of Soft Tissue on Temperature

- Estimation from Burnt Bone Using Fourier Transform Infrared Spectroscopy. *J Forensic Sci* 61:153–159. doi: 10.1111/1556-4029.12855
29. Lee CL, Einhorn TA (2001) The Bone Organ System - Form and Function. In: Marcus R, Feldman D, Kelsey J (eds) *Osteoporosis, Second Edi*. Academic Press, pp 3–20
 30. Boskey JA, Gokhale AL, Robey PG (2001) The Biochemistry of Bone. In: Marcus R, Feldman D, Kelsey J (eds) *Osteoporosis, Second Edi*. Academic Press, pp 107–188
 31. Thompson TJU (2015) The Analysis of Heat-Induced Crystallinity Change in Bone. In: Schmidt CW, Symes SA (eds) *Anal. Burn. Hum. Remain.* pp 323–337
 32. Wang XY, Zuo Y, Huang D, et al (2010) Comparative study on inorganic composition and crystallographic properties of cortical and cancellous bone. *Biomed Environ Sci* 23:473–480. doi: 10.1016/S0895-3988(11)60010-X
 33. Clarke B (2008) Normal bone anatomy and physiology. *Clin J Am Soc Nephrol* 3:131–139. doi: 10.2215/CJN.04151206
 34. LeGeros RZ, Trautz OR, Klein E, LeGeros JP (1969) Two types of carbonate substitution in the apatite structure. *Experientia* 25:5–7. doi: 10.1007/BF01903856
 35. Rey C, Collins B, Goehl T, et al (1989) The carbonate environment in bone mineral: A resolution-enhanced fourier transform infrared spectroscopy study. *Calcif Tissue Int* 45:157–164. doi: 10.1007/BF02556059
 36. Astala R, Stott MJ (2005) First principles investigation of mineral component of bone: CO₃ substitutions in hydroxyapatite. *Chem Mater* 17:4125–4133. doi: 10.1021/cm050523b
 37. Wopenka B, Pasteris JD (2005) A mineralogical perspective on the apatite in bone. *Mater Sci Eng C* 25:131–143. doi: 10.1016/j.msec.2005.01.008
 38. Person A, Bocherens H, Saliège J-F, et al (1995) Early Diagenetic Evolution of Bone Phosphate : An X-ray Diffractometry Analysis. *J Archaeol Sci* 22:211–221. doi: <http://dx.doi.org/10.1006/jasc.1995.0023>
 39. Bacon GE (1990) The dependence of human bone texture on life style. *Proc R Soc London* 240:363–370. doi: 10.1098/rspb.1990.0042
 40. Gómez-Morales J, Iafisco M, Delgado-López JM, et al (2013) Progress on the preparation of nanocrystalline apatites and surface characterization: Overview of fundamental and applied aspects. *Prog Cryst Growth Charact Mater* 59:1–46. doi: 10.1016/j.pcrysgrow.2012.11.001
 41. Beasley MM, Bartelink EJ, Taylor L, Miller RM (2014) Comparison of transmission FTIR, ATR, and DRIFT spectra: Implications for assessment of bone bioapatite diagenesis. *J Archaeol Sci* 46:16–22. doi: 10.1016/j.jas.2014.03.008
 42. Trueman CN, Privat K, Field J (2008) Why do crystallinity values fail to predict the extent of diagenetic alteration of bone mineral? *Palaeogeogr Palaeoclimatol Palaeoecol* 266:160–167. doi: 10.1016/j.palaeo.2008.03.038

5. References

43. Trueman CNG, Behrensmeyer AK, Tuross N, Weiner S (2004) Mineralogical and compositional changes in bones exposed on soil surfaces in Amboseli National Park, Kenya: Diagenetic mechanisms and the role of sediment pore fluids. *J Archaeol Sci* 31:721–739. doi: 10.1016/j.jas.2003.11.003
44. Marques MPM, Gonçalves D, Amarante AIC, et al (2016) Osteometrics in burned human skeletal remains by neutron and optical vibrational spectroscopy. *RSC Adv* 6:68638–68641. doi: 10.1039/C6RA13564A
45. Thompson TJU, Islam M, Bonniere M (2013) A new statistical approach for determining the crystallinity of heat-altered bone mineral from FTIR spectra. *J Archaeol Sci* 40:416–422. doi: 10.1016/j.jas.2012.07.008
46. Shahack-Gross R, Bar-Yosef O, Weiner S (1997) Black-Coloured Bones in Hayonim Cave, Israel: Differentiating Between Burning and Oxide Staining. *J Archaeol Sci* 24:439–446. doi: 10.1006/jasc.1996.0128
47. Nicholson RA (1993) A Morphological Investigation of Burnt Animal Bone and an Evaluation of its Utility in Archaeology. *J Archaeol Sci* 20:411–428. doi: 10.1006/jasc.1993.1025
48. Ellingham STD, Thompson TJU, Islam M, Taylor G (2015) Estimating temperature exposure of burnt bone - A methodological review. *Sci Justice* 55:181–188. doi: 10.1016/j.scijus.2014.12.002
49. Crippin JB (2013) Explosions. In: Siegel JA, Saukko PJ (eds) *Encycl. Forensic Sci.*, Second Edi. Elsevier, pp 104–108
50. Lebon M, Reiche I, Bahain JJ, et al (2010) New parameters for the characterization of diagenetic alterations and heat-induced changes of fossil bone mineral using Fourier transform infrared spectrometry. *J Archaeol Sci* 37:2265–2276. doi: 10.1016/j.jas.2010.03.024
51. Pucéat E, Reynard B, Lécuyer C (2004) Can crystallinity be used to determine the degree of chemical alteration of biogenic apatites? *Chem Geol* 205:83–97. doi: 10.1016/j.chemgeo.2003.12.014
52. Thompson TJU, Islam M, Piduru K, Marcel A (2011) An investigation into the internal and external variables acting on crystallinity index using Fourier Transform Infrared Spectroscopy on unaltered and burned bone. *Palaeogeogr Palaeoclimatol Palaeoecol* 299:168–174. doi: 10.1016/j.palaeo.2010.10.044
53. Thomas DB, McGoverin CM, Fordyce RE, et al (2011) Raman spectroscopy of fossil bioapatite - A proxy for diagenetic alteration of the oxygen isotope composition. *Palaeogeogr Palaeoclimatol Palaeoecol* 310:62–70. doi: 10.1016/j.palaeo.2011.06.016
54. Gamsjaeger S, Hofstetter B, Fratzl-Zelman N, et al (2014) Pediatric reference Raman data for material characteristics of iliac trabecular bone. *Bone* 69:89–97. doi:

- 10.1016/j.bone.2014.09.012
55. France CAM, Thomas DB, Doney CR, Madden O (2014) FT-Raman spectroscopy as a method for screening collagen diagenesis in bone. *J Archaeol Sci* 42:346–355. doi: 10.1016/j.jas.2013.11.020
 56. Taylor MG, Parker SF, Simkiss K, Mitchell PCH (2001) Bone mineral: evidence for hydroxy groups by inelastic neutron scattering. *Phys Chem Chem Phys* 3:1514–1517. doi: 10.1039/b005666i
 57. Benmarouane A, Hansen T, Lodini A (2004) Heat treatment of bovine bone preceding spatially resolved texture investigation by neutron diffraction. *Phys B Condens Matter* 350:611–614. doi: 10.1016/j.physb.2004.03.163
 58. Wilson RM, Elliott JC, Dowker SEP, Smith RI (2004) Rietveld structure refinement of precipitated carbonate apatite using neutron diffraction data. *Biomaterials* 25:2205–2213. doi: 10.1016/j.biomaterials.2003.08.057
 59. Bacon GE, Bacon PJ, Griffiths RK (1977) The study of bones by neutron diffraction. *J Appl Crystallogr* 10:124–126. doi: 10.1107/S002188987701303X
 60. Rogers K, Beckett S, Kuhn S, et al (2010) Contrasting the crystallinity indicators of heated and diagenetically altered bone mineral. *Palaeogeogr Palaeoclimatol Palaeoecol* 296:125–129. doi: 10.1016/j.palaeo.2010.06.021
 61. Piga G, Thompson TJU, Malgosa A, Enzo S (2009) The Potential of X-Ray Diffraction in the Analysis of Burned Remains from Forensic Contexts. *J Forensic Sci* 54:534–539. doi: 10.1111/j.1556-4029.2009.01037.x
 62. Rogers KD, Daniels P (2002) An X-ray diffraction study of the effects of heat treatment on bone mineral microstructure. *Biomaterials* 23:2577–2585. doi: 10.1016/S0142-9612(01)00395-7
 63. Tu A (1982) *Raman Spectroscopy in Biology Principles and applications*. John Wiley & Sons, Inc.
 64. Stuart B (2005) *Infrared Spectroscopy*. In: Kirk-Othmer *Encycl. Chem. Technol.* John Wiley & Sons, Inc., pp 1–20
 65. Griffiths PR (2006) *Introduction to Vibrational Spectroscopy*. In: *Handb. Vib. Spectrosc.* John Wiley & Sons, Ltd, pp 33–43
 66. Coates J (2006) *Interpretation of Infrared Spectra, A Practical Approach*. In: Meyers RA (ed) *Encycl. Anal. Chem.* John Wiley & Sons, Ltd, pp 1–23
 67. Stuart B (1997) *Biological Applications of Infrared Spectroscopy*. John Wiley & Sons, Inc.
 68. Shurvell HF (2006) *Spectra- Structure Correlations in the Mid- and Far-Infrared*. In: Chalmers JM (ed) *Handb. Vib. Spectrosc.* John Wiley & Sons, Ltd, pp 1783–1816
 69. Thompson TJU, Gauthier M, Islam M (2009) The application of a new method of Fourier Transform Infrared Spectroscopy to the analysis of burned bone. *J Archaeol Sci* 36:910–

5. References

914. doi: 10.1016/j.jas.2008.11.013
70. Surovell TA, Stiner MC (2001) Standardizing Infra-red Measures of Bone Mineral Crystallinity: an Experimental Approach. *J Archaeol Sci* 28:633–642. doi: 10.1006/jasc.2000.0633
71. Khoshhesab ZM (2012) Reflectance IR Spectroscopy. In: Theophanides T (ed) *Infrared Spectrosc. - Mater. Sci. Eng. Technol. InTech*, pp 233–244
72. Stathopoulou ET, Psycharis V, Chryssikos GD, et al (2008) Bone diagenesis: New data from infrared spectroscopy and X-ray diffraction. *Palaeogeogr Palaeoclimatol Palaeoecol* 266:168–174. doi: 10.1016/j.palaeo.2008.03.022
73. Gadolnik J (2002) ATR-FTIR Spectroscopy: Its Advantages and Limitations. *Acta Chim Slov* 49:631–642.
74. Bunaciu AA, Aboul-Enein HY, Fleschin Ş (2015) Vibrational Spectroscopy in Clinical Analysis. *Appl Spectrosc Rev* 50:176–191. doi: 10.1080/05704928.2014.955582
75. Delhaye M, Dhamelinourt P (1975) Raman microprobe and microscope with laser excitation. *J Raman Spectrosc* 3:33–43. doi: 10.1002/jrs.1250030105
76. Golcuk K, Mandair GS, Callender AF, et al (2006) Is photobleaching necessary for Raman imaging of bone tissue using a green laser? *Biochim Biophys Acta* 1758:868–873. doi: 10.1016/j.bbamem.2006.02.022
77. Maggiano C, Dupras T, Schultz M, Biggerstaff J (2006) Spectral and photobleaching analysis using confocal laser scanning microscopy: a comparison of modern and archaeological bone fluorescence. *Mol Cell Probes* 20:154–162. doi: 10.1016/j.mcp.2005.11.009
78. Anastassiades CP, Wilson BC, Song L-MWK (2009) Fluorescence and Raman Spectroscopy. *Gastrointest Endosc Clin N Am* 19:221–231. doi: 10.1016/j.giec.2009.02.009
79. Shea DA, Morris MD (2002) Bone Tissue Fluorescence Reduction for Visible Laser Raman Spectroscopy. *Appl Spectrosc* 56:182–186. doi: 10.1366/0003702021954647
80. Pestle WJ, Ahmad F, Vesper BJ, et al (2014) Ancient bone collagen assessment by hand-held vibrational spectroscopy. *J Archaeol Sci* 42:381–389. doi: 10.1016/j.jas.2013.11.014
81. Druet SAJ, Taran J-PE (1981) CARS spectroscopy. *Prog Quantum Electron* 7:1–72. doi: 10.1016/0079-6727(81)90002-1
82. Parekh SH, Lee YJ, Aamer KA, Cicerone MT (2010) Label-Free Cellular Imaging by Broadband Coherent Anti-Stokes Raman Scattering Microscopy. *Biophys J* 99:2695–2704. doi: 10.1016/j.bpj.2010.08.009
83. Krafft C, Dietzek B, Popp J (2009) Raman and CARS microspectroscopy of cells and tissues. *Analyst* 134:1046–1057. doi: 10.1039/b822354h
84. Pynn R (2009) Neutron Scattering - A Non-destructive Microscope for seeing Inside Matter. In: Liang L, Rinaldi R, Schober H (eds) *Neutron Appl. Earth, Energy Environ. Sci.* Springer

- US, pp 1–28
85. Mitchell P, Parker S, Ramirez-Cuesta A, Tomkinson J (2005) *Vibrational Spectroscopy with Neutrons*. World Scientific Publishing Co. Pte. Ltd.
 86. Parker SF (2006) Inelastic Neutron Scattering Spectroscopy. In: Chalmers JM (ed) *Handb. Vib. Spectrosc.* John Wiley & Sons, Ltd, pp 837–852
 87. Taylor MG, Parker SF, Mitchell PCH (2003) A study by high energy transfer inelastic neutron scattering spectroscopy of the mineral fraction of ox femur bone. *J Mol Struct* 651–653:123–126. doi: 10.1016/S0022-2860(03)00102-9
 88. Hudson BS (2001) Inelastic Neutron Scattering: A Tool in Molecular Vibrational Spectroscopy and a Test of ab Initio Methods. *J Phys Chem A* 105:3949–3960. doi: 10.1021/jp004429o
 89. Hudson BS (2006) Vibrational spectroscopy using inelastic neutron scattering: Overview and outlook. *Vib Spectrosc* 42:25–32. doi: 10.1016/j.vibspec.2006.04.014
 90. Lefmann K (2007) *Neutron Scattering: Theory, Instrumentation, and Simulation*. 9–44.
 91. Loong C-K, Rey C, Kuhn LT, et al (2000) Evidence of hydroxyl-ion deficiency in bone apatites: an inelastic neutron-scattering study. *Bone* 26:599–602. doi: 10.1016/S8756-3282(00)00273-8
 92. Morris MD, Finney WF (2004) Recent developments in Raman and infrared spectroscopy and imaging of bone tissue. *Spectroscopy* 18:155–159. doi: 10.1155/2004/765753
 93. Morris MD, Mandair GS (2011) Raman Assessment of Bone Quality. *Clin Orthop Relat Res* 469:2160–2169. doi: 10.1007/s11999-010-1692-y
 94. Zazzo A, Lebon M, Chiotti L, et al (2013) Can we Use Calcined Bones for ¹⁴C Dating the Paleolithic? *Radiocarbon* 55:1409–1421. doi: 10.1017/S0033822200048347
 95. Carden A, Morris MD (2000) Application of vibrational spectroscopy to the study of mineralized tissues (review). *J Biomed Opt* 5:259. doi: 10.1117/1.429994
 96. Sponheimer M, Lee-Thorp J a (1999) Alteration of Enamel Carbonate Environments during Fossilization. *J Archaeol Sci* 26:143–150. doi: 10.1006/jasc.1998.0293
 97. Patonai Z, Maasz G, Avar P, et al (2013) Novel dating method to distinguish between forensic and archeological human skeletal remains by bone mineralization indexes. *Int J Legal Med* 127:529–533. doi: 10.1007/s00414-012-0785-4
 98. Penel G, Leroy G, Rey C, Bres E (1998) MicroRaman Spectral Study of the PO₄ and CO₃ Vibrational Modes in Synthetic and Biological Apatites. *Calcif Tissue Int* 63:475–481. doi: 10.1007/s002239900561
 99. Wright LE, Schwarcz HP (1996) Infrared and Isotopic Evidence for Diagenesis of Bone Apatite at Dos Pilas, Guatemala: Palaeodietary Implications. *J Archaeol Sci* 23:933–944. doi: 10.1006/jasc.1996.0087
 100. Bazin D, Chappard C, Combes C, et al (2009) Diffraction techniques and vibrational

5. References

- spectroscopy opportunities to characterise bones. *Osteoporos Int* 20:1065–1075. doi: 10.1007/s00198-009-0868-3
101. Shemesh A (1990) Crystallinity and diagenesis of sedimentary apatites. *Geochim Cosmochim Acta* 54:2433–2438. doi: 10.1016/0016-7037(90)90230-I
 102. Termine JD, Posner AS (1966) Infrared Analysis of Rat Bone: Age Dependency of Amorphous and Crystalline Mineral Fractions. *Science* (80-) 153:1523–1525. doi: 10.1126/science.153.3743.1523
 103. Piga G, Gonçalves D, Thompson TJU, et al (2016) Understanding the Crystallinity Indices Behavior of Burned Bones and Teeth by ATR-IR and XRD in the Presence of Bioapatite Mixed with Other Phosphate and Carbonate Phases. *Int J Spectrosc* 2016:1–9. doi: 10.1155/2016/4810149
 104. Elliott JC (1994) Structure and Chemistry of the Apatites and Other Calcium Orthophosphates. In: *Stud. Inorg. Chem.* 18. Elsevier B.V., pp 1–389
 105. Iqbal Z, Tomaselli VP, Fahrenfeld O, et al (1977) Polarized Raman scattering and low frequency infrared study of hydroxyapatite. *J Phys Chem Solids* 38:923–927. doi: 10.1016/0022-3697(77)90132-9
 106. de Aza PN, Guitián F, Santos C, et al (1997) Vibrational Properties of Calcium Phosphate Compounds. 2. Comparison between Hydroxyapatite and β -Tricalcium Phosphate. *Chem Mater* 9:916–922. doi: 10.1021/cm9604266
 107. Corno M, Busco C, Civalleri B, Ugliengo P (2006) Periodic ab initio study of structural and vibrational features of hexagonal hydroxyapatite $\text{Ca}_{10}(\text{PO}_4)_6(\text{OH})_2$. *Phys Chem Chem Phys* 8:2464–2472. doi: 10.1039/b602419j
 108. Cullity BD (1978) *Elements of X-Ray Diffraction*, Second edi. Addison-Wesley Publishing Company, Inc
 109. Bacon GE (1966) *X-ray and neutron diffraction*, First edit. Pergamon Press Ltd.
 110. Azaroff L V., Buerger MJ (1958) *The Powder Method in X-Ray Crystallography*. McGraw-Hill Book Company, Inc.
 111. Shapiro IM (1970) The phospholipids of mineralized tissues. *Calcif Tissue Res* 5:21–29. doi: 10.1007/BF02017530
 112. Termine JD, Posner AS (1967) Amorphous/crystalline interrelationships in bone mineral. *Calcif Tissue Res* 1:8–23. doi: 10.1007/BF02008070
 113. Kolosowski KP, Sodhi RNS, Kishen A, Basrani BR (2015) Qualitative time-of-flight secondary ion mass spectrometry analysis of root dentin irrigated with sodium hypochlorite, EDTA, or chlorhexidine. *J Endod* 41:1672–1677. doi: 10.1016/j.joen.2015.06.010
 114. Hamed E, Novitskaya E, Li J, et al (2012) Elastic moduli of untreated, demineralized and deproteinized cortical bone: Validation of a theoretical model of bone as an interpenetrating composite material. *Acta Biomater* 8:1080–1092. doi: 10.1016/j.actbio.2011.11.010

115. Uklejewski R, Winiecki M, Musielak G, Tokł owicz R (2015) Effectiveness of various deproteinization processes of bovine cancellous bone evaluated via mechano-biostructural properties of produced osteoconductive biomaterials. *Biotechnol Bioprocess Eng* 20:259–266. doi: 10.1007/s12257-013-0510-2
116. Termine JD, Eanes ED, Greenfield DJ, et al (1973) Hydrazine-deproteinated bone mineral. *Calcif Tissue Res* 12:73–90. doi: 10.1007/BF02013723
117. Bacon GE, Bacon PJ, Griffiths RK (1979) The orientation of apatite crystals in bone. *J Appl Crystallogr* 12:99–103. doi: 10.1107/S0021889879011857
118. Bertazzo S, Bertran CA (2008) Effect of hydrazine deproteination on bone mineral phase: A critical view. *J Inorg Biochem* 102:137–145. doi: 10.1016/j.jinorgbio.2007.07.031
119. Karampas IA, Orkoula MG, Kontoyannis CG (2012) Effect of hydrazine based deproteination protocol on bone mineral crystal structure. *J Mater Sci Mater Med* 23:1139–1148. doi: 10.1007/s10856-012-4593-7
120. Bou-Gharios G, de Crombrughe B (2008) Type I Collagen Structure, Synthesis, and Regulation. In: *Princ. Bone Biol.*, Third edit. Academic Press, Inc., pp 285–318
121. Zioupos P, Currey JD, Hamer AJ (1999) The role of collagen in the declining mechanical properties of aging human cortical bone. *J Biomed Mater Res* 45:108–116.
122. Zheng X, Pan H, Wang Z, Chen H (2011) Real-time enzymatic degradation of human dentin collagen fibrils exposed to exogenous collagenase: an AFM study in situ. *J Microsc* 241:162–170. doi: 10.1111/j.1365-2818.2010.03412.x
123. Liu Y, Wang Y (2013) Proanthocyanidins' efficacy in stabilizing dentin collagen against enzymatic degradation: MALDI-TOF and FTIR analyses. *J Dent* 41:535–542. doi: 10.1016/j.jdent.2013.03.007
124. Zhang N, Zhou M, Zhang Y, et al (2014) Porcine bone grafts defatted by lipase: efficacy of defatting and assessment of cytocompatibility. *Cell Tissue Bank* 15:357–367. doi: 10.1007/s10561-013-9391-z
125. Pieters IY, De Maeyer EAP, Verbeeck RMH (1998) Influence of Na⁺ on the Stoichiometry of Carbonated Hydroxyapatite Obtained by the Hydrolysis of Octacalcium Phosphate. *Inorg Chem* 37:6392–6395. doi: 10.1021/ic9802810
126. ISIS Facility NEUTROM DIFFRACTION - GEM. <http://www.isis.stfc.ac.uk/instruments/gem/>. Accessed 20 Aug 2017
127. ISIS Facility INS - MAPS. <http://www.isis.stfc.ac.uk/instruments/maps/>. Accessed 20 Aug 2017
128. ISIS Facility INS - TOSCA. <http://www.isis.stfc.ac.uk/instruments/tosca/>. Accessed 20 Aug 2017
129. Ramirez-Cuesta AJ (2004) aCLIMAX 4.0.1. The new version of the software for analyzing and interpreting INS spectra. *Comput Phys Commun* 157:226–238.

5. References

130. Toby BH (2001) EXPGUI, a graphical user interface for GSAS. *J Appl Crystallogr* 34:210–213.
131. Larson AC, Von Dreele RB (1994) General Structure Analysis System (GSAS). Los Alamos Lab Rep 86–748.
132. Arnold O, Bilheux JC, Borreguero JM, et al (2014) Mantid—Data analysis and visualization package for neutron scattering and μ SR experiments. *Nucl Instruments Methods Phys Res Sect A Accel Spectrometers, Detect Assoc Equip* 764:156–166. doi: 10.1016/j.nima.2014.07.029
133. TAIL-UC D8 Advance X-ray powder diffractometer. <http://cfisuc.fis.uc.pt/equipment.php?oid=79876>. Accessed 20 Aug 2017
134. Weiner S, Bar-Yosef O (1990) States of preservation of bones from prehistoric sites in the Near East: A survey. *J Archaeol Sci* 17:187–196. doi: 10.1016/0305-4403(90)90058-D
135. Gamsjaeger S, Masic A, Roschger P, et al (2010) Cortical bone composition and orientation as a function of animal and tissue age in mice by Raman spectroscopy. *Bone* 47:392–399. doi: 10.1016/j.bone.2010.04.608
136. Farlay D, Panczer G, Rey C, et al (2010) Mineral maturity and crystallinity index are distinct characteristics of bone mineral. *J Bone Miner Metab* 28:433–445. doi: 10.1007/s00774-009-0146-7
137. Paschalis EP, DiCarlo E, Betts F, et al (1996) FTIR microspectroscopic analysis of human osteonal bone. *Calcif Tissue Int* 59:480–7.
138. Rey C, Shimizu M, Collins B, Glimcher MJ (1991) Resolution-enhanced fourier transform infrared spectroscopy study of the environment of phosphate ion in the early deposits of a solid phase of calcium phosphate in bone and enamel and their evolution with age: 2. Investigations in the $\nu_3\text{PO}_4$ domain. *Calcif Tissue Int* 49:383–388. doi: 10.1007/BF02555847
139. McCreadie BR, Morris MD, Chen T, et al (2006) Bone tissue compositional differences in women with and without osteoporotic fracture. *Bone* 39:1190–1195. doi: 10.1016/j.bone.2006.06.008
140. Tai K, Dao M, Suresh S, et al (2007) Nanoscale heterogeneity promotes energy dissipation in bone. *Nat Mater* 6:454–462. doi: 10.1038/nmat1911
141. Akkus O, Adar F, Schaffler MB (2004) Age-related changes in physicochemical properties of mineral crystals are related to impaired mechanical function of cortical bone. *Bone* 34:443–453. doi: 10.1016/j.bone.2003.11.003
142. Holcomb DW, Young RA (1980) Thermal decomposition of human tooth enamel. *Calcif Tissue Int* 31:189–201. doi: 10.1007/BF02407181
143. Bachman CH, Ellis EH (1965) Fluorescence of Bone. *Nature* 206:1328–1331. doi: 10.1038/2061328a0

144. Kazanci M, Roschger P, Paschalis EP, et al (2006) Bone osteonal tissues by Raman spectral mapping: Orientation–composition. *J Struct Biol* 156:489–496. doi: 10.1016/j.jsb.2006.06.011
145. Reyes-Gasga J, Martínez-Piñeiro EL, Rodríguez-Álvarez G, et al (2013) XRD and FTIR crystallinity indices in sound human tooth enamel and synthetic hydroxyapatite. *Mater Sci Eng C* 33:4568–4574. doi: 10.1016/j.msec.2013.07.014
146. Danilchenko SN, Moseke C, Sukhodub LF, Sulkio-Cleff B (2004) X-ray diffraction studies of bone apatite under acid demineralization. *Cryst Res Technol* 39:71–77. doi: 10.1002/crat.200310151
147. Ma G, Liu XY (2009) Hydroxyapatite: Hexagonal or Monoclinic? *Cryst Growth Des* 9:2991–2994. doi: 10.1021/cg900156w

Abbreviations

API - Type A Carbonate Amount

BPI – Type B Carbonate Amount

CARS - Coherent Anti-Stokes Raman Scattering

CI – Crystallinity index

Enz – Enzymatically-treated

FTIR - Fourier Transform infrared spectroscopy in attenuated total reflection

FT-Raman - Fourier transform Raman spectroscopy

FIR – Far infrared region

FWHM - Full width at half maximum

HAp – Hydroxyapatite

Hyd – Hydrazine-treated

INS – Inelastic neutron scattering

IR – Infrared

Laser – Light amplification by stimulated emission of radiation

LT-FT-Raman - Low Temperature Fourier Transform Raman Spectroscopy

Nd:YAG – neodymium-doped yttrium aluminium garnet crystal

Phe – Phenylalanine

Pro - Proline

QFM – Unidade de I&D Química-Física Molecular

XRD - X-Ray Diffraction




Indexes

Table of Contents

Acknowledgements / Agradecimientos	I
Abstract	III
Resumo	V
1. Introduction	1
1.1.From Archaeology to Forensics	4
1.2.Bone Composition	5
1.3.Diagenesis	6
1.4.Methodologies	8
1.4.1. Vibrational Spectroscopy	9
1.4.1.1.Fourier Transform Infrared Spectroscopy	9
1.4.1.2.Raman Spectroscopy	11
1.4.1.3.Inelastic Neutron Scattering Spectroscopy	14
1.4.2. Diffraction Methods	17
1.4.2.1.X-Ray Powder Diffraction	17
1.4.2.2.Neutron Diffraction	18
1.5. Removal of Organic Constituents	19
1.6. Aims of the Study	20
2. Experimental	23
2.1. Materials and Equipment	25
2.2. Sample Preparation	26
2.2.1. Defatting and Deproteination Protocols	28
2.2.1.1.Petroleum Ether and Hydrazine Treatment	28
2.2.1.2.Enzymatic Treatment	28
2.3. Analytical Methodologies	29
2.3.1. Vibrational Spectroscopy	29
2.3.2. Diffraction Methods	31
2.4. Quantitative Analysis of Bone Heat-induced Alterations	33
3. Results and Discussion	37
3.1. Defatting and Deproteinisation	39
3.2. Heat-induced Macroscopic Alterations	47
3.3. Heat-induced Submicroscopic Alterations	50
3.3.1. Fourier Transform Infrared Spectroscopy	50
3.3.2. Raman Spectroscopy	60
3.3.2.1.Raman Microspectroscopy with a 514 nm Laser Line	60

3.3.2.2. Raman Microspectroscopy with a 785 nm Laser Line	64
3.3.2.3. FT-Raman Spectroscopy, Low Temperature FT-Raman and CARS Spectroscopies	70
3.3.3. Inelastic Neutron Scattering	71
3.3.4. Diffraction Methods	75
3.3.4.1. X-Ray Powder Diffraction	75
3.3.4.2. Neutron Diffraction	79
4. Conclusions	87
5. References	91
Abbreviations	105
Indexes	

Index of Figures

Figure 1.1. Representation of chemical substitutions in bioapatite crystal lattice	6
Figure 1.2. Schematic representation of heat induced changes in human bone, for the temperature range 25°C to 1000°C. Upper part: colour alterations. Lower part: microscopic variations. Symbols: loss ↵ ; appearance ↷ ; decrease ▼ ; increase ▲ ; organic matrix  ; crystal thickness and length  ; intercrystallite space 	7
Figure 1.3. Schematic representation of an FTIR-ATR experiment	10
Figure 1.4. Schematic representation of the vibrational transitions corresponding to IR absorption and light scattering – Rayleigh and Raman (Stokes and Anti-Stokes)	12
Figure 1.5. Representation of the vibrational transitions involved in the CARS effect	14
Figure 2.1. Representation of the measurement of maximum diameter and maximum length performed in bone sections prior and after the burning experiment	27
Figure 2.2. Representation of the cuts made humerus (A) and femur (B) diaphysis, from proximal to distal regions	27
Figure 2.3. Schematic representation of the calculation of crystallinity index through XRD.....	32
Figure 3.1. ATR spectra, in the mid-infrared region, for femur samples from skeleton CC_NI_18: intact (red); enzymatically-treated (Enz, black) and hydrazine-treated (Hyd, blue)	40
Figure 3.2. ATR spectra, in the range 420 – 1280 cm ⁻¹ , for femur samples from skeleton CC_NI_18: intact (red); enzymatically-treated (Enz, black) and hydrazine-treated (Hyd, blue)	40
Figure 3.3. Inelastic neutron scattering spectra (obtained on MAPS) for femur samples from the skeleton CC_NI_18: intact (blue); enzymatically-treated (Enz, black), hydrazine-treated (Hyd, pink)	42
Figure 3.4. Inelastic neutron scattering spectra (obtained on MAPS) for femur samples from the skeleton CC_NI_18: intact (blue); enzymatically-treated (Enz, black), hydrazine-treated (Hyd, pink)	43
Figure 3.5. Inelastic neutron scattering spectra (obtained on TOSCA) for femur samples from the skeleton CC_NI_18: intact (blue); enzymatically-treated (Enz, black), hydrazine-treated (Hyd, pink)	44
Figure 3.6. Inelastic neutron scattering spectra (obtained on TOSCA) for femur samples from the skeleton CC_NI_18: intact (blue); enzymatically-treated (Enz, black), hydrazine-treated (Hyd, pink)	44

- Figure 3.7.** X-Ray diffractograms obtained in the range 22 - 43°, using Cu K α radiation for femur samples from the skeleton CC_NI_18: intact bone sample (red); enzymatically-treated sample (Enz, black), hydrazine-treated sample (Hyd, blue)46
- Figure 3.8.** Photographic assembly of the heat induced colour alterations caused by the exposure to 400, 500, 600, 700, 800, 900 and 1000 °C, based on the records of studies from the Laboratory of Forensic Anthropology of the University of Coimbra, verified in the samples of this work47
- Figure 3.9.** Graphic representation of the heat-induced macroscopic alterations (HIMA) in mass (dark blue), maximum length (light blue) and diameter (green), as a function of temperature, for femur slices from skeleton CC_NI_4249
- Figure 3.10.** Graphic representation of the heat-induced macroscopic alterations (HIMA) in mass (dark blue), maximum length (light blue) and diameter (green), as a function of temperature, for humerus slices from skeleton CC_NI_4249
- Figure 3.11.** ATR spectra, in the far and mid-IR regions for: A) femur samples and B) humerus samples of the skeleton CC_NI_42: intact, enzymatically-treated (Enz) and burned from 400 to 1000 °C51
- Figure 3.12.** ATR spectra, in the far-IR region for (A) femur and (B) humerus samples of the skeleton CC_NI_42: burned at 700 (pink), 800 (brown), 900 (dark blue) and 1000 °C (black)52
- Figure 3.13.** ATR spectra, in the 700 – 1850 cm⁻¹ range for: (A) femur samples and (B) humerus samples of the skeleton CC_NI_42: burned from 400 to 1000 °C54
- Figure 3.14.** Graphic representation of the parameters' variation calculated using FTIR-ATR data: C/P (turquoise), OH/P (I, yellow; II, light blue; III, purple); BPI (light green), API (dark red), C/C (dark blue), as a function of temperature, for (A) femur and (B) humerus bone samples from skeleton CC_NI_42; CI for femur (dark pink) and humerus (light pink): (C) as a function of temperature, (D) as a function of C/P, (E) as a function of BPI and (F) as a function of API; (G) femur OH/P-I (yellow), II (light blue) and III (purple) as a function of API; (H) humerus OH/P-I (yellow), II (light blue) and III (purple) as a function of API; (I) OH/P-II as a function of OH/P-I in femur (orange) and humerus (brown)57
- Figure 3.15.** Raman spectrum of the enzymatically-treated femur sample from the skeleton CC_NI_42, collected with a laser line of 514 nm, in the range 600 – 1800 cm⁻¹60

Figure 3.16. Raman spectra, collected with the laser line of 514 nm, of samples from the skeleton CC_NI_42: (A) femur samples burned from 800 to 1000 °C, in the range 0 – 3800 cm⁻¹, (B) femur samples burned from 800 to 1000 °C in the 270 – 1200 cm⁻¹ range, (C) humerus samples burned from 800 to 1000 °C, in the range 0 - 3800 cm⁻¹, (D) humerus samples burned from 800 to 1000 °C in the 270 – 1500 cm⁻¹ range61

Figure 3.17. Graphic representation of the parameters' variation as a function of temperature, based on Raman data (with a 514 nm laser line): C/P-I (yellow), C/P-II (light blue); OH/P (turquoise); Maturity/Crystallinity (dark blue), for femur (A) and humerus (B) bone samples from skeleton CC_NI_42; (C) Maturity/Crystallinity as a function of C/P-II for femur (dark blue) and humerus (light blue); (D) Maturity/Crystallinity as a function of C/P-I for femur (dark blue) and humerus (light blue)64

Figure 3.18. Raman spectrum of an unburned femur sample from skeleton CC_NI_42, collected with a 785 nm laser line, in the range 0 – 3750 cm⁻¹65

Figure 3.19. Raman spectra, in the range 0 – 3750 cm⁻¹ collected with the laser of 785 nm of femur samples from the skeleton CC_NI_42, burned between 800 and 1000 °C66

Figure 3.20. Raman spectra, in the range 0 – 1600 cm⁻¹ collected with the laser of 785 nm of bone samples from the skeleton CC_NI_42: A) femur and B) humerus, burned between 800 and 1000°C67

Figure 3.21. Graphical representation of the temperature dependence of the calculated parameters using Raman data obtained with the 785 nm laser: C/P-I, C/P-II, and Maturity/Crystallinity for femur (A) and humerus (B) bone samples from skeleton CC_NI_42; (C), (E) and (G) Maturity/Crystallinity, C/P-I and C/P-II for femur, from data obtained with the 514 nm (turquoise) and 785 nm (blue) lasers; (D), (F) and (H) Maturity/Crystallinity, C/P-I and C/P-II for humerus, from data obtained with the 514 nm (turquoise) and 785 nm (blue) lasers69

Figure 3.22. (A) FT-Raman spectrum of humerus sample from the skeleton CC_NI_42, burned at 700 °C; (B) Low Temperature FT-Raman spectrum of humerus sample from the skeleton CC_NI_42, burned at 400°C71

Figure 3.23. Inelastic neutron scattering spectra, collected in TOSCA, for femur (A) and humerus (B) samples from the skeleton CC_NI_42 burned between 400 and 1000°C72

Figure 3.24. Inelastic neutron scattering spectra, collected in MAPS, for bone samples from skeleton CC_NI_42, burned at temperatures between 400 and 1000 °C: femur (A) and humerus (B)74

- Figure 3.25.** Graphical representation of the temperature dependence of the $\nu(\text{OH})$ INS band intensity, for humerus and femur samples from skeleton CC_NI_4275
- Figure 3.26.** X-ray diffractograms, in the range $2\theta = 22 - 43^\circ$, using $\text{Cu K}\alpha$ radiation, for bone samples from skeleton CC_NI_42: unburned/untreated and burned at temperatures between 400 and 1000 °C; femur (A) and humerus (B)76
- Figure 3.27.** Graphical representation of the temperature dependence of CI and crystals thickness and length calculated through XRD data, for femur (A) and humerus (B) samples from skeleton CC_NI_42; (C) Crystals length variations as a function of crystals thickness, in femur and humerus78
- Figure 3.28.** Neutron diffractograms, in the $0 - 4 \text{ \AA}$ range, for femur samples from skeleton CC_NI_42, burned at 400 °C (A), 700 °C (B) and 1000 °C (C)80
- Figure 3.29.** Graphical representation of the temperature dependence, observed through neutron diffraction, for: the (002) (light green), (111) and (310) (turquoise) diffracting peaks intensity (A); the (002) (light green), (111) and (310) (turquoise) diffracting peaks FWHM (B)83

Index of Tables

Table 1.1. Main infrared, Raman and INS vibrational wavenumbers for samples of human bone	16
Table 2.1. List of reagents, equipment and software used along this work	25
Table 2.2. Analytical approaches used in the analysis of femur and humerus samples exposed to heat and to the petroleum ether and hydrazine, and lipase and collagenase procedures.....	31
Table 2.3. Quantitative relationships for assessing heat induced alterations in bone, based on FTIR, Raman and XRD data	34
Table 3.1. CI, C/P, API, BPI, (API+BPI)/605 and C/C parameters obtained from the FTIR-ATR data collected for intact, hydrazine and enzymatically-treated samples of femur from skeleton CC_NI_18	41
Table 3.2. CI and crystals' thickness and length (Å), obtained from the X-ray diffraction data for the intact, hydrazine and enzymatically-treated samples of femur from the skeleton CC_NI_18	46
Table 3.3. Pre- and post-burning values of mass (g), maximum length and maximum diameter (mm) of femur and humerus slices burned at different temperatures (°C), for 120 min. The respective percentage of these features after the burning experiment are also presented (heat induced macroscopic alterations, HIMA)	48
Table 3.4. CI, C/P, API, BPI, OH/P and C/C parameters calculated through FTIR-ATR data, for femur and humerus samples from the skeleton CC_NI_42: intact, enzymatically-treated and burned from 400 to 1000 °C for 120 min	55
Table 3.5. Calculation of the maturity/crystallinity, C/P and OH/P parameters for femur and humerus from skeleton CC_NI_42, upon burning at temperatures of 800, 900 and 1000 °C, for 120 min, obtained through Raman spectroscopy with a 514 nm laser line	63
Table 3.6. Calculation of the maturity/crystallinity, C/P and OH/P parameters for an unburned femur sample from skeleton CC_NI_42, through Raman spectroscopy with a 785 nm laser line	66
Table 3.7. Calculation of the maturity/crystallinity and C/P parameters for femur and humerus bone samples from skeleton CC_NI_42, burned at different temperatures (°C), based on Raman data with the 785 nm laser	68
Table 3.8. Calculated CI and crystal thickness and length (Å), through XRD results, for femur and humerus samples from skeleton CC_NI_42: intact and burned at temperatures between 400 and 1000 °C	77

